

NEUTRON STAR POPULATIONS

by

Christopher Lee Fryer

A Dissertation Submitted to the Faculty of the

DEPARTMENT OF ASTRONOMY

In Partial Fulfillment of the Requirements
For the Degree of

DOCTOR OF PHILOSOPHY

In the Graduate College

THE UNIVERSITY OF ARIZONA

1 9 9 6

INFORMATION TO USERS

This manuscript has been reproduced from the microfilm master. UMI films the text directly from the original or copy submitted. Thus, some thesis and dissertation copies are in typewriter face, while others may be from any type of computer printer.

The quality of this reproduction is dependent upon the quality of the copy submitted. Broken or indistinct print, colored or poor quality illustrations and photographs, print bleedthrough, substandard margins, and improper alignment can adversely affect reproduction.

In the unlikely event that the author did not send UMI a complete manuscript and there are missing pages, these will be noted. Also, if unauthorized copyright material had to be removed, a note will indicate the deletion.

Oversize materials (e.g., maps, drawings, charts) are reproduced by sectioning the original, beginning at the upper left-hand corner and continuing from left to right in equal sections with small overlaps. Each original is also photographed in one exposure and is included in reduced form at the back of the book.

Photographs included in the original manuscript have been reproduced xerographically in this copy. Higher quality 6" x 9" black and white photographic prints are available for any photographs or illustrations appearing in this copy for an additional charge. Contact UMI directly to order.

UMI

**A Bell & Howell Information Company
300 North Zeeb Road, Ann Arbor MI 48106-1346 USA
313/761-4700 800/521-0600**

NEUTRON STAR POPULATIONS

by

Christopher Lee Fryer

A Dissertation Submitted to the Faculty of the

DEPARTMENT OF ASTRONOMY

In Partial Fulfillment of the Requirements
For the Degree of

DOCTOR OF PHILOSOPHY

In the Graduate College

THE UNIVERSITY OF ARIZONA

1 9 9 6

UMI Number: 9720706

UMI Microform 9720706
Copyright 1997, by UMI Company. All rights reserved.

**This microform edition is protected against unauthorized
copying under Title 17, United States Code.**

UMI
300 North Zeeb Road
Ann Arbor, MI 48103

THE UNIVERSITY OF ARIZONA ©
GRADUATE COLLEGE

As members of the Final Examination Committee, we certify that we have
read the dissertation prepared by Christopher Lee Fryer
entitled Aspects of Neutron Star Populations

and recommend that it be accepted as fulfilling the dissertation
requirement for the Degree of Ph.D. in Astronomy

Dr. Willy Benz

W. Benz

12/12/96

Date

Dr. Adam Burrows

Adam Burrows

12/12/96

Date

Dr. David Arnett

David Arnett

12/12/96

Date

Date

Date

Final approval and acceptance of this dissertation is contingent upon
the candidate's submission of the final copy of the dissertation to the
Graduate College.

I hereby certify that I have read this dissertation prepared under my
direction and recommend that it be accepted as fulfilling the dissertation
requirement.


W. Benz
Dissertation Director

12/12/96
Date

STATEMENT BY AUTHOR

This dissertation has been submitted in partial fulfillment of requirements for an advanced degree at The University of Arizona and is deposited in the University Library to be made available to borrowers under rules of the Library.

Brief quotations from this dissertation are allowable without special permission, provided that accurate acknowledgment of source is made. Requests for permission for extended quotation from or reproduction of this manuscript in whole or in part may be granted by the head of the major department or the Dean of the Graduate College when in his or her judgment the proposed use of the material is in the interests of scholarship. In all other instances, however, permission must be obtained from the author.

SIGNED: 

ACKNOWLEDGMENTS

With great surprise, and a little sadness, I find myself recollecting all my friends and companions whose paths have crossed mine over the past five years. I say “surprise”, not because the trail was particularly unbearable, but because I never expected to stay in Astronomy this long. Unlike many of my fellow graduate students and professors, I did not develop a strong desire to understand the cosmos during my childhood. Instead, it was during my stay at Steward that I learned their love and passion for this field.

I can’t praise enough the family of graduate students, post-docs, and professors at Steward. My office-mates, my juggle partners, my biking buddies, my comrades-in-arms at Los Alamos, and the soccer crew all gave me essential moral support. The professors, particularly Adam, put up with my insubordination and temper, and managed to teach me, along the way, invaluable aspects of science and of life. But three advisors stand out as pivotal cultivators of my love for science and Astronomy.

Marc, whose philosophy most closely resembled my own, taught me more about Astronomy than he thinks and more about life than he could possibly imagine. I owe him for many things and will forever be in his debt.

Stirling taught me the great joys held within science and learning. One afternoon, we found ourselves in a thunderstorm as we were hiking near Los Alamos. As lightning flashed all around us, Stirling began to instruct me on the nature of lightning. I soon became so engrossed with his teaching that I forgot the cold and the rain. For that brief moment, he showed me how pleasures of the mind could overcome one’s physical environment. In the same way, he has shown me the importance of all aspects of life.

It is impossible for me to express my admiration for Willy. There is not a person living that I respect more. I will not forget the time that I’ve spent with him and his family.

These three people went beyond collaborators and advisors to become good friends. Friends and family have been the driving force supporting me over the past few years. My korean friends, especially Ga-Ju, became an important part of my supporting family in Tucson. To my wonderful Greeks, Vicky and Demetris, Thanks! But above all, there is one friend with whom I’ve lost touch, but who gave me more support and inspiration than all the others put together. I will never forget you Eun Jung.

TABLE OF CONTENTS

LIST OF FIGURES	8
LIST OF TABLES	13
ABSTRACT	14
 1 Introduction	 15
1.1 Neutron Star Systems and Observations	16
1.2 Astrophysical Applications	18
1.3 Applications to physics	19
1.4 Outline of Dissertation	20
 2 The Dynamics and Outcomes of Rapid Infall onto Neutron Stars	 23
2.1 INTRODUCTION	24
2.2 NUMERICAL METHODS	29
2.2.1 One-dimensional Lagrangian Code	29
2.2.2 Two-dimensional SPH Code	30
2.3 INITIAL CONDITIONS AND PHYSICAL PROCESSES	31
2.3.1 Initial Conditions	31
2.3.2 Equation of State and Neutrinos Processes	32
2.3.3 Infall rates and Assumptions	33
2.4 RESULTS	40
2.4.1 Infall Atmospheres	40
2.4.2 Equilibrium Atmospheres	50
2.4.3 Summary of Results	59
2.4.4 Initial Transient Revisited	60
2.5 IMPLICATIONS	62
2.5.1 TŻ Objects	62

2.5.2	Common Envelope Systems	65
2.5.3	Supernovae	67
2.5.4	Explosions	68
2.5.5	Future Work	69
2.5.6	A Necessary Criterion for the Validity of the Mixing Length Approximation for Convection	70
3	Double Neutron Star Systems: Evidence for Kick Velocities	95
3.1	Introduction	96
3.2	The Nature of the Pulsar Companion	99
3.2.1	Roche Lobe Overflow	100
3.2.2	Rate of Periastron Advance	101
3.2.3	Optical Identification of the Companion	102
3.2.4	Summary	103
3.3	Formation Mechanisms	104
3.4	Symmetric Explosions	106
3.4.1	Orbital Dynamics	107
3.4.2	Neutron Stars in Common-Envelope Phases	110
3.5	Asymmetric Explosions	115
3.5.1	Circular Pre-SN Orbits	116
3.5.2	Eccentric Orbits	120
3.6	Discussion	120
4	Population Syntheses for Neutron Star Systems with Intrinsic Kicks	132
4.1	Introduction	133
4.2	Neutron Star Populations	135
4.2.1	Low-Mass X-ray Binaries	136
4.2.2	High-Mass X-ray Binaries	138
4.2.3	Double Neutron Star Systems	139

4.2.4	Radio Pulsars	139
4.2.5	O/B runaway stars	141
4.3	Galactic and Globular Cluster Potentials	142
4.3.1	Galactic Models	142
4.3.2	Globular Clusters	143
4.4	Simulations	144
4.4.1	Initial Conditions	144
4.4.2	Stellar Models and Binary Evolution	147
4.5	Natal Kick Distributions	150
4.5.1	Maxwellian and Flat Distributions	151
4.5.2	Delta Function and Bimodal Distributions	152
4.6	Conclusions	154
5	Ejecta from Accretion Induced Collapse: A Cosmic Pollutant	181
5.1	Introduction	182
5.2	Models and Results	185
5.2.1	Numerical Methods	186
5.2.2	Neutrino Physics	186
5.2.3	Equation of State	188
5.2.4	Convection and Rotation	190
5.2.5	Neutrino Wind	192
5.3	Discussion and Conclusions	192
	REFERENCES	203

LIST OF FIGURES

2.1	characteristic timescales; photon diffusion τ_γ , neutrino cooling τ_ν , and sound travel time τ_s versus entropy. Note that at an entropy lower than that defined by the intersection between the sound travel and neutrino cooling timescale, no stable atmosphere can form. Note also that the intersection between photon diffusion and neutrino cooling defines the entropy at which photon trapping is complete.	78
2.2	structure of an infall atmosphere. Note that the region within the accretion shock is convectively unstable.	79
2.3	Density vs. radius for a $10^3 M_\odot \text{ y}^{-1}$ infall model. The points are from numerical simulations. The lines are analytical results for different adiabatic indices.	80
2.4	steady state shock radius versus accretion rate for a range of adiabatic indices in a one-dimensional infall model.	81
2.5	Entropy versus radius after 50 ms for a range of infall atmospheres. .	82
2.6	entropy-driven convective plume for $10^3 M_\odot \text{ y}^{-1}$ infall atmosphere 10 s after creation of the accretion shock. The negative entropy gradient is induced by the initial outward motion of the shock. Average plume velocity is 3000 km/s and mean inflow velocity is 1000 km/s.	83
2.7	atmosphere mass versus entropy for two sizes of atmosphere: $R = 10^9$ cm and 10^{13} cm. The dashed lines denote atmospheres with no external pressure, whereas the solid lines include a pressure term derived from typical values for Bondi-Hoyle accretion.	84
2.8	entropy profiles at 70 ms intervals for an $S_{\text{tot}} = 50$ equilibrium atmosphere. Note that with increasing time, the innermost material cools (lowering its entropy) while an increasing amount of material is heated (raising its entropy).	85
2.9	entropy-driven convection for an $S_{\text{tot}} = 50$ equilibrium atmosphere 200 ms after turning on neutrino processes. The negative entropy gradient is induced by neutrino heating and drives convection. The mean outflow velocity is 4000 km/s and the mean inflow is 9000 km/s. .	86
2.10	the same simulation from Figure 4 after 500 ms. The atmosphere is now exploding with a kinetic energy of 2×10^{-6} foe. The mean outflow velocity is 5000 km/s and the mean inflow is 3000 km/s. . . .	87

2.11	entropy vs. mass at 80 ms intervals for an $S_{\text{tot}} = 80$ equilibrium atmosphere. Note that the inner material radiates its energy through neutrino losses, lowering its entropy.	88
2.12	Neutrino luminosity and mean neutrino energy as a function of time for an $S_{\text{tot}} = 80$ equilibrium atmosphere.	89
2.13	total mass accreted versus time with the best constant accretion fit for an $S_{\text{tot}} = 80$ equilibrium atmosphere.	90
2.14	a comparison between numerical accretion rates and the analytical results of Colgate et al. (1993). The filled circles compare analytical results using only the radiation entropy from the numerical calculations, whereas the open symbols use the total entropy.	91
2.15	accretion rate versus entropy. The two lines denote analytical results using outer pressures of 0% and 0.25% that of the pressure at the surface of the neutron star. The points are results from the simulations.	92
2.16	entropy profiles versus radius for the nucleosynthesis models of Cannon (top line) and Biehle (bottom line).	93
2.17	Biehle's structure model after 0.5 s. The high entropy material is driving the atmosphere outward. Outward velocities approach 6000 km/s.	94
3.1	Post-supernova orbital separation, A , and eccentricity, e , as a function of the time, T_{SN} , elapsed from the supernova explosion, for PSR 1913+16 and PSR 1534+12.	126
3.2	Pre-supernova orbital separation, A_o , mass of the exploding (helium) star, M_o , and ratio, R_L/R_{He} , of the Roche lobe radius to the maximum radius acquired by a helium star prior to the supernova, as a function of the time, T_{SN} , elapsed from the explosion. Quantities are plotted for PSR 1913+16 and PSR 1534+12 and under the assumptions of circular pre-supernova orbits and symmetric supernovae.	127
3.3	Ratio, R_L/R_{He} , of the Roche lobe radius to the maximum radius acquired by a helium star prior to the supernova, as a function of the mass, M_o , of the helium star, for a complete range of pre-supernova eccentricities. Plots are shown for PSR 1913+16 and PSR 1534+12 and for symmetric supernovae. A minimum helium star mass for neutron star formation of $2 M_{\odot}$ has been assumed.	128

- 3.4 Limits on the pre-supernova orbital separation, A_o , and mass of the helium star, M_o for (a) PSR 1913+16 and (b) PSR 1534+12, and for three different magnitudes of the kick velocity, V_k . The thick dashed vertical line corresponds to the maximum separation set by the geometrical constraint; the thick dotted line corresponds to the minimum helium-star mass that can be accommodated in the orbit; the thin lines correspond to the maximum possible pre-supernova orbital angular momentum and their position depends on the kick magnitude. Limits are calculated for circular pre-supernova orbits and neglecting any post-supernova orbital evolution. 129
- 3.5 Limits on the pre-supernova orbital separation, A_o , and mass of the helium star, M_o for (a) PSR 1913+16 and (b) PSR 1534+12, and for three different values of the time, T_{SN} elapsed from the supernova in units of the pulsar characteristic ages, τ_c . The thick solid line corresponds to the minimum helium-star mass that can be accommodated in the orbit; the thin lines correspond to the geometrical (vertical) and the angular momentum constraints, and depend on the value of T_{SN} . Limits are calculated for circular pre-supernova orbits and for kick velocity magnitudes (a) $V_k = 400$ km/s and (b) $V_k = 300$ km/s. 130
- 3.6 Limits on the pre-supernova orbital separation, A_o , and mass of the helium star, M_o for (a) PSR 1913+16 and (b) PSR 1534+12, for eccentric pre-supernova orbits and for different values of the magnitude of the kick velocity, V_k . Post supernova orbital evolution has been neglected. 131
- 4.1 The observed transverse velocities of radio pulsars versus their distances D from the Sun (Harrison et al. 1993). The open triangles denote the 44 pulsars with proper motions determined by Harrison et al. and the filled hexagons are the 43 additional pulsars with proper motions calculated by other techniques. 164
- 4.2 Luminosity versus velocity for a simulated sample (no biases) without distance errors on the left and with distance errors on the right. The pulsars in the simulated sample are evenly chosen in velocity/luminosity space with no intrinsic biases. We assume the distance errors are Gaussian with a magnitude of 20% distance. The faster pulsars *appear* to be more luminous. 165

- 4.3 The same as Figure 2, except velocity is plotted versus distance. Note that with distance errors, another fictitious bias appears with the nearby pulsars tending to have slower velocities. 166
- 4.4 The dependence of the various neutron-star binaries with respect to the various initial binary and evolutionary parameters and velocity. The filled circles correspond to the two standard parameter set that we use with $q_0 = 0.35, 0.15$. The open symbols correspond to the initial binary parameters (§4.4.1) and the skeletal symbols correspond to the binary evolution parameters (§4.4.2). 167
- 4.5 The velocity distribution of pulsars for a range of initial and binary-evolution parameters with a δ -function kick of 200 km/s. The binary parameters affect only a small number of the pulsars. The typical pulsar velocity is unchanged by even extreme changes in the binary parameters. The largest differences come from assuming that there is no mass lost from winds. 168
- 4.6 The simulated populations normalized by the observations versus the root-mean-square velocity for a Maxwellian Distribution. For the pulsars, we plot $(99.99 - P)$ where P is the percentage probability that the simulated velocity distribution and the observed velocity distribution are not from the same parent population. We use our standard set of binary parameters. A “successful” solution is one for which all the normalized numbers are greater than unity simultaneously. 169
- 4.7 Fraction of Neutron Stars with a velocity greater than a given velocity versus that velocity for the series of Maxwellian kick distributions. A zero kick simulation with no mass loss from winds is included to give the maximum effects from the binary parameters. 170
- 4.8 The same as Fig. 6, but with $q_0 = 0.15$ and $M_{t,u} = 10, 100 M_\odot$ 171
- 4.9 The same as Fig. 6, but for flat distributions with $q_0 = 0.15$ 172
- 4.10 The same as Fig. 6, but for δ -function kicks. 173
- 4.11 Kick distributions with fraction of neutron stars versus velocity bin. The solid line denotes the best-fitting overall kick profile. The remaining curves are constrained by requiring that the middle range of velocities be non-zero to varying degrees. 174
- 4.12 Same as Figure 11, but with the best-fitting overall profiles for a range of distance scale factors. 175

- 4.13 χ^2 residuals versus the degree to which the middle velocities are filled, normalized by the residuals from the best-fitting overall distribution. The curves represent a range of scale factors for the distance. 176
- 4.14 Same as Fig 6. with a double-peaked δ -function distribution: 30% at 0 km s⁻¹ and 70% at the value on the plot. Again, we use $q_0 = 0.15$. . 177
- 4.15 Same as Fig 6. with a double-peaked distribution: 30% at 0 km s⁻¹ and 70% with a flat distribution with a mean at 625 km s⁻¹ with a mean: σ . Again, we use $q_0 = 0.15$ 178
- 4.16 The neutron star velocity distribution for our best fitting double peaked distribution. 179
- 4.17 The velocity distribution of O/B stars for simulations with no kick (solid line - bound systems, dotted line - unbound O/B stars) and for our best fitting double peaked distribution (long-dashed line - bound systems, short-dashed line - unbound systems.) 180
- 5.1 shows density profiles for the initial model (solid line), the BCK EOS after 40 ms (short-dashed line), the SL EOS after 40 ms (dotted line), and a simulation using 80 % of the pressure from the BCK EOS after 40 ms (long-dashed line). Changing the pressure by 20 % drastically alters the evolution of the collapse. 198
- 5.2 displays mass-point trajectories for a simulation using the SL EOS. The resolution is increased near the transition between ejected material and proto-neutron star material. The inner 9 lines represent the $1M_\odot$ core. 199
- 5.3 is identical to Figure 2 using the BCK equation of state. 200
- 5.4 is identical to Figure 2 with the same SL EOS but without neutrino transport. Comparison with Figure 2 differentiates a prompt explosion from a delayed neutrino explosion. 201
- 5.5 plots the ratio of pressure from the SL EOS and the BCK EOS. For densities less than 10^{14} g cm⁻³, the BCK pressure is consistently higher by 10-20 %. 202

LIST OF TABLES

2.1	Accretion Parameters	74
2.1	Accretion Parameters	75
2.2	Infall Atmospheres	76
2.3	Infall Atmospheres	76
2.4	Constant Entropy Atmospheres	77
2.5	Infall Results	77
2.6	Convection	77
3.1	Double Neutron Star Systems	124
3.2	Double Neutron Star Systems	125
4.1	Parameters: Initial Conditions ^a	158
4.2	Parameters: Orbital ^a	159
4.3	NS Retention: Maxwellian Kick Distribution ^a	160
4.4	NS Retention: Maxwellian Kick Distribution ^a	161
4.5	NS Retention: Flat Kick Distribution ^a	162
4.6	NS Retention: δ -Function Kick Distribution ^a	163
5.1	AIC Simulations	196
5.2	BCK EOS models ^a	197

ABSTRACT

This dissertation clarifies two aspects of neutron-star formation and evolution: the formation of neutron stars through the accretion-induced collapse of white dwarfs and the common envelope evolution of neutron stars. In both cases, we utilize a 1-D lagrangean and 2-D SPH hydrodynamics codes equipped with a broad range of physics including neutrino emission, absorption, and transport, general relativity and dense equations of state. These results are then applied to a Monte-Carlo population synthesis code to study the effects of kicks placed upon neutron stars near the time of their formation. By comparing these results with the current observational data, we find that a bimodal kick distribution of neutron-star kicks is required.

CHAPTER 1

INTRODUCTION

This thesis is devoted to several aspects of neutron star formation and evolution, a field which covers a broad range of astronomical objects from supernovae and gamma-ray bursts to X-ray binaries and O/B runaway stars. Before we become mired in the details, let us begin with a brief overview of what makes neutron stars such fascinating objects. Neutron stars, along with black holes, are the primary sources of the high-energy emission in the universe. High-energy astrophysics is one of the youngest and fastest-growing fields in astronomy. Because of its relative youth (in comparison to optical and radio astronomy), every new instrument brings with it new insights, surprises, and problems (Bradt, Ohashi, & Pounds 1992).

Neutron stars allow the adventurous theorist to utilize a wide range of physics. The potential energy liberated from 1 gram of matter falling onto a neutron star is $\sim 2 \times 10^{20}$ ergs, an energy roughly equivalent to a 50 kiloton bomb! The free-fall velocity of this matter is $\sim 60\%$ the speed of light. Neutron stars have densities $\sim 5 \times 10^{14}$ g cm $^{-3}$, over 13 orders of magnitude greater than anything found on the Earth. In addition, neutron stars exhibit some of the strongest magnetic fields in

the universe (Chanmugam 1992).

This chapter provides an introduction to neutron stars and the many systems in which they are found. In §1.1, we list and describe the basic systems along with the current and upcoming instruments used to detect these systems. Of course, the first step in studying these systems is to understand the systems themselves, but, as we shall discuss in §1.2, they can also be used as probes of the environments through which neutron stars pass. In addition, neutron star systems, with their extreme energetics and densities, provide ideal laboratories to test fundamental laws in physics. Let us now look into the details of these studies.

1.1. Neutron Star Systems and Observations

Although the emission from neutron stars is not limited to high-energy radiation, X-ray and gamma-ray satellites such as Einstein, ROSAT, COS-B, HEAO-1, HEAO-3, GRO, Ginga, ASCA, etc. have secured the prominent role neutron stars and the accretion onto neutron stars play in astronomy. A majority of the brightest high-energy sources in the sky involve accretion onto compact objects (e.g. neutron stars or black holes). The era of high-energy astronomy has just begun and the future holds many new high-energy observatories: AXAF, Integral, XMM, Spectrum-X/ γ , etc.

Probably the most famous example of an X-ray emitting object involving a neutron star is PSR0531+21 (the Crab pulsar), but pulsars near supernova remnants are not the only high-energy emitting neutron stars observed. For example, using Einstein satellite data, Trinchieri and Fabbiano (1991) analyzed the X-ray sources near M31 and found that not only could the entire X-ray flux be explained by discrete sources (many of which are accreting neutron stars), but

that a majority of the sources appeared to be associated with the globular clusters around M31. AXAF will provide sufficiently accurate spectral information for these objects to achieve reliable identifications, placing constraints upon their formation rates and/or lifetimes if combined with a detailed theoretical model.

Accreting neutron stars can also explain such peculiarities as Be/X-ray systems. These objects have optical components compatible with Be spectra, but X-ray fluxes much too high for B stars or even accretion onto white dwarfs (see the ROSAT data analysis by Motch *et al.* 1991). It is probable that these objects are neutron stars accreting in common envelopes, but this speculation can only be verified with detailed accretion models.

These are just a few examples of a long list of high-energy emitting neutron-star sources which includes low-mass X-ray binaries, high-mass X-ray binaries, gamma-ray bursters, X-ray bursters, millisecond pulsars, objects exhibiting quasi-periodic oscillations, and so on. Although neutron stars have gained prominence as sources of high-energy emission, they are not limited to low-wavelength radiation. Of course, as with any well-studied object, PSR 0531+21 (the Crab Pulsar) has been observed in virtually all wavelengths. Many neutron stars have large fluxes in lower-energy wavelengths. A large database of strong radio-emitting pulsars exists with well over 100 of these sources in the galaxy (Taylor, Manchester, & Lyne 1993). In addition, merging neutron stars and supernova are likely sources of gravitational wave emission that may be detected by LIGO (Abromovici *et al.* 1992, Ruffert, Janka, & Schafer 1996, Burrows & Hayes, 1996).

1.2. Astrophysical Applications

As part of the incessant curiosity of astronomers, just understanding the observed neutron star systems themselves makes research on neutron stars a worthwhile endeavor. However, neutron star systems can also be used as probes to study many other aspects of astronomy. In this section, we list some of the applications of neutron stars and neutron star systems to other aspects of astronomy.

As the products of supernovae, neutron stars can be used to understand the supernova mechanism itself. The remnant neutron star mass may provide insight into the supernova progenitor as well as the explosion itself (Timmes, Woosley, & Weaver 1996). In addition, the magnetic fields, spin-rates, and, as we shall show in this dissertation, the velocities, all can give information about the supernova explosion.

Observations of neutron star populations can be used in combination with population synthesis models of these systems to gain insight into the formation and evolution of massive star binaries. For instance, we shall show that the number of low-mass X-ray binaries found in the galaxy imply that the companion/primary mass ratio for massive stars is peaks at extreme values (~ 0.1). A more direct example of neutron-star probes in massive binaries is PSR J0045-7319. (Kaspi *et al.*) This binary system contains a neutron star and a B-star companion. The orbit of this system is highly eccentric with its closest separation a mere $3.7 \pm 0.5 R_{\odot}$. The neutron star strongly disturbs the B-star during periastron and measurements of the B-star's oscillations will allow an alternate way to probe and understand massive star evolution (van Kerkwijk 1996).

High-velocity pulsars can also be used as probes of the galactic halo. The work in this dissertation prepares us for these studies, but there are many selection effects

which must be overcome before any concrete conclusions can be drawn (Narayan & Ostriker 1990). If gamma-ray bursts are galactic in nature, the distribution of these bursts combined with some knowledge of neutron-star velocities can be used as a probe of the galactic halo (Podsiadlowski, Rees, & Ruderman 1995). If gamma-ray bursts are cosmological (e.g. merging neutron stars), we can set limits on early star formation. As we learn more about neutron stars, this list will increase.

1.3. Applications to physics

Even more interesting are the many applications neutron-star systems provide for testing basic physics. The nature of neutron stars, with their high densities and high magnetic fields along with the high energies of the matter accreting onto neutron stars make neutron stars ideal laboratories to study general relativity, the properties of degenerate matter, particle physics, magnetic fields, etc.

For instance, as we shall show in this dissertation, models of collapsing white dwarfs depend strongly upon the dense equation of state used. There remain many uncertainties on the behavior of dense matter and it is costly, if not impossible, to devise experiments to sort out these uncertainties in Earth-based labs. However, such conditions already exist in collapsing white dwarfs and by modeling them and comparing these models to observations, we can constrain the uncertainties in the physics. Another example using neutron star systems to gain some knowledge about the properties of dense material comes from measuring the masses of neutron stars. Different equations of state predict different maximum stable masses for neutron degenerate material. By measuring the masses, we may be able to rule out some dense equations of state (van Kerkwijk, van Paradijs, & Zuiderwijk 1995).

Neutron star formation involves the emission of a large number of neutrinos.

By observing these neutrinos and coupling these observations to models of the collapse of white dwarfs or supernovae, we gain insight into the nature of neutrino emission, neutrino mixing, and similar aspects of particle physics. For instance, the neutrinos emitted from neutron star mergers, supernovae, and the collapse of white dwarfs give information about the maximum mass of neutrinos (e.g. Bahcall & Glashow 1987).

Pulsar 1913+16 has already provided an alternate test for general relativity (Hulse & Taylor 1975). But, as we have already mentioned in §1.1, the merging of binary pulsars and asymmetric explosions of supernovae should be observable by LIGO and, hence, provide another verification of general relativity. (Abromovici *et al.* 1992, Ruffert, Janka, & Schafer 1996, Burrows & Hayes, 1996).

1.4. Outline of Dissertation

We begin the work of this dissertation (Chapter 2) with the hydrodynamical study of rapid infall onto neutron stars ($\dot{M} \gtrsim 10^{-4} M_{\odot} y^{-1}$). These rates apply to physical conditions for neutron stars in common envelope systems with their companions, Thorne-Żytkow objects, and supernova fallback. During the evolution of many types of neutron star binaries, the neutron star passes through a phase where it is in the envelope of its companion. These simulations are critical to understanding this common envelope phase. Thorne-Żytkow objects are also a common phase for alternate formation mechanisms of many neutron star populations. Our results show that if the neutron star does develop into a Thorne-Żytkow object, it will quickly collapse into a black hole. We can not rely upon Thorne-Żytkow objects to be an alternate route in the formation for neutron star systems. The accretion of supernova fallback also has consequences upon neutron star and black hole

formation. All of these implications will be discussed in Chapter 2.

We can apply our results to the study of specific neutron star systems. Chapter 3 discusses the formation of double neutron star systems such as PSR 1913+16 using the additional constraint provided by our rapid infall models. Our rapid infall models place limits on the conditions required for a neutron star to survive a common envelope phase. In Chapter 4, we describe a binary population model designed to study the formation of massive binaries. We use our results of neutron-star accretion with this population synthesis code to gain some information of velocity imparted on the neutron star due to some asymmetry in the supernova explosion which created the neutron star. This chapter gives the first results of this powerful code which we will later use to address many astrophysical puzzles. For instance, we include in this code the motion of our neutron star systems through a galactic potential. With a better understanding of the neutron star populations, our simulations can be used to probe the galactic halo.

A weak point in our population synthesis simulations is that these models do not include a potentially important alternate neutron-star formation mechanism: the collapse of accreting white dwarfs. Population synthesis calculations place only rough constraints upon the rate of collapsing white dwarfs. However, by modeling the collapse of these white dwarfs, we can use the nucleosynthetic yield of these objects to constrain their rate. These models are discussed in Chapter 5.

We end this chapter with a brief summary of this thesis. We have outlined the chapters based upon our hydrodynamical models of accretion. We then apply these results based on basic physics to a variety of neutron star populations. Alternatively, from the observational perspective, we can begin by studying a range of neutron star populations. Population synthesis models are plagued by

a number of uncertainties, chief among them being common envelope evolution and the role of accretion-induced collapse of white dwarfs play in the formation of neutron stars. We attack two problems, rapid infall onto neutron stars, a part of common-envelope evolution, and the collapse of accreting white dwarfs. As with most scientific endeavors, we find that we have uncovered more new questions than we have answered, but a wealth of information in physics and astronomy lies before us.

CHAPTER 2

THE DYNAMICS AND OUTCOMES OF RAPID INFALL ONTO NEUTRON STARS

Brief Summary

We present an extensive study of accretion onto neutron stars in which the velocity of the neutron star and structure of the surrounding medium is such that the Bondi-Hoyle accretion exceeds $10^{-3}M_{\odot} \text{ y}^{-1}$. Two types of initial conditions are considered for a range of entropies and chemical compositions: an atmosphere in pressure equilibrium above the neutron star, and a freely falling inflow of matter from infinity (also parametrized by the infall rate). We then evolve the system with one- and two-dimensional hydrodynamic codes to determine the outcome. For most cases, hypercritical (also termed “super-Eddington”) accretion due to rapid neutrino cooling allows the neutron star to accrete above the Bondi-Hoyle rate as previously pointed out by Chevalier. However, for a subset of simulations which corresponds to evolutionarily common events, convection driven by neutrino heating can lead to explosions by a mechanism similar to that found in core-collapse

supernovae.

Armed with the results from our calculations, we are in a position to predict the fate of a range of rapid-infall neutron star accretors present in certain low-mass X-ray binaries, common envelope systems, supernova fallbacks and Thorne-Żytkow objects (TŻOs). A majority of the common envelope systems that we considered led to explosions expelling the envelope, halting the neutron star's inward spiral, and allowing the formation of close binary systems. As a result, the smothered neutron stars produced in the collisions studied by Davies & Benz may also explode, probably preventing them from forming millisecond pulsars. For the most massive supernovae, in which the fallback of material towards the neutron star after a successful explosion is large, we find that a black hole is formed in a few seconds. Finally, we argue that the current set of TŻO formation scenarios is inadequate and leads instead to hypercritical accretion and black hole formation. Moreover, it appears that many of the current TŻ models have structures ill-suited to modeling by mixing-length convection. This has prompted us to develop a simple test to determine the viability of this approximation for a variety of convective systems.

2.1. INTRODUCTION

It is only in the last few decades, with the arrival of high-energy observatories, that the problem of accretion onto neutron stars has moved from the speculations of theorists to the constraints of observations. Satellites such as *Einstein*, *ROSAT*, *GRO*, *Ginga*, and others, have contributed to a growing list of accreting neutron star sources such as gamma-ray bursters, X-ray bursters, millisecond pulsars, high mass X-ray binaries (HMXB), low mass X-ray binaries (LMXB), and a number of objects entangled within the current evolutionary scenarios for binary pulsars.

Future observations (*AXAF*, *Integral XMM*, *Spectrum-X/γ*, etc.) promise to add more. Unfortunately, the current state of theoretical models falls short of the present and upcoming data. At the root of the theoretical difficulties is the range of extreme physical conditions encountered in many of the observed systems: high magnetic fields, angular momentum, degenerate matter, neutrino effects, etc. In addition, as we shall demonstrate in this paper, it is likely that multidimensional effects are important. As a result, progress in understanding neutron star accretion has been slow. In this paper, the first of a series, we will consider the effects of rapid mass infall onto neutron stars ($\dot{M}_{\text{Bondi-Hoyle}} > 10^{-3} M_{\odot} \text{ y}^{-1}$). By *infall* rate, we mean the rate at which material is added to the atmosphere surrounding the neutron star. This is to be distinguished from the term *accretion* which we reserve for the mass incorporated into the neutron star. High infall rates occur in common envelope systems such as Be/X-ray objects, more deeply buried systems such as Thorne-Żytkow objects (TZO), and supernova fallback.

Early work studying rapid mass infall onto neutron stars logically began with estimates of the fallback of matter onto newborn neutron stars in supernovae (Colgate 1971; Zel'dovich, Ivanova, & Nadezhin 1972). Both groups found that the canonical photon Eddington accretion rate vastly underestimates accretion onto the neutron star as neutrino, rather than photon, emission becomes the dominant cooling source. Chevalier (1989), and Houck & Chevalier (1991) have studied in greater analytic detail the fallback of matter onto the adolescent neutron star, confirming this “hypercritical” accretion rate. Even though the amount of fallback matter is generally a small fraction of the material expelled by the supernova, it is a large portion of the material undergoing heavy element nucleosynthesis. Thus, understanding supernova fallback is crucial, not only to decide whether or not a neutron star or black hole is left after the explosion, but also to understand

the nucleosynthetic yields of supernova explosions which, in turn, have profound repercussions for galactic chemical evolution.

However, most of the interest in atmospheres around neutron stars has been directed toward understanding Thorne-Żytkow objects, an hypothetical red giant in which the normally white dwarf-like core is a neutron star. These objects are supported, in addition to the “normal” contribution from thermonuclear burning, by the release of gravitational energy from accretion onto the neutron star, and therefore have longer lifetimes than standard red giants. The concept of powering a star from mass accretion onto a degenerate object was revived from its pre-fusion days (Landau 1937; Gamow 1937) by Thorne & Żytkow (1975). In their study of a range of models for stellar envelopes greater than $1 M_{\odot}$, Thorne & Żytkow (1977) separated their models into two classes depending upon atmosphere mass. For the more massive envelopes, accretion alone is insufficient to provide pressure support, suggesting nuclear burning arising from the extreme conditions near the surface of the neutron star as a possible complementary mechanism. Follow-up work by Biehle (1991, 1994), Cannon et al. (1992), and Cannon (1993) focused on this class of objects, using more detailed descriptions of the nuclear burning processes. These simulations established abnormal nuclear burning (such as the rp-process) as an additional source of energy and led to more definitive results on the observable chemical compositions of TŻOs, should they exist. In recent years, the usage of the terms TŻO has grown in the literature to encompass a broader range of neutron-star atmosphere systems. In this paper, we reserve the TŻO designation for those objects originally envisioned by Thorne, Żytkow Cannon and Biehle.

As an ever-branching list of formation scenarios has been dreamed up, the occurrence of rapid infall on neutron stars has evolved from the seed of a theorist’s

imagination to a virtual certainty. Among them one finds: 1) supernova fallback, 2) common envelope evolution (Taam, Bodenheimer, & Ostriker 1978; Terman, Taam, & Hernquist 1994), 3) collisions between main-sequence stars or red giants and neutron stars in globular clusters or galactic nuclei (Benz & Hills 1992; Davies & Benz 1995), 4) an induced collision between a newly formed neutron star and its binary companion as it is kicked by an asymmetric supernova explosion (Leonard, Hills, & Dewey 1994), and 5) a neutron star caught within the torus of an active galactic nucleus or within a dense molecular cloud (D. N. C. Lin - private communication). Supernova fallback excepted, not much attention has been paid to the link between formation scenario and their hypothetical product (LMXB, TŻO, etc.). Along those lines, the stability of the build-up of an atmosphere around a neutron star has been in dispute ever since TŻ objects were conjectured. At the heart of this controversy is the impact of neutrino physics on the structure of the atmosphere. Neutrino cooling, an aspect of the problem first brought up by Bisnovatyi-Kogan & Lamzin (1984), dismissed by Eich et al. (1989) and subsequently ignored by Biehle (1991, 1994), Cannon et al. (1992) and Cannon (1993) has regained prominence as understanding of supernova fallback onto neutron stars has progressed. In particular, Chevalier (1993) has found that hypercritical accretion can occur, not only in the case of supernova fallback, but also in the entire range of common envelope systems, including TŻ objects.

This paper is about what occurs when a neutron star is forced to accrete matter at a high rate. A generic scenario might be as follows: a neutron star encounters a star (or a gas cloud, or an AGN disk, or its own ejecta). During an initial transient, an accretion shock moves from the surface of the neutron star to some equilibrium radius. The region inside the shock then becomes an atmosphere in near-pressure equilibrium which settles on the neutron star. Both of

these phases of the evolution can last for many dynamical times so that it is not possible to model the comprehensive evolution of the accreting neutron star. Since we would still like to determine what will be the final outcome, we have devised the following plan of attack: in a first set of simulations, we compute the evolution of a series of initial free-fall conditions over a range of parameters (entropy, chemical composition, and most importantly, infall rate). These conditions typify the expected initial structure obtained as a neutron star plows into a medium. For reasons explained in §2.4.1.1, the transient structure which develops while the accretion shock moves outward immediately becomes convectively unstable, pushing the accretion shock beyond its steady state radius. Unfortunately, the convective episode lasts too long to follow to completion, but the end result can be inferred, namely that an isentropic atmosphere will eventually build up above the neutron star. In a second set of simulations, we examine just such isentropic atmospheres initially in gravitational and pressure equilibrium for a range of entropy and chemical composition. In the absence of neutrino processes, these atmospheres are stable. Starting with these “pseudo-stable” initial conditions, we turn on neutrino processes and determine how stability is affected by energy losses due to neutrino emission. Combining these two sets of simulations, we can take a given infall structure and, using our first set of models, estimate the resulting structure of the isentropic atmosphere. With this structure, the second series of models will then predict the ultimate fate of the system.

Section 2.2 discusses the numerical methods used in our simulations and §2.3 presents the range of initial conditions and physical processes included in this study. The results, including comparisons to the work of Chevalier (1989, hereafter C89), Chevalier (1993), Houck & Chevalier (1991) (hereafter HC), and Colgate, Herant, & Benz (1993) (hereafter CHB), are presented in §2.4. We conclude with

a discussion of the implications of our findings for the variety of systems involving high mass infall and the potential observational consequences.

2.2. NUMERICAL METHODS

To explore the behavior of our range of atmospheres, we utilize both one-dimensional and two-dimensional codes. The one-dimensional code is used to determine the subset of atmospheres that develop negative entropy gradients of sufficient magnitudes to induce convection and thus break the otherwise spherical symmetry. This allows us to limit two-dimensional simulations to those atmospheres that really require it. All physical processes such as neutrino physics (absorption, emission and transport), equation of state, etc., are implemented in identical ways for both codes. The two codes have already been described in detail (Herant et al. 1994, hereafter HBHFC). Thus, we will limit ourselves to an overview except to describe modifications introduced specifically for these simulations.

2.2.1. One-dimensional Lagrangian Code

The one-dimensional simulations were performed with an explicit, grid-based, Lagrangian code (Benz 1991) using a second order Runge-Kutta integrator. This code does not include any form of convection modeling (mixing length or other), and as a result, its usefulness is limited to non-convective regimes, and to the diagnosis of the onset of convection. The neutron star surface is modeled by a reflective inner boundary, exterior to which lies the atmosphere. For most of the one-dimensional simulations we used a total of 140 cells modeling the pressure equilibrium atmospheres out to a radius ~ 2500 km and the infall atmospheres out to $\sim 25,000$ km. Since the mass of the atmosphere strongly depends on entropy for

the equilibrium models [see eq. (39)] and on the infall rate for the infall models [see eq. (13)], the mass resolution for the models varies according to the computed model. It was however chosen in such a way as to maximize resolution near the surface of the neutron star.

Both Newtonian and general relativistic (in the style of Van Riper 1979) formalisms have been implemented in the code. We have found that the general relativistic implementation leads to an increase in the Brunt-Väisälä frequency of up to 40% over the Newtonian case in the intermediate entropy models (see §2.4.2), and in addition, a factor of ~ 3 increase in accretion rates. These effects are comparable to those calculated by HC. However, since angular momentum and accretion concerns limit us to mostly qualitative estimates anyway, in most of the simulations presented here, general relativistic effects have been ignored.

2.2.2. Two-dimensional SPH Code

The basic structure of the two-dimensional cylindrical geometry smooth particle hydrodynamics (SPH) code used for the simulations of this paper has been presented in Herant & Benz (1992). The code was further developed in Herant, Benz, & Colgate (1992) and HBHFC to incorporate neutrino processes and an equation of state of extended range.

As in HBHFC we run our calculations in a wedge centered on the equatorial plane with periodic boundary conditions to avoid the complications associated with the z -axis which corresponds to a singularity of the cylindrical coordinate system. The opening angle is usually 90° corresponding to $\sqrt{2}/2$ of the total volume. We have varied the opening angle (up to 160°) and the number of particles [factors of 4 (4,000 - 16,000 particles)] in the simulations without noticing appreciable changes

in the results. The gravitational force is calculated in the Newtonian limit by evaluating the mass interior to each particle, thereby assuming spherical symmetry, which is reasonable considering that the central neutron star provides the dominant contribution. The kernel used is the same as in HBHFC.

The structure of the initial atmospheres (see §2.3.1) is mapped to an SPH representation. Particles are placed on concentric circles around the origin. There are of order 50 particles per circle, which in a 90° wedge translates to an angular resolution of a few degrees. As in the one-dimensional case, the mass of the particles is dependent upon the specific characteristics of the atmosphere being studied with the maximal mass resolution near the surface of the neutron star. Also similar to the one-dimensional code, a fixed, hard boundary represents the neutron star surface. Its implementation is as described in HBHFC. Once particles reach a critical density ($\rho > 10^{13} \text{ g cm}^{-3}$) and electron fraction ($Y_e < 0.1$), they are accreted onto the neutron star surface. In addition, an outer boundary was introduced to allow us to control the pressure of the outer atmosphere.

2.3. INITIAL CONDITIONS AND PHYSICAL PROCESSES

2.3.1. Initial Conditions

In most of our simulations, the neutron star has a $1.4 M_\odot$ gravitational mass and a radius of 10 km. Atmospheres with initially uniform entropy and chemical composition are constructed above the neutron star. Their initial density structure is determined by pressure equilibrium in the equilibrium atmosphere models, or by assigning a mass infall rate and assuming free-fall initial conditions for the infall

simulations. We considered initial compositions of pure iron, pure oxygen, and a primordial mix of hydrogen and helium. Because the temperature at the base of the atmosphere is usually high enough to lead to nuclear statistical equilibrium (NSE), the initial composition is important to determine the energy release from nuclear burning.

For the equilibrium atmosphere calculations, pressure equilibrium was verified in our code by allowing the atmosphere to evolve hydrodynamically without neutrino physics. For the two-dimensional simulations, inaccuracies in the mapping scheme from the one-dimensional structure lead to small initial transients which have to be damped, preserving constancy of entropy. In general however, the atmospheres were found to remain in equilibrium for times much longer than our simulation times.

2.3.2. Equation of State and Neutrinos Processes

The equation of state and neutrino processes are discussed in HBHFC to which the reader is referred for further details. The equation of state includes perfect gas, photon, and electron contributions to any degree of degeneracy and relativity (Nadezhin 1974; Blinnikov, Dunina-Barkovskaya, & Nadezhin 1995), and a nuclear equation of state (Lattimer & Swesty 1991). Additionally, when the temperature rises above 5×10^9 K, NSE (see Hix et al., 1995) is enforced to approximate the effect of nuclear burning, and to compute the free nucleon fraction which is important for neutrino emission and absorption. Although matter does burn at lower temperatures without going immediately into NSE, burning is a slow process compared to the hydrodynamics.

The neutrino emission processes accounted for include electron and positron

capture by free protons and neutrons, and pair and plasma neutrino–antineutrino creation. Neutrino absorption processes include electron neutrino capture by free neutrons, electron antineutrino by free protons, and neutrino antineutrino annihilation. Neutrino scattering includes electron and positron scattering of neutrinos, and neutral current opacities by nuclei. Three species of neutrinos are tracked separately by the transport algorithm: electron neutrino, electron antineutrino, and a generic “ τ ” neutrino bundling together μ and τ neutrinos and antineutrinos which have very similar characteristics in the regimes under consideration. The neutrino transport consists of two schemes: flux-limited diffusion for the optically thick regions and a light-bulb approximation for the optically thin regions. The light-bulb approximation was introduced for computational speed and is only valid if the absorbed neutrino luminosity ($L_{\nu_{\text{abs}}}$) in this regime is much less than the total neutrino luminosity ($L_{\nu_{\text{tot}}}$). In most of our calculations, we limit the $L_{\nu_{\text{abs}}}/L_{\nu_{\text{tot}}}$ to 10%. We have run test calculations limiting $L_{\nu_{\text{abs}}}/L_{\nu_{\text{tot}}}$ to 3% without appreciable changes in the results.

2.3.3. Infall rates and Assumptions

The objective of this paper is to determine the effects of neutrino processes on accretion for a range of initial conditions. We then apply our results to specific circumstances which lead to rapid infall on neutron stars. In this section, we discuss the probable infall rates for various scenarios and the suitability of our assumptions, which include ignoring the effects of angular momentum, magnetic fields, and photon diffusion.

Infall

The infall of matter onto a neutron star plowing through a medium is characterized for many, if not all, of the formation scenarios by Bondi-Hoyle “infall” and has been further studied numerically in a series of papers by Ruffert (1994a, b, 1995) and Ruffert & Arnett (1994). They compare numerical results to the canonical Bondi-Hoyle infall in a homogeneous medium, and introduce a new set of equations to estimate the infall rate. However, except at Mach numbers (M) close to 1, the infall rate is within 20 % of the canonical rate (it can increase by factors of 3 for $M = 1$ infall). Since we are only interested in rough estimates of the infall, we will use the simpler equations of Bondi-Hoyle-Lyttleton (Bondi 1952):

$$\dot{M}_B \approx 4\pi r_B^2 \rho (v^2 + c_s^2)^{1/2} \quad (1)$$

where the Bondi infall radius is

$$r_B = \frac{GM_{\text{NS}}}{v^2 + c_s^2}, \quad (2)$$

and G is the gravitational constant, ρ and c_s are the density and sound speed of the ambient medium. Table 2.1 lists the infall radii and infall rates for a neutron star plowing through stars (modeled with a stellar structure code developed by D. Arnett) of different masses and at different distances from the center for a range of impact velocities spanning possible high infall scenarios. Note that proper motion measurements of neutron stars imply an average spatial velocity of neutron stars on the order of 450 km s^{-1} and, in some cases, as high as 1000 km s^{-1} (Lyne & Lorimer Lyne & Lorimer 1994; Frail, Gross, & Whiteoak 1994). However, common envelope systems will involve much lower velocities ($\sim v_{\text{orbital}}$).

Angular Momentum

Estimating the effects of inhomogeneous media on Bondi-Hoyle accretion has been fraught with difficulties both from an analytic and numeric standpoint. Analytical approaches tend to depend heavily upon unphysical assumptions (sometimes assuming that the fluid flow system is identical to the standard Bondi-Hoyle structure for the homogeneous case) and in general, results have not been corroborated by simulations. Moreover, the lack of agreement among numerical endeavors has made their estimates equally inconclusive. A partial list of numerical studies representing the large variation in results includes: Davies & Pringle (1980); Fryxell & Taam (1988); Taam & Fryxell (1989); Sawada et al. (1989); Theuns & Jorissen (1993); and Ruffert & Anzer (1994). Most of these discrepancies are probably due to differences in resolution, boundary effects, or a difference in accretion between two- and three-dimensional models. However, the numerical simulations virtually all agree on two points: the average infall rate is within a factor of two of the Bondi-Hoyle infall (even though in many simulations the infall rate is seen to vary with time, e.g. the “flip-flop” instability seen by Fryxell and Taam), and the angular momentum accreted within the accretor radius (typically $0.1r_B$) is generally non-zero, but less than that predicted by a majority of the analytical estimates.

Despite these difficulties, we would like to try to evaluate, using currently favored numerical models, the effects of angular momentum on accretion. A typical estimation for angular momentum accretion is (see, for example, Ruffert & Anzer 1994):

$$j_z \equiv \dot{J}_z / \dot{M} = \frac{1}{4}(6\epsilon_v - \epsilon_\rho)Vr_B \quad (3)$$

where \dot{J}_z is the angular momentum accretion rate, \dot{M} is the mass accretion rate

and V is the velocity of the accretor, and $\epsilon_{v,\rho}$ are the inhomogeneity parameters defined as (Taam & Fryxell 1989):

$$\epsilon_{\rho,v} = r_B / H_{\rho,v} \quad (4)$$

where $H_{\rho,v}$ is the scale height of the density (ρ) or the velocity (including the sound speed, i.e. $(c_s^2 + v^2)^{1/2}$) profile perpendicular to the direction of motion of the accretor. Ruffert and Anzer consider a $V = 3c_s$ accretor in a $\epsilon_v = 0.3$ medium with an accretion radius one tenth the size of the Bondi radius. Their results give a 40% decrease in the angular momentum accreted in comparison to equation (3). Assuming no angular momentum is lost once the material passes within the accretion radius and using equation (3), one can determine an upper limit for the radius at which rotational support stops the infall (r_{ang}) of material (also shown in Table 2.1). This is most likely an over-estimate since, until an axisymmetric regime is attained, angular momentum can be effectively transported by pressure waves and shocks.

From r_{ang} inward, a thick accretion disk forms. For a thick α disk, the timescale for the outward transport of angular momentum is estimated to be (Chevalier 1993):

$$t_{\text{in}} \sim \frac{r_{\text{ang}}^2}{\alpha c_s H} \sim \frac{r_{\text{ang}}^{3/2}}{\alpha \sqrt{GM}} \sim r_8^{1.5} \text{ s} \quad (5)$$

where the sound speed (c_s) is approximated as the orbital velocity, H is the disk scale height and is estimated to be $\sim r_{\text{NS}}$, α is a measure of the viscous stress typically found to be $\sim .01 - .1$ (we use .07), and r_8 is r_{ang} in units of 10^8 cm. Once the material loses its angular momentum, it will accrete onto the neutron star. Thus t_{in} is essentially the time delay for the accretion of material. Since t_{in} is not much larger than the free-fall timescale, this delay should have a relatively small impact on the accretion rate.

Despite this discussion, we are aware that the question of the effect of angular momentum accretion is unsettled, and it will remain so until more comprehensive results from numerical and analytical calculations become available. However, we believe that in the case of buried neutron stars, the effect of angular momentum should be a perturbation on the classical Bondi regime. One reason is that the dynamics of self-gravitating, thick accretion disk is ripe with hydrodynamical instabilities (unlike cold, thin disks), which should allow rapid transport of angular momentum. Another reason for sustained accretion is that just as there exists a plane in which the angular momentum accreted is maximal, there is also a plane in which it is nil, and that is where the accreted matter may come from primarily (i.e. the polar direction in the case of an inspiral).

Photon Diffusion

Our current set of simulations is limited by the assumption that the photons are “trapped” within the infalling material. By trapped, we mean that the photons are carried inward with the accretion flow significantly faster than they can diffuse outward. As a result, we only consider cases for which the accretion rate is sufficiently high (infall models), or for which the entropy is not too large (equilibrium atmosphere models). We derive below the conditions for which the assumption of photon trapping is valid.

For equilibrium atmospheres, the timescale for neutrino cooling (τ_ν) sets the accretion rate and therefore the dynamical timescale. We can therefore compare the photon diffusion timescale (τ_γ , calculated near the surface of the neutron star since this is where the interesting dynamics occur) with τ_ν to determine the range of constant entropy, equilibrium atmospheres for which we can assume neutrinos

are trapped. Using the approximations for the structure of the equilibrium atmospheres derived in §2.4.2, we obtain:

$$\tau_\nu = E_{\text{reg}}/L_{\text{reg}} = 3.2 \times 10^{-12} S_{\text{rad}}^6 (1 + S_{\text{rad}}/55) \text{ s} \quad (6)$$

and

$$\tau_\gamma \approx \frac{r_{\text{scale}}^2}{\lambda_{\text{mfp}}^2} \frac{\lambda_{\text{mfp}}}{c} \quad (7)$$

where E_{reg} and L_{reg} are the energy and neutrino luminosity near the surface of the neutron star over the scale height r_{scale} [see equation (40)], S_{rad} is the radiation entropy of the atmosphere, λ_{mfp} is the mean free path of the photons, and c is the speed of light. For entropies in which $\tau_\gamma > \tau_\nu$, ($S < 600$ - see Fig. 2.1) the photons will be carried in with the accreting material and we can reliably assume that the photons are trapped. However, this argument implicitly relies upon a spherically symmetric inflow. When convection becomes important, we must once again examine the effects of this convection-enhanced photon diffusion. We will consider these specific cases as they appear in our equilibrium simulations.

For the infall atmospheres, we can use the infall rate to determine the inward motion of the material and compare it to photon diffusion. The trapping radius is then the radius where these speeds are equal and is commonly denoted (e.g. see Chevalier 1989):

$$r_{\text{tr}} = \min \left(\frac{\dot{M} \kappa}{4\pi c}, r_B \right) \quad (8)$$

where \dot{M} is the mass infall rate, κ is the opacity of the infalling material (we assumed $\kappa = 0.2 \text{ cm}^2 \text{ g}^{-1}$), c is the speed of light and r_B is the Bondi accretion radius. From Table 2.1, we see that the trapping radius for most neutron star encounters with stellar objects is close or equal to the Bondi radius and, as a result, the diffusion of photons is unimportant.

Magnetic Fields

We have assumed in our simulations that the magnetic field of the neutron star has no effect upon the hydrodynamics. This assumption is valid for two regimes; for neutron stars with low magnetic fields and for high infall rates which smother the magnetic field of the neutron star. The importance of magnetic fields can be estimated by finding the radius at which the magnetic energy density equals the kinetic energy density of the infalling matter (Shapiro & Teukolsky 1983):

$$\frac{B^2}{8\pi} = \frac{1}{2}\rho v_{\text{ff}}^2 \quad (9)$$

$$\Rightarrow \frac{\mu^2}{8\pi r_A^6} = \frac{1}{2} \frac{\dot{M}}{4\pi r_A^2 v_{\text{ff}}} v_{\text{ff}}^2 \quad (10)$$

Where B is the magnetic field, μ is the magnetic dipole moment, ρ is the density of the matter, v_{ff} is the free-fall velocity, r_A is the Alfvén radius and \dot{M} is the mass infall rate. To insure that magnetic fields are unimportant, the Alfvén radius should lie within the neutron star. For a 10^{12} Gauss magnetic field, the accretion rate has to be:

$$\dot{M} \gtrsim 0.8 M_{\odot} \text{ y}^{-1}. \quad (11)$$

Thus for high infall rates the infalling material effectively smothers even high magnetic fields and its trajectory is unaffected by them.

However, the above calculation may be overly conservative because it ignores the pile-up of material which occurs at lower infall rates. As the infalling material builds up around the neutron star, the pressure at the base of the atmosphere increases. In a more detailed analysis, Chevalier (1989) calculated the relative importance of radiation and magnetic pressure for this built-up material around

a neutron star. He found that for the radiation pressure to exceed the magnetic pressure at the surface of a 10^{13} Gauss neutron star, the infall rate need only exceed $5 \times 10^{-6} M_{\odot} \text{ y}^{-1}$, in support of our assumption that magnetic fields are unimportant at high accretion rates.

2.4. RESULTS

Following the strategy that we mapped out in the introduction, we present two sets of simulations for which the initial atmosphere structures were defined by either free-fall or pressure equilibrium conditions. Recall that the infall atmospheres model the likely initial conditions encountered by a neutron star entering a medium. The infall simulations provide clues to the structure of the developing atmosphere which, in most cases, will become similar to our second set of models, the equilibrium atmospheres. From the equilibrium atmosphere simulations, we can then determine the ultimate fate of these systems. In both cases, we found that the outcome is primarily dependent upon one parameter: the infall rate for the infall atmospheres and the entropy for equilibrium atmospheres. In this section, we also compare our results to prior analytical derivations obtained by C89 and HC for infall atmospheres and CHB for equilibrium atmospheres.

2.4.1. Infall Atmospheres

The structure of infall atmospheres has been discussed analytically by C89 and in more detail by HC and Brown (1995). The qualitative structure, and indeed much of the quantitative results, predicted by C89 is in good agreement with our numerical simulations. The density and pressure profiles derived by C89, with only a slight modification of the adiabatic index, match our numerical simulations

closely. Still, as we shall see further, the seemingly innocuous deviation of the adiabatic index for very high infall rates has non-negligible consequences on the overall hydrodynamical evolution. Yet of greater importance, convection adds a new dimension to the problem as high-entropy bubbles drive the accretion shock outward. We begin this section with a summary of conditions prevailing in steady state infall atmospheres, much along the ideas set forth by C89. We then go on to the analysis of the initial transient which occurs during the onset of accretion and has important consequences for the subsequent evolution. We then discuss our one-dimensional simulations and compare them to the work of C89. We end this section discussing the effects of convection on infall atmospheres.

Steady State Infall Structure

As a neutron star plows through an ambient medium, material within the Bondi infall radius is captured and falls inward. Initially, pressure forces are insignificant so that the infall structure is similar to that predicted by the free-fall solution. Rapidly however, “the sink backs up” as the Bondi infall rate [$\dot{M}_B = 4\pi r_B^2 \rho_{\text{ext}} (c_{\text{ext}}^2 + v_{\text{NS}}^2)^{1/2}$ where the “ext” subscript indicates the external density and sound speed] exceeds the acceptance rate determined by the cooling rates. As matter continues to crash down, it heats up and pressure increases until it is sufficient to slow down the infall by a shock. The accretion shock moves outward from the neutron star, until the flow structure (especially conditions in the neighborhood of the neutron star) allow neutrino losses to match the energy output due to accretion, or in the case of low infall rates, until the shock emerges from the optically thick domain. In the latter case, which we will not consider further, the accretion is Eddington-limited, while in the former case, neutrino cooling allows an

essentially unlimited accretion rate.

The accretion shock separates two distinct structural regions in the infall (see Fig. 2.2). Outside the shock, the infall can be characterized by the free-fall solution (see, for example C89):

$$v_{\text{ff}} = \sqrt{\frac{2GM}{r}} \quad (12)$$

and

$$\rho_{\text{ff}} = \frac{\dot{M}_B}{4\pi r^2 v_{\text{ff}}}, \quad (13)$$

where G is the gravitational constant, M is the neutron star mass and r is the distance from the center of the neutron star.

At the shock, using mass, momentum and energy conservation in addition to a perfect gas equation of state and assuming a strong shock, the shock jump conditions are (C89):

$$P_{\text{sh}} = \frac{\gamma + 1}{2} \rho_{\text{ff}} v_{\text{ff}}^2 \quad (14)$$

and

$$\rho_{\text{sh}} = \frac{\gamma + 1}{\gamma - 1} \rho_{\text{ff}} \quad (15)$$

where the pressure outside the shock is considered to be negligible (strong shock assumption) and γ is the adiabatic index.

Inside the shock front, in the settling region, we again turn to the conservation equations assuming spherical symmetry and that all initial transients set by the outmoving shock wave are quickly ironed out by convection (C89):

$$\partial \rho / \partial t + \nabla(\rho v) = 0 \quad \text{mass conservation,} \quad (16)$$

$$\partial v / \partial t + \nabla(v^2/2 + P/\rho) = F_T \quad \text{momentum conservation,} \quad (17)$$

and

$$P \propto \rho^\gamma \quad \text{adiabatic perfect gas,} \quad (18)$$

where F_T is the net external force (in our case, gravity). Steady state solutions demand that $\partial v/\partial t = \partial \rho/\partial t = 0$, so that the mass conservation equation becomes $4\pi r^2 \rho v = \text{const} = \dot{M}_B$. Moreover, right behind the shock radius, we have that $v^2/2 \ll P/\rho$ since the flow becomes subsonic ($v^2 < c_s^2 = \gamma P/\rho \propto \rho^{\gamma-1}$). From the mass conservation equation, $v^2 \propto \rho^{-2} r^{-4}$ so that the ratio $(v^2/2)/(P/\rho) \propto r^{-4} \rho^{-1-\gamma}$. Since ρ is obviously a decreasing function of radius, we have that $v^2/2 \ll P/\rho$ everywhere behind the shock. One can thus neglect the v^2 term in the momentum conservation equation (17) throughout the region behind the shock, so that the determination of the density and pressure becomes straightforward (C89).

$$\rho = \rho_{\text{sh}} \left(\frac{r}{r_{\text{sh}}} \right)^{-1/(\gamma-1)} \quad (19)$$

and

$$P = P_{\text{sh}} \left(\frac{r}{r_{\text{sh}}} \right)^{-\gamma/(\gamma-1)}. \quad (20)$$

As the pressure, and hence temperature, at the base of the atmosphere increases, the neutrino emission increases. Because of the low cross-section of interaction with matter ($\sigma_\nu = 10^{-43} \text{ cm}^2$ vs. $\sigma_\gamma = \sigma_T = 6 \times 10^{-25} \text{ cm}^2$), the neutrinos are not trapped like the photons and commence cooling the base of the atmosphere. An important cooling mechanism is the capture of electrons and positrons by free protons and neutrons with emission of electron neutrinos and anti-electron neutrinos respectively. In the regime where pairs dominate and the matter is completely dissociated into free nucleons (corresponding to a high temperature and entropy), the emission rate can be approximated by (Herant et al. 1992):

$$\frac{d\epsilon_{\text{nuc}}}{dt} = 2 \times 10^{18} T_{\text{MeV}}^6 \text{ erg g}^{-1} \text{ s}^{-1}. \quad (21)$$

Also important is the annihilation of electrons and positrons into neutrino antineutrino pairs of all flavors which, if pairs dominate, can be written as (Herant

et al. 1992):

$$\frac{d\epsilon_{pp}}{dt} = 1.9 \times 10^{25} \frac{T_{\text{MeV}}^9}{\rho} \text{ erg g}^{-1} \text{ s}^{-1}. \quad (22)$$

In steady state, the neutrino losses balance the gain in potential energy due to accretion;

$$4\pi r_{\text{NS}}^2 (\Delta r_{\text{ER}}) \rho \frac{d\epsilon_{\text{tot}}}{dt} = \frac{GM_{\text{NS}} \dot{M}_B}{r_{\text{NS}}} \quad (23)$$

where Δr_{ER} is the thickness of the emission region at the base of the atmosphere where most of the cooling takes place (one temperature scale height, $\sim r_{\text{NS}}/8$), $d\epsilon_{\text{tot}}/dt$ is the specific neutrino cooling rate from the neutrino emission processes [eqs. (21), (22)]. This last expression closes the set of equations that determines the steady state of the system and allows one to determine r_{sh} . For instance, we can use the approximation that the pressure is dominated by radiation at the base of the atmosphere (i.e. $P_{\text{atm}} = aT_{\text{atm}}^4$, $\gamma = 4/3$) to determine the temperature at the base of the atmosphere from equations (12)-(20), and thus the cooling rate for free nucleon emission:

$$\frac{d\epsilon_{\text{nuc}}}{dt} = 8.5 \times 10^{15} \left(\frac{M}{1.4 M_{\odot}} \right)^{3/4} \left(\frac{\dot{M}_B}{M_{\odot} \text{ y}^{-1}} \right)^{3/2} \left(\frac{r_{\text{NS}}}{10 \text{ km}} \right)^{-6} \left(\frac{r_{\text{sh}}}{100 \text{ km}} \right)^{9/4} \text{ erg g}^{-1} \text{ s}^{-1}, \quad (24)$$

and pair annihilation:

$$\frac{d\epsilon_{pp}}{dt} = 9.2 \times 10^{16} \left(\frac{M}{1.4 M_{\odot}} \right)^{13/8} \left(\frac{\dot{M}_B}{M_{\odot} \text{ y}^{-1}} \right)^{5/4} \left(\frac{r_{\text{NS}}}{10 \text{ km}} \right)^{-6} \left(\frac{r_{\text{sh}}}{100 \text{ km}} \right)^{15/8} \text{ erg g}^{-1} \text{ s}^{-1}. \quad (25)$$

For most steady-state accretion scenarios, the pair annihilation emission process dominates the cooling, so we will ignore nucleon emission in determining r_{sh} .

Assuming a 10 km, $1.4 M_{\odot}$ neutron star, we obtain a result similar to C89:

$$r_{\text{sh}}^{\gamma=4/3} = 6.7 \times 10^8 \dot{M}_B^{-10/27} \text{ cm}, \quad (26)$$

where \dot{M}_B is in $M_{\odot} \text{ y}^{-1}$. Our neutrino emission processes are slightly different from those in C89 which, combined with a different value for the emission region

(we used r_{NS} , accounts for the slight differences between the two solutions. We can repeat this derivation for various values of gamma to obtain:

$$r_{\text{sh}}^{\gamma=1.37} = 3.3 \times 10^9 \dot{M}_B^{-0.46} \text{ cm} \quad (27)$$

and

$$r_{\text{sh}}^{\gamma=1.4} = 1.7 \times 10^{10} \dot{M}_B^{-0.56} \text{ cm}. \quad (28)$$

The Onset of Accretion and the Initial Transient

We now leave the steady state solution and return to the analysis of the initial transient which takes place at the beginning of the evolution. During the initial phase of the accretion, the shock moves out from the surface of the neutron star towards its steady-state position r_{sh} . As a result, the post-shock entropy decreases as the accretion shock progresses outwards and weakens. Assuming that radiation dominates, but that electrons are non-relativistic (which is reasonable away from direct proximity of the neutron star), the post-shock entropy can be written $S_{\text{sh}} = 1.1 \times 10^{-11} P_{\text{sh}}^{3/4} / \rho_{\text{sh}}$. We can then apply the shock equations (14) and (15) and the free-fall equations (12) and (13) to determine the entropy for a given shock radius and infall rate:

$$S = 5.5 \times 10^3 \frac{((\gamma + 1)/2)^{3/4}}{(\gamma + 1)/(\gamma - 1)} M_{\text{NS}}^{7/8} \dot{M}_B^{-1/4} r_6^{-3/8} \quad (29)$$

where S is in k_B per nucleon, M_{NS} is the mass of the neutron star in solar masses, \dot{M}_B is the infall rate in $M_{\odot} \text{ y}^{-1}$, and r_6 is the radius of the shock in units of 10^6 cm . Note that in the strong shock regime (which applies if the shock radius remains much smaller than the Bondi radius), the entropy below the shock is independent of the entropy above the shock. Consequently, in most of our simulations, the initial entropy of the infalling material has little effect on the resulting structure.

Because of the dependence on radius (exponent $-3/8$) of the postshock entropy, the outward motion of the shock imprints a negative entropy gradient in the inner region during the initial transient. This entropy profile is evidently unstable and leads to a break in the spherical symmetry which is not included in the picture developed in C89. The timescale for convection can be approximated using the Brunt-Väisälä frequency N (see Cox, Vauclair, & Zahn 1983):

$$N^2 = \frac{g}{\rho} \left(\frac{\partial \rho}{\partial S} \right)_P \frac{\partial S}{\partial r}. \quad (30)$$

For $\partial S / \partial z < 0$, $N^2 < 0$ and the atmosphere is unstable. The timescale for this convection (τ_{conv}) is $\sqrt{|1/N^2|}$. Of course, convective instability can also depend on the chemical composition as an atmosphere may be stabilized by a negative gradient of the molecular weight. However, the entropy gradients are sufficiently high in our simulations that this is not a concern. The region within the accretion shock convects until stability is achieved and ultimately develops into an equilibrium atmosphere.

An additional effect of this initial convection is to drive the shock beyond its steady-state value, lowering the entropy at the shock [eq. (29)] with respect to the steady-state prediction. This material ultimately makes its way down to the base of the atmosphere, defining the entropy of the equilibrium atmosphere. Since the base of the atmosphere depends on its entropy, this convection-driven overshoot can drastically alter the evolution of the system. Equilibrium atmospheres and the effect of the initial transient on their entropy will be addressed in §2.4.2.

However, this description does not apply to extremely high infall rates. Beginning from the free-fall solution of matter crashing down on the neutron star surface we have:

$$\frac{GM_{\text{NS}}\rho_{\text{atm}}}{r_{\text{NS}}} = aT_{\text{atm}}^4 \quad (31)$$

so that the temperature at the bottom of the atmosphere is proportional to the density at the bottom of the atmosphere to the one-fourth power: $T_{\text{atm}} \propto \rho_{\text{atm}}^{1/4}$. From mass conservation, we also have that $\rho_{\text{atm}} \propto \dot{M}$, and as a result $T_{\text{atm}} \propto \dot{M}^{1/4}$. Since neutrino cooling has a high power dependence on temperature (see section 2.4.2) there exists a critical mass infall rate beyond which the accretion shock can hover right above the neutron star and provide a sufficiently high temperature for neutrino cooling to allow accretion to take place immediately. In our simulations, this occurs at infall rates upward of $10^5 M_{\odot} \text{ y}^{-1}$ (see Table 2.2). The critical infall rates are slightly higher for the higher initial entropy atmospheres due to their lower initial neutrino luminosities.

Thus, rapid mass infall atmospheres lead to three distinct regimes. For a low rate of infall, material builds up around the neutron star and sends an accretion shock outward from the core. The unstable negative entropy gradient inprinted by the motion of the shock leads to instabilities. The low-entropy matter at the shock is convected downward onto the neutron star, and eventually an equilibrium atmosphere forms, with the range of outcomes discussed in section 2.4.2. Intermediate rates of infall initially lead to similar situations. However, the intense neutrino emission leads to cooling times shorter than the convective time, thus preventing the formation of an equilibrium atmosphere. For a high rate of infall, the material is shocked at close proximity of the neutron star surface and cools efficiently through neutrino emission without further ado.

One-dimensional Simulations

We have modeled a series of infalls for a range of infall rates and initial entropies. The results from the one-dimensional simulations are shown in Table

2.2. Note that the initial entropy has little impact, except in mass accretion rates near the transition between high and intermediate infall regimes.

Although the structure of the infall atmosphere is reasonably well described by the analytical derivation of C89, we found that the effective adiabatic index γ from our more detailed equation of state is slightly higher than the radiation dominated $4/3$ assumed by C89 (see Fig. 2.3). For infall rates below $1 M_{\odot} \text{ y}^{-1}$, this deviation is too small to have a significant impact on the flow structure, but for higher infall rates, it has a crucial influence on the steady state position of the shock. Figure 2.4 shows r_{sh} versus accretion rates for a range adiabatic indices (1.33, 1.37, 1.40) using equations (26-28). Note that by merely changing γ from $4/3$ to $4.2/3$ for the $100 M_{\odot} \text{ y}^{-1}$ simulation changes r_{sh} by an order of magnitude. This is important because, as we have seen in the previous section, the position where the shock stalls determines the entropy of the atmosphere which develops in the inner region in the vicinity of the neutron star. As we shall discuss in section 2.4.1, this entropy determines the ultimate fate of the atmosphere.

Figure 5 shows the entropy profile established by the transient motion of the shock from the surface of the neutron star toward its steady state radius. As predicted by equation (29), the entropy gradient is negative and will thus be subject to convective instabilities. Table 2.2 lists Brunt-Väisälä timescales along with neutrino luminosities, effective γ 's, and central entropies for all the one-dimensional simulations. It is clear, however, that multidimensional simulations are needed to calculate the subsequent evolution.

Two-dimensional Simulations

Since the high infall regime is not conducive to instabilities, we have limited our two-dimensional simulations to intermediate and low rates of infall. These atmospheres become active quickly (recall the short Brunt-Väisälä timescales) sending bubbles outward through the inner region. These bubbles contribute to the outward push of the shock, while plumes of low-entropy material stream down towards the neutron star (see Fig. 6). To better appreciate the properties of infalling atmospheres, the distinction between intermediate and low infall atmospheres needs to be elucidated. In addition, for the low infall regimes, we would like to determine the entropy of the resulting equilibrium atmosphere. As stated in the introduction, due to the relatively long convecting timescales ($> 10^4$ s), it is impossible to simulate a complete convective turn over as the Courant time step restriction near the neutron star is of order of tens of μ s. Nevertheless, the simulations seem to have reached steady-state, indicating that we may understand the long-term behavior of the system. allowing us to predict the ultimate outcome of the evolution.

In our simulations, we have noticed that the typical velocity of an infalling plume of material travelling between the shock and the neutron star is ~ 0.1 the free-fall velocity. Knowing this, we can estimate the convective turnover timescale (see Table 2.3):

$$\tau_{\text{conv}} = 10 t_{\text{dyn}} = 10 \frac{\pi r}{c_s} = 10 \frac{\pi r^{1.5}}{\sqrt{GM_{ns}}} \quad (32)$$

where t_{dyn} is the dynamical timescale, r is the radius of the material to be convected inward; τ_{conv} is the time to advect material from the shock to the neutron star surface. The time τ_{conv} must be compared with the time τ_{BH} required for the neutron star to accrete enough material to collapse into a black hole (see Table

2.3):

$$\tau_{\text{BH}} = \frac{1}{L_\nu} \frac{GM_{\text{NS}}m}{r_{\text{NS}}} \quad (33)$$

where L_ν is the total neutrino emission per unit time, m is the additional mass required to induce collapse (we use $0.2 M_\odot$), and r_{NS} is the neutron star radius. When $\tau_{\text{conv}} > \tau_{\text{BH}}$ which corresponds to the case of intermediate rate of infall, we expect the neutron star to collapse into a black hole before an equilibrium atmosphere can be formed. However, when $\tau_{\text{conv}} < \tau_{\text{BH}}$, which corresponds to low rates of infall, there is sufficient time for convection to form an equilibrium atmosphere. In these cases, we can use equation (29) to determine the resultant entropy for the equilibrium atmosphere.

These results can be approximately summarized as follows. Very high rates of infall ($\dot{M} \gtrsim 10^6 M_\odot \text{y}^{-1}$ – Note that these numbers are estimates as these rates depend on additional factors such as the Bondi radius and initial atmosphere entropy) clamp the shock close to the neutron star and lead to rapid accretion and black hole formation. An intermediate rate of infall ($10^3 M_\odot \text{y}^{-1} \lesssim \dot{M} \lesssim 10^6 M_\odot \text{y}^{-1}$) does not have the time to form a proper atmosphere as it rapidly leads to collapse into a black hole. Low rates of infall ($\dot{M} \lesssim 10^3 M_\odot \text{y}^{-1}$) allow sufficient time for an equilibrium atmosphere to develop. The structure and fate of these equilibrium atmosphere are discussed in the next section.

2.4.2. Equilibrium Atmospheres

In the previous section, we have studied the initial development of an accretion structure around a neutron star encountering an external medium. We now turn to the ultimate fate of these systems after convective stability has been achieved. Given the condition of initial pressure equilibrium, the most massive atmosphere that can form stably above a neutron star is isentropic, where the entropy is

determined by whichever density and temperature is chosen at the surface of the neutron star. More massive atmospheres can be constructed with a negative entropy gradient, but they are unstable to convection. Because even a small negative entropy gradient rapidly drives convection [see eq. (30) for convective timescale], stellar models always adjust themselves to constant entropy or positive entropy gradient structures. We expect the same situation for atmospheres around neutron stars. Consequently, we believe that the most simple and appropriate way to parametrize the set of the possible atmospheres is to use isentropic initial conditions.

The analytical work of CHB has examined the characteristics of constant entropy equilibrium atmospheres with the additional assumption that the pressure and internal energy are dominated by radiation and electron pairs contributions (that is, $P = 11/12aT^4$). This remains valid at the base of the atmosphere for entropies less than $400 k_B/\text{nucleon}$ [see eq. (38)] and larger than $30 k_B/\text{nucleon}$. The radiation component of the entropy (in units of Boltzman factor per nucleon) can then be expressed (CHB):

$$S_{\text{rad}} = \frac{4}{3} \times \frac{11}{4} a T^3 / (\rho k_B N_A) = 1.4 \times 10^{-11} P^{3/4} / \rho = 5.2 \times 10^8 T_{\text{MeV}}^3 / \rho \quad (34)$$

This expression is valid when the entropy and temperature are high. For high entropies, $S_{\text{rad}} \approx S_{\text{tot}}$, so that the analytical derivations can be compared directly to our models with increasing accuracy the higher the entropy.

Assuming constant entropy and a radiation pressure dominated system, one can use the hydrostatic equation of pressure equilibrium to derive the structure of the atmosphere (CHB).

$$P = \left[\frac{1}{4} M_{\text{NS}} G (S_{\text{rad}}/S_0)^{-1} (1/r - 1/r_1) + P_1^{1/4} \right]^4 \quad \text{dyne cm}^{-2}, \quad (35)$$

where $S_0 = 1.4 \times 10^{-11} k_B/\text{nucleon}$ with r_1 and P_1 referring to the radius and pressure at the outer boundary. Implicit to this derivation is that the mass of the atmosphere is negligible when compared to the neutron star mass. As we shall see, for high-entropy atmospheres, this is a good assumption.

In most cases, the radius of the outer boundary is sufficiently large that the terms involving r_1 and P_1 can be neglected. In the equilibrium simulations, we have included varying degrees of boundary pressure (motivated in part by the computed pressure of the infalling material from our infall simulations - §2.4.1). Thus, we have incorporated the full equations in our comparison with the analytic solutions. Nonetheless, the basic structure of the atmospheres changes very little (less than a factor of 2 for even the most extreme external pressures) by ignoring the boundary conditions, so we will present the structure equations in their simple, $P_1 = 0$, $r_1 \gg r_{\text{NS}}$ form (CHB):

$$P_{\text{atm}} = 1.83 \times 10^{35} S_{\text{rad}}^{-4} r_6^{-4} \text{ dyne cm}^{-2}, \quad (36)$$

and using equation (34), we find,

$$\rho_{\text{atm}} = 3.9 \times 10^{15} S_{\text{rad}}^{-4} r_6^{-3} \text{ g cm}^{-3}, \quad (37)$$

$$T_{\text{atm}} = 195 S_{\text{rad}}^{-1} r_6^{-1} \text{ MeV}, \quad (38)$$

$$M_{\text{atm}} = 24.5 S_{\text{rad}}^{-4} \ln(r_{\text{max}}/r_{\text{NS}}), \quad M_{\odot} \quad (39)$$

where r_6 is the radius in units of 10^6 cm, and S_{rad} is the radiation entropy in units of $k_B/\text{nucleon}$. These expressions assume a $1.4 M_{\odot}$ neutron star, as in our simulations. The most significant consequence of setting $P_1 = 0$ and $r_1 \gg r_{\text{NS}}$ is in the total mass of the atmosphere, M_{atm} . Figure 2.7 plots M_{atm} as a function of entropy for an outer radius of the atmosphere of 10^9 cm and 10^{13} cm using

equation (39) in the case of no external pressure (dashed lines) and additional external pressure (solid lines). When present, the external pressure was determined using our infall models (see §2.4.1) to find the maximum realistic infall pressure ($P_{\text{infall}} = \frac{1}{2}\rho_{\text{ff}}v_{\text{ff}}^2$) at a given radius and entropy. These lines represent the maximum achievable mass for a *stable* atmosphere of the prescribed radius and entropy. Note that despite the fact that constant entropy structures are the most massive stable atmospheres, their masses tend to be small. More massive atmosphere would require a negative entropy gradient which would then be convectively unstable.

Using equations (21), (22) combined with the structure equations for temperature and density, it is apparent that the neutrino energy emission per gram falls off roughly as r^{-6} , implying that most of the neutrino emission (and hence cooling of material) occurs close to the neutron star. We estimated the cooling rate by assuming a nearly constant neutrino cooling over a scale height of the emission region (subscript “ER”) $r_{\text{ER}} = r_{\text{NS}}/8$ above the neutron star and calculating the neutrino luminosity per gram in this region. The mass accretion is then:

$$\dot{M} = M_{\text{ER}}L_{\text{ER}}/E_{\text{ER}} \quad (40)$$

where M_{ER} is the mass within a scale height of the neutron star, L_{ER} is the neutrino emission from that region using equations (21) and (22), and E_{ER} was chosen (somewhat arbitrarily) to be half the potential energy $GM_{\text{NS}}M_{\text{ER}}/(r_{\text{NS}} + r_{\text{ER}})$ gained by the material falling from infinity. Combining these equations and using the $P_1 = 0$ atmosphere structure, we obtain:

$$\dot{M} = 9.0 \times 10^{11} S_{\text{rad}}^{-10} (1 + S_{\text{rad}}/55) \quad M_{\odot} \text{ s}^{-1} \quad (41)$$

Neutrinos emitted at the base of the atmosphere can be recaptured and heat matter higher up. This is especially important for low- and intermediate-entropy

atmospheres ($S < 50$). Neutrino absorption by free nucleons gives rise to the following heating term (Herant et al. 1992):

$$\frac{d\epsilon}{dt} = 4.8 \times 10^{32} \frac{L_\nu}{4\pi r^2} T_\nu^2 \quad \text{erg g}^{-1} \text{ s}^{-1} \quad (42)$$

where L_ν is the electron neutrino luminosity (in $10^{51} \text{ erg s}^{-1}$) which is due to neutrino emission at the base of the atmosphere, and T_ν is the neutrino temperature which tends to be similar to the matter temperature near the surface of the neutron star. We have seen earlier that cooling is proportional to r^{-6} , while it appears that heating is proportional to r^{-2} . One therefore expects that there exists a radius separating an inner region where cooling dominates from an outer region where there is a net gain in energy from neutrino processes. This is known in supernova circles as the gain radius.

The preceding equations give an analytical picture of the dominant physical processes involved for atmospheres in which photons are trapped. Note that nuclear burning effects were ignored. In our simulations, we have noticed that the initial chemical composition of the atmospheres has little effect upon the end result. As was seen analytically, we find that the primary parameter characterizing the atmospheres is entropy. For a low-entropy atmosphere, an immediate explosion is generated by the intense emission of neutrinos and the resulting energy deposition just beyond the gain radius. Intermediate ranges for entropy still exhibit noticeable effects from neutrino heating which induce convection. For these entropies, two-dimensional simulations of the atmospheres are required to fully investigate the hydrodynamical evolution. For high-entropy atmospheres, neutrino heating turns out to be unimportant, and hence there is no convection. However, neutrino cooling continues to determine the accretion rates up to extremely high entropies. These results are summarized in Table 2.4, and presented in more details in the

following sections.

Low-entropy Atmospheres

Figure 2.1 shows the sound travel time (τ_s) through the neutrino emission region together with neutrino cooling and photon diffusion time scales. For $S_{\text{rad}} \lesssim 14 \, k_B/\text{nucleon}$, which corresponds to $S_{\text{tot}} \lesssim 22 \, k_B/\text{nucleon}$ for our simulations, we find that the neutrino cooling time is faster than the sound travel time. Because of this, it is physically impossible to form such an atmosphere in hydrostatic equilibrium. It is thus unlikely that equilibrium atmospheres with low entropies can exist. Just to see what would happen, we have constructed such atmospheres in pressure equilibrium artificially maintained by ignoring neutrino effects. These atmospheres lead to neutrino-driven explosions as soon as neutrino processes are turned on. Despite the fact that they are unphysical, low-entropy atmospheres illustrate the importance of neutrino energy deposition beyond the gain radius. This process also plays a critical role in the more physical scenarios of supernova explosion, or in intermediate entropy atmospheres which are discussed below.

Intermediate-entropy Atmospheres

For atmospheres within a range of intermediate entropies ($30 \lesssim S_{\text{tot}} \lesssim 50$), the sound crossing time is much less than the neutrino cooling time ($\tau_s \lesssim 0.01\tau_\nu$), allowing the formation of atmospheres in pressure equilibrium. However, neutrino deposition is still sufficiently strong to heat the atmosphere just beyond the gain radius and thus raise the otherwise constant entropy of this region above the value

of the rest of the atmosphere. The resulting negative entropy gradient is unstable and convection takes place. In supernova simulations (HBHFC), this convection increases the efficiency of neutrino heating leading eventually to an explosion. In the context of our simulations, in order for the convection to be important, it must be able to overcome the general advection inward resulting from the sharp decrease in pressure support as material near the neutron star surface is quickly cooled by neutrino emission. Or in simpler terms, the bubbles have to rise faster than they are dragged inward by the general accretion flow. We can estimate the relative importance of these effects in the atmosphere by comparing the Brunt-Väisälä and infall time scales (see Table 2.4). Evidently, multidimensional simulations are required to correctly model these phenomena.

Figure 2.8 shows the effects neutrino heating for an $S_{\text{tot}} = 50$ atmosphere on the entropy profile in a one-dimensional computation. While neutrino cooling rapidly decreases the entropy at the base of the atmosphere near the neutron star, neutrino absorption further up leads to the formation of an entropy peak and an associated negative entropy gradient which will drive convective instabilities. When the same atmosphere is simulated in two dimensions, large scale convection arises from the neutrino induced negative entropy gradient as can be seen in Figure 2.9. Within this entropy range, the two-dimensional calculations resulted in the expulsion of the atmosphere in what might be considered a “mini-supernova” (see Fig. 2.10). Table 2.4 gives explosion energies for atmospheres of different entropies. The energies are much lower than supernova energies primarily due to the low mass of the atmospheres ($M_{\text{atm}}(1000 \text{ km}) \sim 10^{-5} - 10^{-3} M_{\odot}$).

Rather than trap the released gravitational energy near the surface of the neutron star to be ultimately emitted in neutrinos, convective bubbles transport

the energy up through the atmosphere as they rise. Such extensive convection raises the question whether our one-dimensional analysis which showed photon diffusion to be negligible is still valid. However, given the short timescales required for the explosion to develop in our simulations, photon diffusion remains unimportant. For example, in the worst case scenario of our $S_{\text{tot}} = 50$ atmosphere after 0.5 s (see Fig. 2.10), we find from equations (37) and (7) that photons at 2000 km diffused less than 1.5 km during the course of the simulation, a fraction of the particle size at that radius.

High-entropy Atmospheres

In the case of high-entropy atmospheres ($S_{\text{tot}} \gtrsim 60$), neutrino deposition has little effect upon the infalling atmosphere. Neutrino emission, however, remains an efficient source of cooling for all our simulations which extend up to $S_{\text{tot}} = 125$. In fact, neutrino losses dominate photon losses up to $S_{\text{tot}} = 600$ (Fig. 2.1).

Figure 2.11 plots the entropy profile at discrete time intervals (80 ms) for a typical one-dimensional run ($S_{\text{tot}} = 80$). The cooled, low-entropy matter consists primarily of neutrons ($Y_e \sim 0.1$) and has essentially become part of the neutron star. Note that for these high-entropy atmospheres, no entropy “bump” develops through neutrino heating. Figure 2.12 shows the neutrino luminosities and mean energies vs. time. The neutrino luminosity increases initially and then stabilizes, indicating a constant rate of accretion for the duration of the simulation. In essence, the system has reached a steady state in which the neutrino emission exactly balances the compression work done by gravity on the gas settling on the neutron star. In these conditions, hypercritical accretion is maintained until the neutron star collapses into a black hole.

For each simulation, the constancy of the accretion rate was verified by fitting the accreted mass vs. time with a straight line (see Fig. 2.13 for a typical fit), and the r.m.s. deviation was estimated. Figure 2.14 presents a comparison between the accretion rate calculated analytically and numerically as a function of atmosphere total entropy. The open symbols were plotted using a straight insertion of the total entropy while the filled symbols were plotted by computing the radiation entropy from the numerical simulations and using this value in equation (40). The remarkable agreement between analytical and numerical calculations (when the radiation entropy is used) shows that our models are self-consistent. In addition, we note that as entropy increases, the difference between S_{tot} and S_{rad} becomes smaller and smaller. Together with the good agreement with the CHB model, this allows us to extrapolate the behavior of our atmospheres beyond the range of entropies that we have simulated.

Figure 2.15 show the analytical accretion rates for high-entropy atmospheres. The lower and upper curves represent the cases with no external pressure, and with external pressure at 1000 km of 0.25% the pressure at the surface of the neutron star respectively. Of course, in reality the external pressure on the atmosphere is determined by the formation mechanism. However, the limits that we have chosen bound the results from all our infall models (see section 2.4.1) and it is unlikely that any of the formation mechanisms will produce atmospheres with external pressures beyond these limits. Note also that photons are still trapped out to 100 times the neutron star radius at an entropy $\sim 600 k_B/\text{nucleon}$, which is over a factor of ten times higher than typical stellar entropy values.

2.4.3. Summary of Results

We are now in position to tie together our studies of infall models with the behavior observed in our equilibrium atmosphere simulation, to create a complete picture of the evolution of rapid accretion onto neutron stars (see table 2.5). As we know from section 2.4.2, if the entropy is greater than ~ 600 , then the atmosphere is stable over long time scales. For $600 < S < 50$, the atmosphere accretes hypercritically. But for $50 < S < 30$, neutrinos heat the base of the atmosphere, ultimately leading to explosions. The mass accreted before the explosion is $M_{\text{exp}} = \dot{M}\tau_{\text{exp}}$, where $\dot{M} = (GM_{\text{NS}}/r_{\text{NS}})/L_{\nu}$ and $\tau_{\text{exp}} \sim \tau_{\text{conv}}$. These values are shown in Table 2.3. The final results for the objects in Table 2.1 are listed in the last column. Immediate collapse designates atmospheres in the high or intermediate regimes, $S > 600$ atmospheres are stable, $600 < S < 50$ atmospheres suffer delayed collapse, and $50 < S < 30$ atmospheres result in explosions.

We will now summarize these results in terms of accretion rates. Very high rates of infall ($\dot{M} \gtrsim 10^6 M_{\odot}\text{y}^{-1}$) clamp the shock close to the neutron star and lead to rapid accretion and black hole formation. Very low rates of infall ($\dot{M} \lesssim 10^{-4} M_{\odot}\text{y}^{-1}$) allow the entropy to rise to about $600 k_b/\text{nucleon}$ and form a stable atmosphere lasting many dynamical times. Low rates ($10^{-4} M_{\odot}\text{y}^{-1} \lesssim \dot{M} \lesssim 0.1 M_{\odot}\text{y}^{-1}$) of infall form a stable atmosphere in near pressure equilibrium which nonetheless accretes hypercritically and lead to the eventual formation of a black hole. Medium-low ($0.1 M_{\odot}\text{y}^{-1} \lesssim \dot{M} \lesssim 10^3 M_{\odot}\text{y}^{-1}$) rates of infall also form a stable atmosphere in near pressure equilibrium but neutrino heating eventually leads to an explosion rather than black hole formation. Finally, an intermediate rate of infall ($10^3 M_{\odot}\text{y}^{-1} \lesssim \dot{M} \lesssim 10^6 M_{\odot}\text{y}^{-1}$) does not have the time to form a proper atmosphere as it rapidly leads to collapse into a black hole.

2.4.4. Initial Transient Revisited

We have implicitly assumed in §2.4.3 that the initial transients define the fate of the system. However, if a system evolves into a steady state, this steady state can be maintained as long as any variations in the infall rate are sufficiently slow that the atmosphere can adapt to the changes before vigorous convection develops. The ultimate fate of the system is identical under the steady-state solution and the transient solution for all regimes except the medium-low regime which results in explosions. We will thus limit this discussion to the specific cases where a steady-state system evolves and then the infall rate is gradually changed to place it in the medium-low regime. If the steady state is maintained, the boundary between low and medium-low regimes will rise, limiting the range of atmospheres that fall into the medium-low regime. In this section, we will estimate how slow the infall rate must change to maintain the steady state system under various developments of the infall rate and the modifications to the results if a steady state is maintained.

We will consider two possible scenarios in which we begin with a steady state system and then modify the infall rate: a very high initial rate ($\dot{M} \gtrsim 10^3 M_{\odot} \text{y}^{-1}$) corresponding to supernova fallback, and a low initial rate ($\dot{M} \lesssim 10^{-4} M_{\odot} \text{y}^{-1}$) corresponding to stellar encounters. For the very high initial rate, a steady state system can not be formed because the convection timescale is longer than the timescale for the neutron star to accrete sufficient material to become a black hole. For low initial infall rates, a steady state system can form and be maintained with a sufficiently slow increase in the infall rate.

As we increase the infall rate on an initial equilibrium atmosphere, the entropy of the material at the shock radius decreases, becoming lower than the entropy of the equilibrium atmosphere. This system is then unstable to convection. If

convection can equilibrate this disparity in entropy before the entropy changes sufficiently to cause vigorous convection, then the system will remain in steady state. We can estimate a minimum timescale required for the convection from our calculation of the convective turnover timescale [see eq. (32)]. This timescale was derived assuming the same vigorous convection which we are trying to avoid and is, therefore, certainly an underestimate of the time required. At a radius of 10^{11}cm , the vigorous convective timescale is $1.6 \times 10^4\text{s}$. We will discuss the details of convection in the appendix from which we determine that for density enhancements greater than $\sim 20\%$, the convective velocity rises within a factor of 2 of the sound speed, which is too fast to model under the mixing length algorithm. We will define “vigorous” convection to begin where mixing length fails. With this approximation and using equation (13), we notice that only for situations where \dot{M} changes by less than 20% over the convective timescale can a steady-state system be maintained. From Table 2.1, we see that even this underestimate of the timescale precludes most collision formation scenarios, but allows for the possibility to maintain a steady state in common envelope systems.

As mentioned in section 2.4.3, for $50 < S < 30$ atmospheres, neutrino heating leads to an explosion. Assuming that the initial transient defines the entropy profile, these entropies are achieved for $\dot{M} \gtrsim 0.1 M_{\odot}\text{y}^{-1}$. In the steady state solution, we can use equation (29) and equations (26-28) to determine the infall rate above which the equilibrium atmosphere entropy is less than 50: $\dot{M}_{crit} = 20 M_{\odot}\text{y}^{-1}$. Thus, if a steady state is maintained, the critical infall rate between the low (hypercritical accretion) regime and the medium-low (explosion) regime will move from $0.1 M_{\odot}\text{y}^{-1}$ to $20 M_{\odot}\text{y}^{-1}$.

2.5. IMPLICATIONS

We can now apply the results from the two sets of simulations to a range of astrophysical situations involving high infall rates onto neutron stars. In this section, we discuss neutron star accretion in the context of TŻ objects, common envelope systems, neutron stars in dense molecular clouds, and supernovae.

Because our two-dimensional simulations invalidate a number of results previously obtained in one dimension, we present a criterion for the appropriateness of the mixing length algorithm to model convection. Further, the discussion of specific systems provides examples of the methodology in applying our results to the study of other objects. We end this work with a brief discussion of the observational properties of the explosion regime and a note on plans for future work.

2.5.1. TŻ Objects

All the formation scenarios for TŻ objects discussed previously (see §2.1) involve a neutron star spiralling into a red giant star. As it approaches the core, the infall rate becomes high. For example, a neutron star moving at 100 km s^{-1} at a radius of $5 \times 10^{10} \text{ cm}$ inside a $20 M_{\odot}$ giant has a mass infall rate of $1.8 \times 10^6 M_{\odot} \text{ y}^{-1}$ (again, we use the stellar evolution code by D. Arnett). We can easily verify that all our assumptions hold. That is, the time delay due to angular momentum transport is short ($\sim 0.5 \text{ s}$) and the impact of rotational support is minimal (see §2.3.3), magnetic fields $\lesssim 10^{15} \text{ Gauss}$ will be buried by the inflow of material (see §2.3.3), and photons will be trapped out to the Bondi accretion radius (see §2.3.3). Looking at Tables 2.3 and 2.4, we see that this infall fits into the intermediate regime, which forms a shocked atmosphere but accretes it through neutrino emission before it can become completely mixed. These kind of systems quickly collapse into black holes (for our specific case, the time scale for collapse $\sim 1 \text{ minute}$). Hence, the

current range of scenarios cited in the literature as possible birth mechanisms for $\dot{T}\dot{Z}$ objects will *not* form $\dot{T}\dot{Z}$ objects.

Even assuming that a proper formation scenario can be found, it is difficult to imagine how a $\dot{T}\dot{Z}$ object could exist for an extended period of time. Peculiarities in the structure of $\dot{T}\dot{Z}O$ seem to inevitably lead to instabilities which destroy the object. All stellar structure models of $\dot{T}\dot{Z}O$ have to smoothly connect the base of the envelope to the surface of the neutron star. In order to prevent significant neutrino emission, the base of the atmosphere must remain relatively cool ($\lesssim 10^9 K$). Eich et al. (1989) were able to construct such cool inner regions (which they call insulating layers) with low neutrino emission while maintaining the appropriate pressures. They argued that high-temperature atmospheres would emit neutrinos and turn into the low-temperature stable atmospheres that they had created. Our results clearly show that this is not the case and that once it begins, neutrino emission increases to a high value which maintains a high rate of accretion. In our simulations, after an initial transient, the neutrino emission rate becomes nearly constant (see Fig. 2.12) rather than shutting itself off after cooling the material at the surface of the neutron star.

This can readily be explained by the fact that energy losses due to neutrinos deleptonize and decrease the specific internal energy of the base of the atmosphere. Since the pressure is set by the structure above, the base of the atmosphere can only adjust and try to maintain pressure equilibrium by compression. This increases density *and temperature* (or if degeneracy has set in, the Fermi energy increases) and thus keeps up the neutrino emission rate until the material is incorporated into the neutron star. It may appear paradoxical that a loss of energy via neutrino emission could increase the temperature (or the Fermi energy). However, as a star

evolves, the entropy of the core continually decreases, while the central temperature keeps increasing [see also eq. (38)]. All this is related to the fact that under certain conditions, the heat capacity of gravitational systems can be negative (inasmuch as a gravitational system can be considered a thermodynamical system). As a result, once neutrino emission begins to have a dynamical effect, i.e. the compression of the base of the atmosphere, it will continue to be important. Thus the low temperature atmospheres constructed by Eich et al. (1989) are unstable.

In addition, the region above the inner layer postulated by Eich et al. (1989), has to have a high entropy $S > 600 k_B/\text{nucleon}$, so that neutrino losses remain unimportant (Fig. 2.16). Notwithstanding the fact that such entropies are an order of magnitude greater than those found in main sequence or even giant stars, a gravitationally bound atmosphere with $S > 600$ would have little mass (recall Fig. 2.7). Biehle (1991, 1994), Cannon et al. (1992), and Cannon (1993) have attempted to overcome this mass problem by placing a low-entropy envelope on top of the high-entropy inner region, with associated large negative entropy gradients (see Fig. 2.16). These atmospheres are, of course, unstable and Biehle and Cannon use the convective instability to transport energy outward and bring fuel down into the burning region of their stellar models. However, they treat convection with the mixing-length approximation. While Biehle and Cannon were able to maintain the structure of their atmospheres by assuming mixing length convection, we have found that this assumption is invalid by running two-dimensional calculations. Figure 2.17 illustrates the vigorous convection arising from Biehle's initial structure after 0.1 s. This convection eventually drives a shock through the atmosphere, disrupting it, and blowing it away.

An intrinsic assumption of mixing length theory is that the convective

evolution is nearly adiabatic, and slow compared to the dynamical timescale so that the evolution can be represented by a series of quasi-static equilibria. As a result, a necessary (but probably not sufficient) criterion for the validity of mixing length is that the sound travel time across a convective cell is much less than the rise time for that cell to move one cell length, or equivalently that the convective velocity is very subsonic. The mathematical details of this criterion are discussed in the appendix. Table 2.6 lists the rise times and velocities calculated with equations (47) and (48) for the convective cells after they travel one scale height for a typical supernovae simulation, the Sun, and the TŻ models of Biehle and Cannon. Note that only for the Sun is the ratio of the rise time over the sound crossing time *much* less than one. Of our four examples, only the Sun satisfies this essential assumption of mixing length theory.

We have argued above that currently envisioned astrophysical scenarios are incapable of forming TŻ objects. It also appears that present models of TŻ structures improperly account for convection using mixing-length algorithm, and thus result in unphysical objects which are artificially stable.

2.5.2. Common Envelope Systems

For a common envelope system, comparison to our results is less straightforward. Let us again discuss the characteristics of a specific case from Table 2.1. For a neutron star 10^{12} cm from the center of a $20M_{\odot}$ giant, moving at $v \approx v_{\text{orb}} = 100$ km s $^{-1}$, the infall rate is $175 M_{\odot} \text{ y}^{-1}$. Again, photons are trapped out to the Bondi radius and magnetic fields $\lesssim 4 \times 10^{13}$ Gauss will be smothered by the infalling material. Angular momentum induces a significant delay time in the accretion of order 200 s which is nevertheless much less than the orbital timescale. As we shall see, this situation leads to a neutrino induced explosion.

The convection timescale for this particular case is much less than the neutrino cooling timescale (see Table 2.4). This corresponds to the medium-low infall rate regime from our results. In this regime, the postshock entropy of the infalling material is critical to determine the outcome. From Figure 2.4, it is clear the accretion shock will lie at a radius $> 10^8$ cm, and using equation (29) the postshock entropy will be $\lesssim 50 k_B/\text{nucleon}$, if the shock is strong, which it is not since this value is close to the specific entropy of the material outside the Bondi radius. Nevertheless, this allows us to estimate that the entropy of the equilibrium atmosphere which forms above the neutron star corresponds to $29 < S < 50$ where the upper limit comes from the maximum post accretion shock entropy and the minimum comes from the entropy of the ambient matter.

From our models of equilibrium atmospheres (see §2.4.2), we know that these conditions will lead to explosions. These explosions may be sufficient to blow off the atmosphere and halt the inward spiral of the neutron star, forming close binary systems such as PSR 1913+16 (see Smarr & Blandford 1976 or Burrows & Woosley 1986). However, if the injected energy is insufficient to completely expel the atmosphere, the neutron star continues to fall into the giant star, as a new atmosphere once again builds up around it. Extrapolating from Table 2.4, we estimate that the neutron star might survive 50 outbursts over 100 years before it accretes $\sim 0.2 M_\odot$. Simulations of double core evolution (Terman, Taam, & Hernquist 1994) estimate inspiral times $\lesssim 1$ year with some cases where the energy input from viscous forces on the neutron star ($\sim 10^{47}$ ergs) is sufficient to drive off the envelope and halt the inward spiral of the neutron star. The neutron star will certainly survive this evolution, and this offers yet another way to form close binary systems.

However, we must here qualify our claims. As we have said before, it is not possible to run a continuous simulation from the convective infall regime to the stable equilibrium atmosphere which eventually appears. Thus, we are forced to infer indirectly the entropy of this equilibrium atmosphere from the early behavior observed in our infall simulations. Should the entropy for some reason end up larger than 50, then an explosion will not occur, but rather, the atmosphere will undergo steady, hypercritical accretion until the neutron star collapses to form a black hole.

2.5.3. Supernovae

At present, the details surrounding the explosion mechanism for supernovae are not sufficiently well understood to place any firm constraints on the fallback of matter onto the neutron star after a successful explosion (e.g. see Herant et al. 1994). Taking into account these uncertainties we would still like to address the questions whether fallback can lead to the formation of a black hole or a secondary explosion. A $25 M_{\odot}$ supernova progenitor exploded by Woosley & Weaver (1995) gives rise to an initial fallback rate of $10^7 M_{\odot} \text{ y}^{-1}$, decreasing thereafter. This initial value is just within the high accretion regime which corresponds to unrestricted accretion by the neutron star. This may or may not push the neutron star over its maximum mass, and make it collapse into a black hole. If this does not happen, the declining accretion rate will eventually reach the low infall regime which corresponds to explosions. Those would then blow off the remaining bound atmosphere. Note that the infall rate from this particular simulation was near the division between the high and low infall regimes, implying that uncertainties in the explosion mechanism coupled with differences between supernova progenitors may lead to very different outcomes, one in which a black hole forms, and another in which a secondary

explosions expels the remaining material bound to the neutron star.

2.5.4. Explosions

Explosions add an entirely new observational dimension to the the evolution of rapid mass infall systems which we have considered in this paper. Physically, these explosions are most akin to Type II supernovae, and thus, some of the observational aspects may be similar (velocities, compositions) even though the amount of mass expelled and energy should be a factor of 10^{-5} smaller. Moreover, it is clear that the extent and amount of material in which a neutron star is embedded during such an explosion will have a crucial impact on the observational signature. The range of possible signatures is vast, requiring a more detailed analysis which we relegate to future work. However, in some circumstances, these supernova-like objects may still be bright enough to be seen in nearby galaxies.

Using observed abundances of Be systems and Massive Binary systems, Biehle (1991) has derived the formation rate of common envelope systems to be between 2×10^{-5} and 6×10^{-4} per year in our galaxy. Using the entire set of observations of massive X-ray binaries, Cannon (1993) gave a not too different estimate of 10^{-3} objects per year in our galaxy. Iben, Tututov, & Yungelson (1995) predict 1.5×10^{-3} objects using an entire neutron star census. Because the “embedding” companion star will usually be massive, explosions in these systems are likely to be damped as they propagate through the massive envelope. They may therefore appear only as enhancements of an already strong wind, and changes in chemical abundances.

Focusing on globular clusters, Davies & Benz (1995), have obtained a reliable formation rate of 10^{-8} per year per cluster (which corresponds to $\sim 10^{-6}$ per

year per galaxy) through extensive encounter simulations. They also predict that these collisions generally result in a $\sim 0.3 M_{\odot}$ atmosphere remaining bound to the neutron star. Due to the smaller amount of mass surrounding the neutron star, explosions from these atmospheres will be less damped and might be observed as supernova-like objects. However, the low formation rates limit the observational prospects for these objects. One should note though, that these objects have been proposed as progenitors of millisecond pulsars. If, instead, they blow off their atmospheres before accreting sufficiently to be spun up, other scenarios for the production of millisecond pulsars will have to be found. Further study including angular momentum effects will better address this problem. Similarly, the dense stellar systems of galactic bulges offer opportunities for mergers involving neutron stars through collisions. However, we are not aware of reliable estimates for collisional rates in the galactic center.

Leonard et al. (1994) investigated the scenario in which the velocity kick received by a neutron star in a supernova explosion makes it merge with a binary companion. They predicted an occurrence rate of 2.5×10^{-4} per year in our galaxy. These systems may result in an inward spiralling neutron star. However, since the kick produces collisions with similar velocities to those from the globular cluster collisions of Davies & Benz, we might instead expect the likely result to be $\sim 0.3 M_{\odot}$ smothered neutron stars as predicted in their models. Assuming the latter to be the case, we would expect 1% of observed supernovae to produce a secondary explosion and lead to a peculiar structure of the remnant.

2.5.5. Future Work

We would like to follow-up the discovery of these “accretion induced” explosions with detailed calculations of their observable signatures. The observational

prospects for the ejection of neutron star atmospheres are tightly linked to the fraction of encounters which result in energetic explosions. This fraction is in turn strongly dependent on the effects of angular momentum. While at best difficult, accounting for those effects will be essential to understanding neutron stars accreting at high rates. We would also like to determine the observational properties and chemical composition of the ejected material. This will be addressed in future work.

Although it is an interesting topic, we have not discussed the case of neutron stars embedded in dense molecular clouds or in AGN disks elsewhere in this paper. Unfortunately, in these conditions, the photon trapping radius is within the Bondi radius so that radiation transport plays an important role in the evolution. It is plausible that dense molecular cloud will first accrete slowly, at the Eddington rate, until sufficiently high pressures and temperatures near the neutron star surface develop, leading then to hypercritical accretion or possibly an expulsion of the material. This ejecta will enrich the surrounding medium and, since the mass accretion will be low, may be a repeatable process, facilitating an important mechanism to enrich the interstellar medium or the disk of an AGN. Understanding these effects will require the implementation of a radiation transport scheme.

2.5.6. A Necessary Criterion for the Validity of the Mixing Length Approximation for Convection

Despite the many problems with mixing length (choice of scale height, etc.), there is no better convection algorithm short of multidimensional simulations. Hence, mixing length theory remains the most common technique for dealing with convective instabilities. It is thus worthwhile to try to derive a simple criterion to verify the validity of a mixing length approach in a given situation. An intrinsic

assumption of mixing length theory is that the convective evolution is nearly adiabatic, and slow compared to the dynamical timescale so that the evolution can be represented by a series of quasi-static equilibria. As a result, a necessary (but probably not sufficient) criterion for the validity of mixing length is that the sound travel time across a convective cell is *much* less than the rise time for that cell to move one cell length, or equivalently that the convective velocity is very subsonic. In the following paragraphs, we first provide a rigorous calculation of the motion of a convective cell which we then complement with a more physically intuitive interpretation. We go on to show that typical convective neutron star atmospheres do not satisfy our criterion and therefore cannot be modeled using mixing length.

The sound travel time across a cell is simply given by:

$$\tau_s = H_p / c_s \quad (43)$$

where H_p is the convective scale length, typically approximated as the pressure scale height and c_s is the sound speed of the convective cell. The acceleration for the cell is [see Hansen & Kawaler (1994) for a basic summary]:

$$a_{\text{cell}} = a_{\text{buo}} + a_{\text{vis}} = g(1 - \rho/\rho_c) - \frac{\eta}{\rho} \nabla^2 v - \frac{\theta_{\text{turb}}}{V\rho} \quad (44)$$

where g is the gravitational acceleration at the position of the cell, ρ_c is the density of the cell, ρ is the density of the medium through which the cell is passing and V is the volume of the cell. The quantity η is the linear viscous term and can be written (see Kippenhahn & Weigert 1990):

$$\eta \approx \eta_{\text{th}} + \eta_{\text{rad}} \approx \rho l_{\text{mfp}} v_{\text{th}} + aT^4 / c\kappa\rho \quad (45)$$

where l_{mfp} is the electron mean free path and v_{th} is the electron's thermal velocity. We shall approximate $\nabla^2 v = v / (fH_p)^2$ where $f < 1$ (in our calculations, we choose

$f = 0.01$). The term θ_{turb} is the turbulent drag [see, for example, Shames (1992)]:

$$\theta_{\text{turb}} \approx \frac{C_{\text{turb}} \rho v^2 A}{2} \quad (46)$$

where C_{turb} depends upon how streamlined our convective cells are (values range from 0.01–1 and we conservatively use 1) and A is the effective surface area of the cell.

We can then integrate this equation to determine the velocity of the cell (assuming it starts at rest) and distance as a function of time:

$$v = (L + M) \left(\frac{e^{2Lct} - 1}{\left(\frac{L+M}{L-M}\right) e^{2Lct} + 1} \right), \quad (47)$$

$$x = -\ln \left(\frac{\left(\frac{L+M}{L-M}\right) e^{2Lct} + 1}{c} \right) - (L + M)t + \ln \left(\frac{\left(\frac{L+M}{L-M}\right) + 1}{c} \right) \quad (48)$$

where $L = \sqrt{b^2/(4c^2) - a/c}$ and $M = b/2c$ with $a = a_{\text{buo}}$, $b = -\eta/(f\rho H_p^2)$, and $c = -(C_{\text{turb}}\rho A)/(2\rho_c)$. Setting $x = H_p$, one can solve for the rising time scale, and determine whether the evolution can be appropriately modeled with a mixing length algorithm.

In most circumstances, the dominant viscous force arises from the turbulent drag term. Ignoring the linear viscous terms simplifies the preceding equations and provides a more intuitive picture of the conditions required for using the mixing length formalism (although we recommend the general argument for any applications). As we stated earlier, a necessary condition for mixing length is that the sound travel time is much less than the convective travel time, or equivalently, the convective velocity must be much slower than the sound speed. By eliminating the linear term from equation (44), using equation (46) with $A/V = 1/H_p$, and setting $g = \nabla P/\rho = P/(\rho H_p)$, we can solve for the maximum bubble velocity:

$$v_{\text{max}} = \sqrt{\frac{2P}{\rho C_{\text{turb}}}} (\rho/\rho_c - 1) = c_s \sqrt{\frac{2}{C_{\text{turb}} \gamma}} (\rho/\rho_c - 1). \quad (49)$$

For a $\gamma = 4/3$ gas and $\rho_c < .85\rho$, we find that $v_{\max} > .5c_s$, violating the mixing length assumption that $v \ll c_s$. However, these high velocities are only a problem if the bubble can attain them before dispersing. We can estimate the velocity of the bubble after travelling a distance d by assuming that the turbulent viscosity is small until v approaches v_{\max} :

$$v = \sqrt{2da} = c_s \sqrt{\frac{d}{H_p} \frac{2}{C_{\text{turb}} \gamma} (\rho/\rho_c - 1)}. \quad (50)$$

Setting $d = H_p$ gives $v \rightarrow v_{\max}$. It is likely, then, that the bubble will approach its maximum velocity after rising one scale length. The ratio of the bubble density to the density of the ambient medium is clearly the primary parameter behind this necessary criterion for mixing length and can be simply applied to any system. One merely needs to determine the buoyancy (or density) of a bubble raised adiabatically one scale height.

TABLE 1
ACCRETION PARAMETERS

Stellar Type ^a	Velocity km s ⁻¹	c _s km s ⁻¹	Bondi Radius 10 ¹¹ cm	\dot{M} M _⊙ y ⁻¹	Inhom. Factor $\epsilon_{p,v}$	R _{ang} 10 ⁸ cm	Trap. Rad. 10 ¹¹ cm	Result ^b
1 M _⊙ MS								
@ 4 × 10 ¹⁰ cm	1000	300	.17	N/A	N/A	N/A	N/A	IC
ρ = .4g/cm ³	300	300	1	N/A	N/A	N/A	N/A	IC
S = 15k _B /nucleon	100	300	2	N/A	N/A	N/A	N/A	IC
@ 1.25 × 10 ¹⁰ cm	1000	475	.15	N/A	N/A	N/A	N/A	IC
ρ = 60g/cm ³	300	475	.6	N/A	N/A	N/A	N/A	IC
S = 12k _B /nucleon	100	475	.8	N/A	N/A	N/A	N/A	IC
5 M _⊙ MS								
@ 10 ¹¹ cm	1000	400	.16	1.4 × 10 ³	.72,-.07	.77	.16	IC
ρ = .25g/cm ³	300	400	.75	1.4 × 10 ⁴	3.4,-.004	200	.75	IC
S = 17k _B /nucleon	100	400	1.0	2.0 × 10 ⁴	4.5,~0	68	1.0	IC
@ 4 × 10 ¹⁰ cm	1000	550	.14	2.7 × 10 ⁴	.56,-.17	1.3	.14	IC
ρ = 6.3g/cm ³	300	550	.5	2.0 × 10 ⁵	2.0,-.20	4.8	.5	IC
S = 15k _B /nucleon	100	550	.6	2.5 × 10 ⁵	2.4,-.20	1.2	.6	IC
10 M _⊙ MS								
@ 2 × 10 ¹¹ cm	1000	350	.17	1.5 × 10 ³	.4,-.03	.47	.17	IC
ρ = .25g/cm ³	300	350	.9	1.8 × 10 ⁴	2.0,-.16	26	.9	IC
S = 18k _B /nucleon	100	350	1.4	3.5 × 10 ⁴	3.2,-.10	44	1.4	IC
@ 6 × 10 ¹⁰ cm	1000	600	.14	1.0 × 10 ⁴	.35,-.03	.19	.14	IC
ρ = 2.5g/cm ³	300	600	.4	5.0 × 10 ⁴	1.0,-.05	2.4	.4	IC
S = 17k _B /nucleon	100	600	.5	7.5 × 10 ⁴	1.25,-.06	4.5	.5	IC
20 M _⊙ MS								
@ 1 × 10 ¹² cm	1000	200	.18	20	.14,.01	.43	.18	EX
ρ = 3 × 10 ⁻³ g/cm ³	300	200	1.4	300	1.0,.07	120	1.4	EX
S = 22k _B /nucleon	100	200	4.0	2000	3.0,.11	720	4.0	IC
@ 5 × 10 ¹¹ cm	1000	300	.17	75	.034,-.01	7 × 10 ⁻³	.17	EX
ρ = 1.3 × 10 ⁻² g/cm ³	300	300	.74	570	.3,-.01	.10	.74	EX
S = 21k _B /nucleon	100	300	1.3	1300	.52,-.03	.06	1.3	IC
10 M _⊙ Giant								
@ 2.5 × 10 ¹³ cm	1000	40	.2	4 × 10 ⁻⁴	.0024,~0	8 × 10 ⁻⁵	.14	DC
ρ = 5 × 10 ⁻³ g/cm ³	300	40	2.0	.01	.024,~0	.07	2.0	DC
S = 26k _B /nucleon	70	40	30	.7	.36,-.01	130	30	EX
@ 6 × 10 ¹² cm	1000	60	.2	2.5 × 10 ⁻³	.005,~0	3 × 10 ⁻⁴	.2	DC
ρ = 3 × 10 ⁻⁷ g/cm ³	300	60	2.0	.06	.05,-.01	.01	2.0	EX
S = 26k _B /nucleon	70	60	20	2	.5,-.05	26	20	EX
@ 1 × 10 ¹¹ cm	1000	300	.17	480	.13,-.06	5 × 10 ⁻³	.17	EX
ρ = 8 × 10 ⁻² g/cm ³	300	300	.74	3700	.58,-.15	1.7	.74	IC
S = 10k _B /nucleon	70	300	2.0	2 × 10 ⁴	1.6,-.37	2.5	2.0	IC
20 M _⊙ Giant								
@ 1 × 10 ¹² cm	1000	250	.18	7	.06,.01	.15	.18	EX
ρ = 10 ⁻³ g/cm ³	300	250	1.2	100	.42,.07	31	1.2	EX
S = 29k _B /nucleon	100	250	1.8	175	.63,.12	20	1.8	EX
@ 4 × 10 ¹¹ cm	1000	400	.11	25	.06,~0	.01	.11	EX

TABLE 1—Continued

Stellar Type ^a	Velocity km s ⁻¹	c _s km s ⁻¹	Bondi Radius 10 ¹¹ cm	M M _⊙ y ⁻¹	Inhom. Factor $\epsilon_{\rho,v}$	R _{ang} 10 ⁸ cm	Trap. Rad. 10 ¹¹ cm	Result ^b
$\rho = 10^{-2} \text{g/cm}^3$	300	400	.5	250	.25,-.06	.09	.5	EX
$S = 24k_B/\text{nucleon}$	100	400	1.0	800	.5,-.1	.01	1.0	EX
@ $5 \times 10^{10} \text{cm}$	1000	1000	.094	6.0×10^5	.11,-.04	.36	.094	IC
$\rho = 250 \text{g/cm}^3$	300	1000	.17	1.5×10^6	.20,-.06	.02	.17	IC
$S = 10k_B/\text{nucleon}$	100	1000	.18	1.8×10^6	.21,-.07	5×10^{-3}	.18	IC
GMC								
	1000	10	.2	8×10^{-8}	0?	0?	3×10^{-5}	?
$\rho = 10^{-11} \text{g/cm}^3$	300	10	2.0	2×10^{-6}	0?	0?	7×10^{-4}	?
$S = 45k_B/\text{nucleon}$	10	10	930	.024	0?	0?	9	?

^aUnderneath each stellar type, we also list the position in the star that we are considering as well as the density and entropy at that position.

^bIC = Immediate Collapse, EX = Explosion, DC=Delayed Collapse

^aUnderneath each stellar type, we also list the position in the star that we are considering as well as the density and entropy at that position.

^bIC = Immediate Collapse, EX = Explosion, DC=Delayed Collapse

Table 2.2. Infall Atmospheres

Infall Rate $M_{\odot} \text{ y}^{-1}$	L_{ν}^{tot} (erg s $^{-1}$)	1-D τ_{conv} (s)	Results γ	S_{center}
$S_{\text{infall}} = 30$ $M_{\text{crit}} = \sim 10^6$				
10^0	$< 10^{39}$	$\sim .02$	1.35	630
10^1	$\sim 3 \times 10^{41}$	$\sim .06$	1.37	380
10^2	$\sim 7 \times 10^{43}$	$\sim .05$	1.4	220
10^3	$\sim 6 \times 10^{46}$	$\sim .03$	1.4	120
10^4	$\sim 2.5 \times 10^{48}$	$\sim .03$	1.4	85
10^5	$\sim 1 \times 10^{50}$	$\sim .03$	1.43	~ 50
$S_{\text{infall}} = 10$ $M_{\text{crit}} = \sim 5 \times 10^5$				
10^0	$< 10^{39}$	$\sim .02$	1.35	650
10^2	$\sim 9 \times 10^{43}$	$\sim .03$	1.4	200
10^5	$\sim 3 \times 10^{50}$	$\sim .03$	1.4	~ 40
10^6	$\sim 7 \times 10^{51}$	$\sim .02$	1.43	~ 25
$S_{\text{infall}} = 50$ $M_{\text{crit}} = \sim 2 \times 10^6$				
10^1	$\sim 2 \times 10^{41}$	$\sim .02$	1.37	650
10^3	$\sim 2 \times 10^{46}$	$\sim .03$	1.4	130

Table 2.3. Infall Atmospheres

Infall Rate $M_{\odot} \text{ y}^{-1}$	L_{ν}^{tot} (erg s $^{-1}$)	KE_{exp} (erg)	2-D $\tau_{\text{BH}}(s)$	Results $\tau_{\text{conv}}(s)$	S (k_B/nuc)	$M_{\text{exp}}(M_{\odot})$
$S_{\text{infall}} = 30$						
10^1	$\sim 4 \times 10^{41}$	$\sim 3 \times 10^{43}$	$\sim 10^{11}$	$10^4 - 10^6$	50 - 100	10^{-7}
10^3	$\sim 8 \times 10^{45}$	$\sim 2 \times 10^{45}$	$\sim 10^7$	$\sim 10^6$	$\sim S_{\text{infall}}$.1
10^5	$\sim 7 \times 10^{49}$	$\sim 2 \times 10^{47}$	$\sim 10^3$	$\sim 10^5$	$\sim S_{\text{infall}}$	100

Table 2.4. Constant Entropy Atmospheres

S_{tot}	Results
10	Immediate explosion
20	Immediate explosion
30	$\tau_{\text{conv}} \approx 5 \text{ ms}$ $t_{\text{infall}} = .05 \text{ s}$ $KE_{\text{exp}} = 2 \times 10^{46} \text{ erg}$
50	$\tau_{\text{conv}} \approx .1 \text{ s}$ $t_{\text{infall}} = 2 \text{ s}$ $KE_{\text{exp}} = 2 \times 10^{45} \text{ erg}$ $\dot{M} \approx 3 \times 10^3 M_{\odot} \text{ y}^{-1}$ $L_{\nu}^{\text{tot}} \approx 3 \times 10^{49} \text{ erg s}^{-1}$
60	$\dot{M} = 3.8 \times 10^3 (\pm 300) M_{\odot} \text{ y}^{-1}$ $L_{\nu}^{\text{tot}} \approx 4 \times 10^{49} \text{ erg s}^{-1}$
70	$\dot{M} = 5.2 \times 10^2 (\pm 50) M_{\odot} \text{ y}^{-1}$ $L_{\nu}^{\text{tot}} \approx 5 \times 10^{48} \text{ erg s}^{-1}$
80	$\dot{M} = 1.8 \times 10^2 (\pm 20) M_{\odot} \text{ y}^{-1}$ $L_{\nu}^{\text{tot}} \approx 2 \times 10^{48} \text{ erg s}^{-1}$
90	$\dot{M} = 33 (\pm 6) M_{\odot} \text{ y}^{-1}$ $L_{\nu}^{\text{tot}} \approx 5 \times 10^{47} \text{ erg s}^{-1}$
100	$\dot{M} = 13 (\pm 3) M_{\odot} \text{ y}^{-1}$ $L_{\nu}^{\text{tot}} \approx 2 \times 10^{47} \text{ erg s}^{-1}$

Table 2.5. Infall Results

Infall Rate	Transient Convection	Neutrino Convection	End Result
$\dot{M} > 10^6 M_{\odot} \text{ y}^{-1}$	No	No	Black Hole
$10^6 M_{\odot} \text{ y}^{-1} > \dot{M} > 10^3 M_{\odot} \text{ y}^{-1}$	No ^a	No	Black Hole
$10^3 M_{\odot} \text{ y}^{-1} > \dot{M} > 0.01 M_{\odot} \text{ y}^{-1}$	Yes	Yes	Explosion
$0.01 M_{\odot} \text{ y}^{-1} > \dot{M} > 10^{-4} M_{\odot} \text{ y}^{-1}$	Yes	No	Steady Accretion

^aA transient is produced but a black hole forms before it can fully develop.

Table 2.6. Convection

ratio	Solar Envelope	Core Collapse	Model	
		Supernova	Biehle's TŻ	Cannon's TŻ
$t_{\text{co}}/t_{\text{cs}}$	$\sim 2 \times 10^3$	~ 1.2	~ 4	~ 2
v/c_s	$\sim 4 \times 10^{-3}$	~ 1.0	$\sim .2$	$\sim .5$

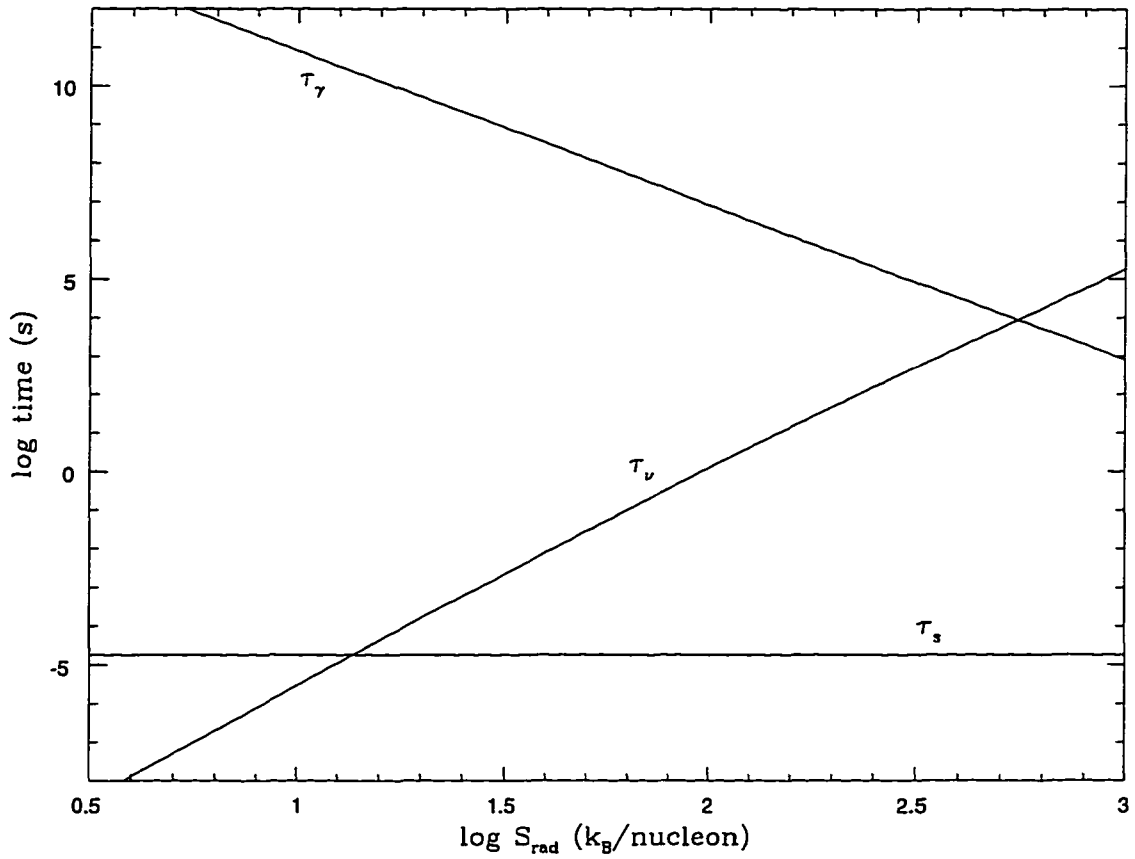


Figure 2.1 characteristic timescales; photon diffusion τ_γ , neutrino cooling τ_ν , and sound travel time τ_s versus entropy. Note that at an entropy lower than that defined by the intersection between the sound travel and neutrino cooling timescale, no stable atmosphere can form. Note also that the intersection between photon diffusion and neutrino cooling defines the entropy at which photon trapping is complete.

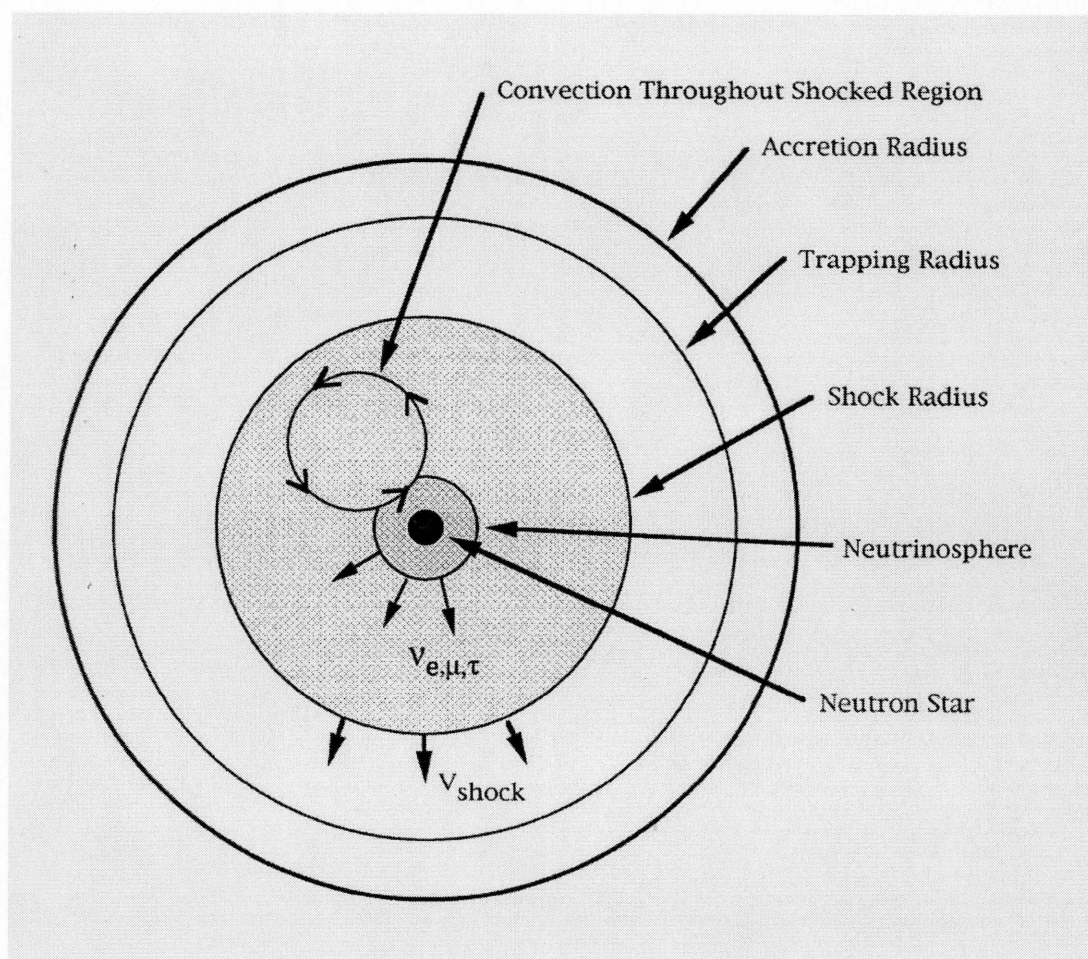


Figure 2.2 structure of an infall atmosphere. Note that the region within the accretion shock is convectively unstable.

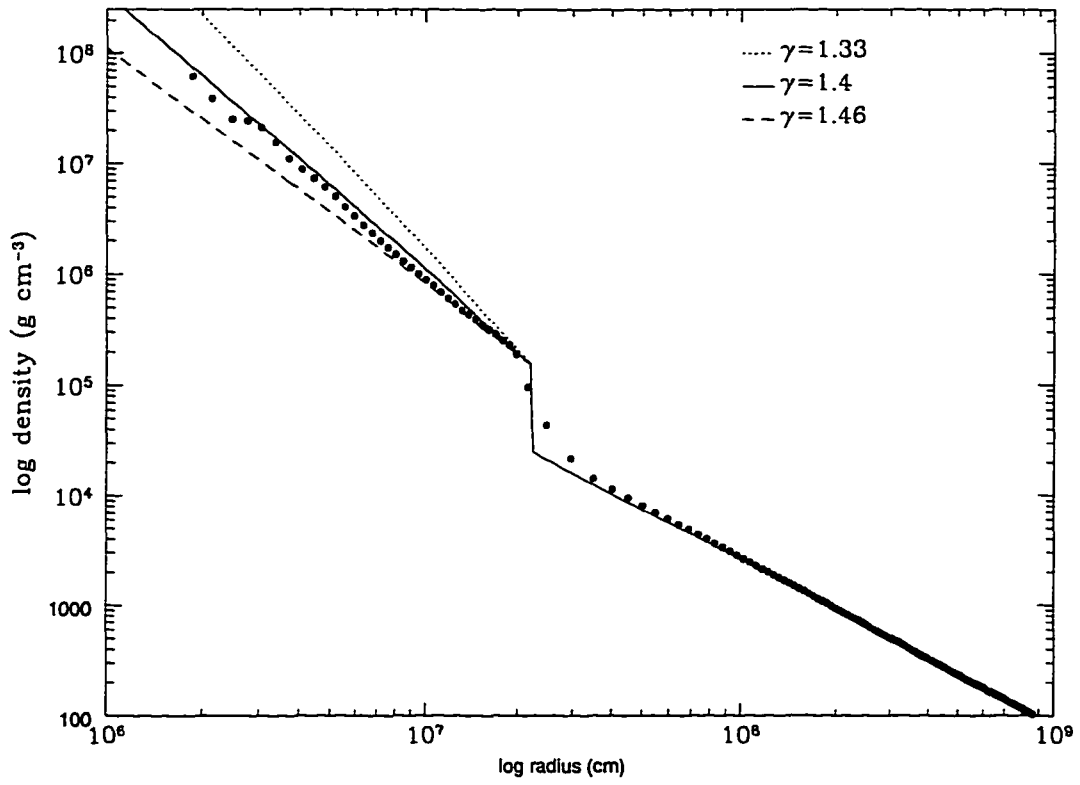


Figure 2.3 Density vs. radius for a $10^3 M_{\odot} \text{ y}^{-1}$ infall model. The points are from numerical simulations. The lines are analytical results for different adiabatic indices.

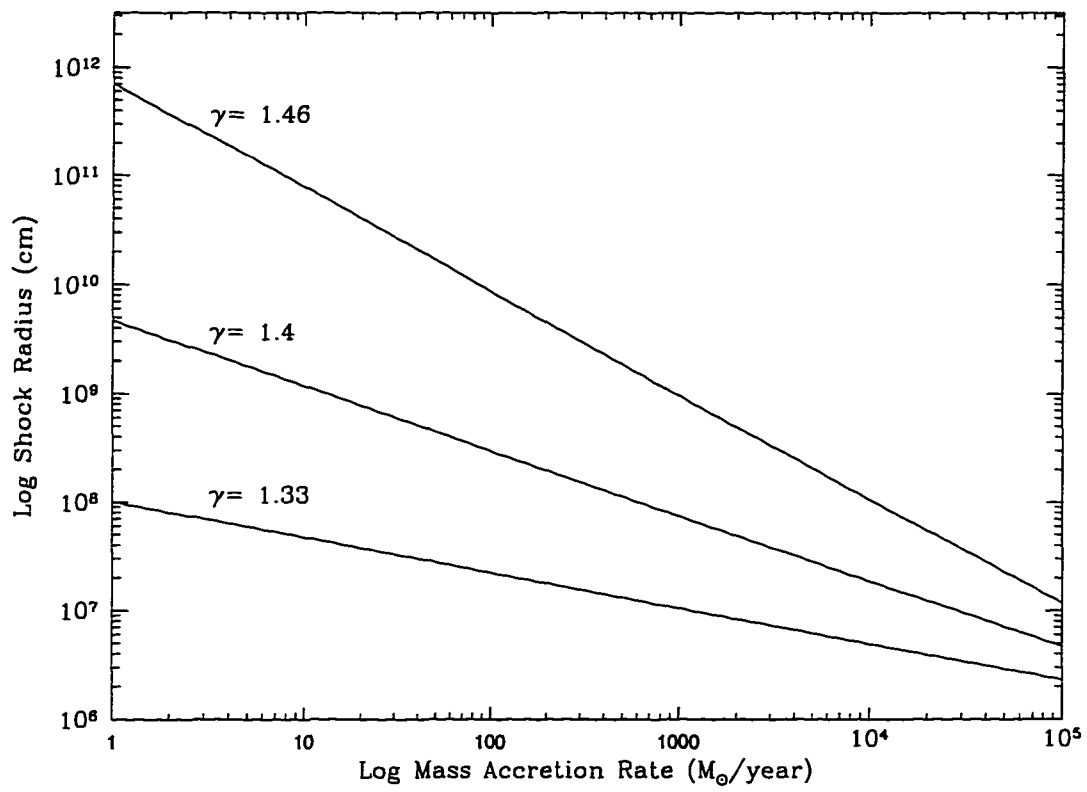


Figure 2.4 steady state shock radius versus accretion rate for a range of adiabatic indices in a one-dimensional infall model.

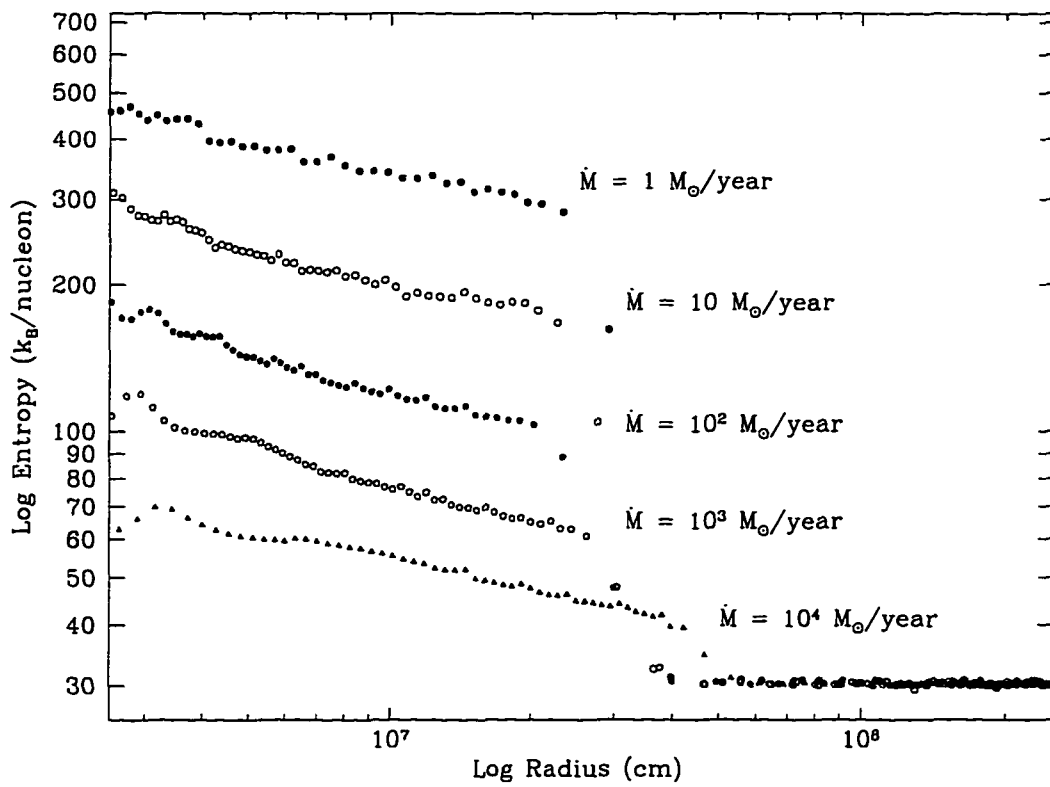


Figure 2.5 Entropy versus radius after 50 ms for a range of infall atmospheres.

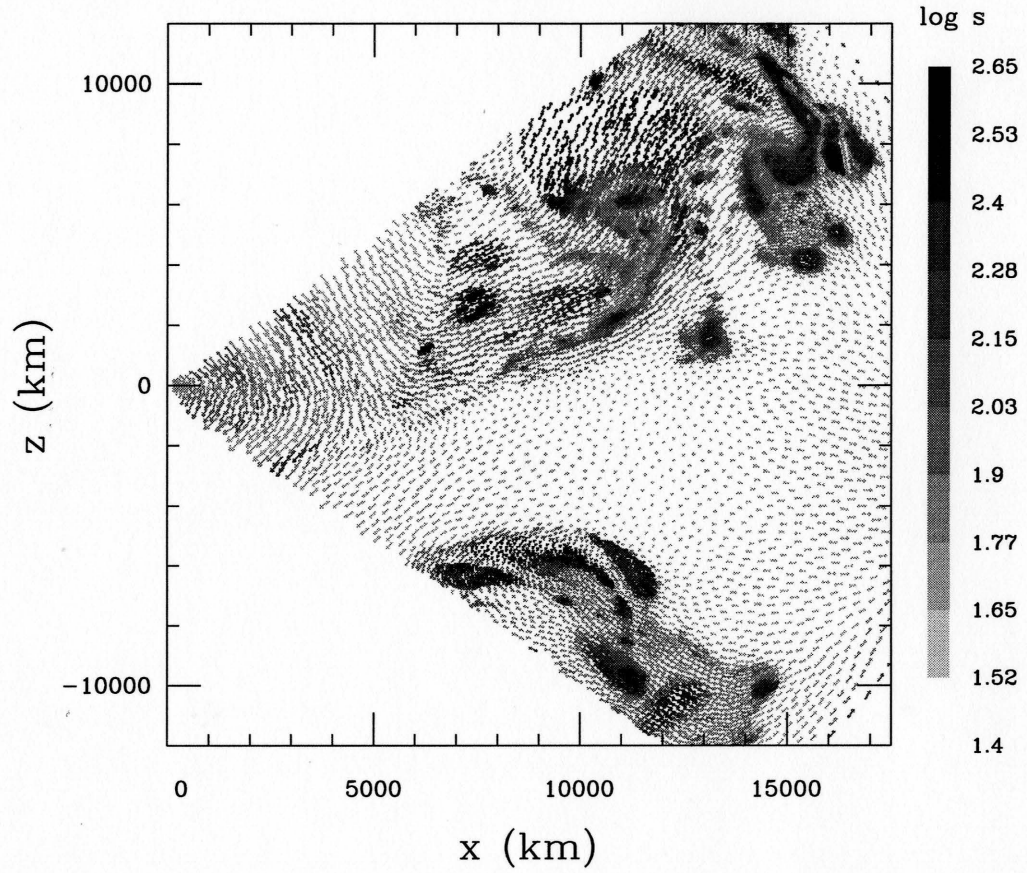


Figure 2.6 entropy-driven convective plume for $10^3 M_{\odot} \text{ y}^{-1}$ infall atmosphere 10 s after creation of the accretion shock. The negative entropy gradient is induced by the initial outward motion of the shock. Average plume velocity is 3000 km/s and mean inflow velocity is 1000 km/s.

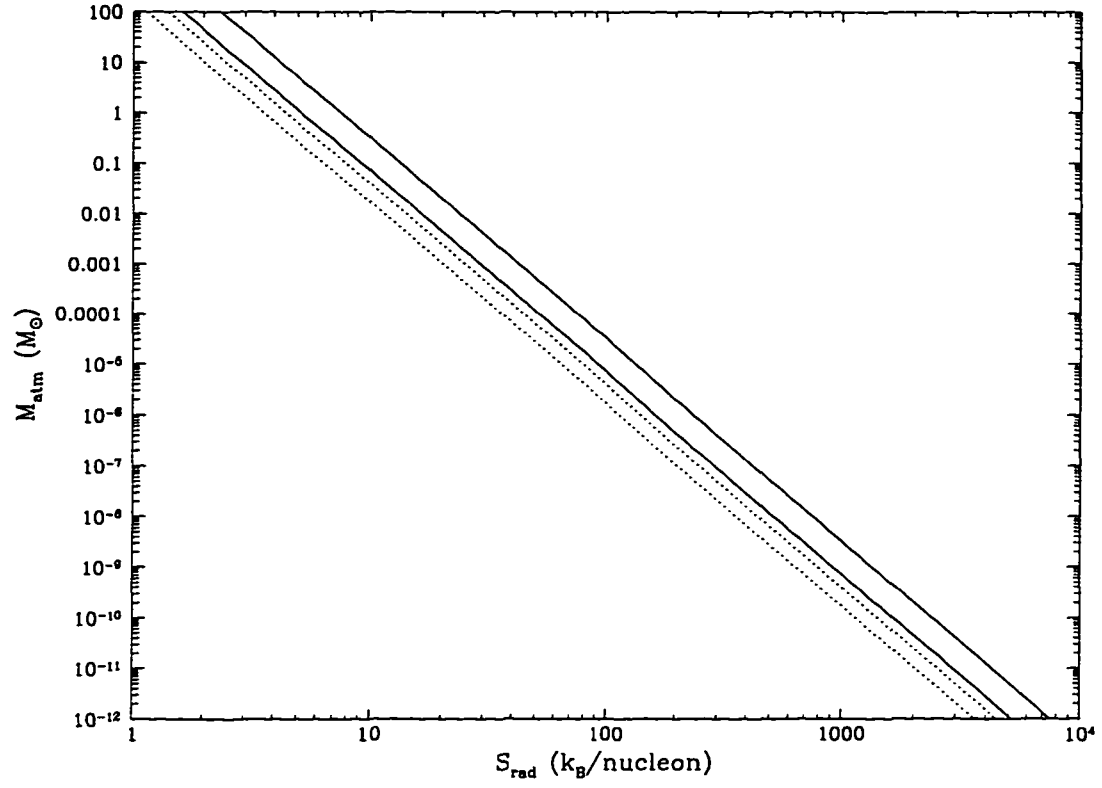


Figure 2.7 atmosphere mass versus entropy for two sizes of atmosphere: $R = 10^9$ cm and 10^{13} cm. The dashed lines denote atmospheres with no external pressure, whereas the solid lines include a pressure term derived from typical values for Bondi-Hoyle accretion.

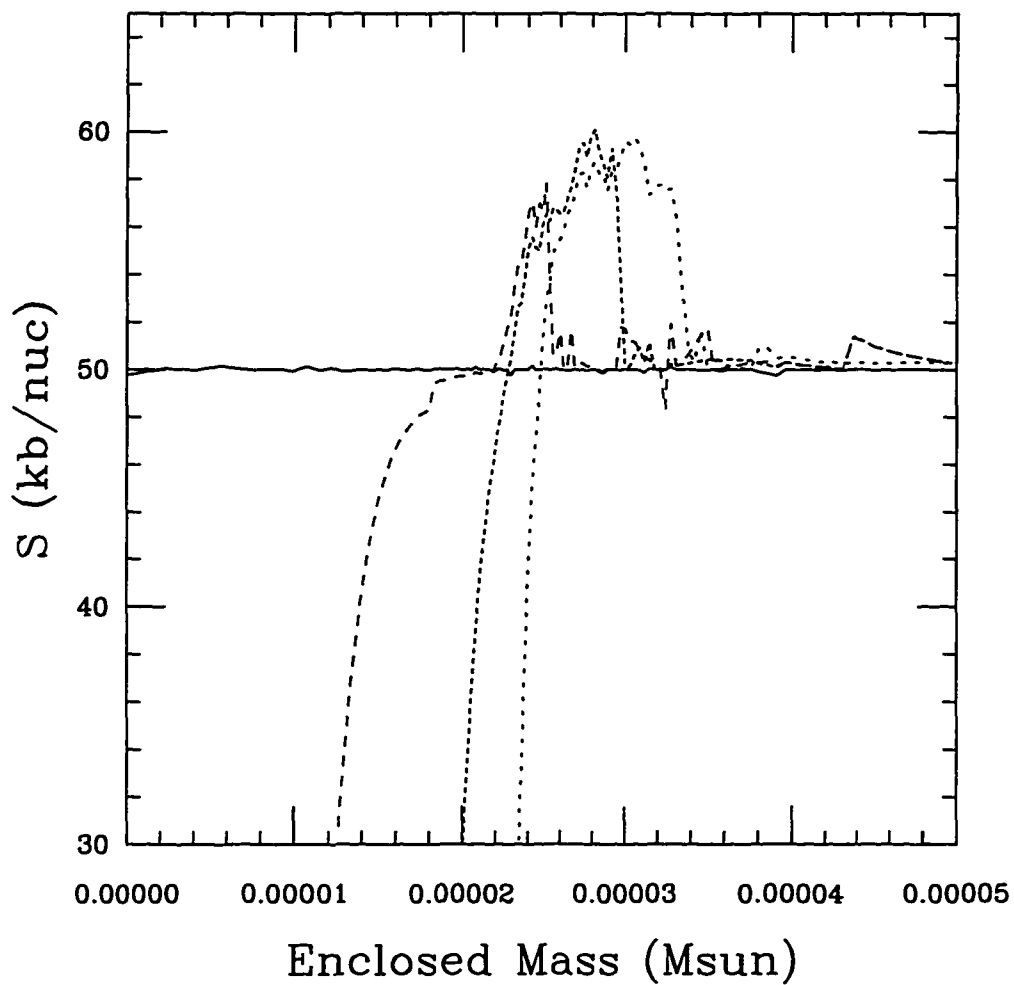


Figure 2.8 entropy profiles at 70 ms intervals for an $S_{\text{tot}} = 50$ equilibrium atmosphere. Note that with increasing time, the innermost material cools (lowering its entropy) while an increasing amount of material is heated (raising its entropy).

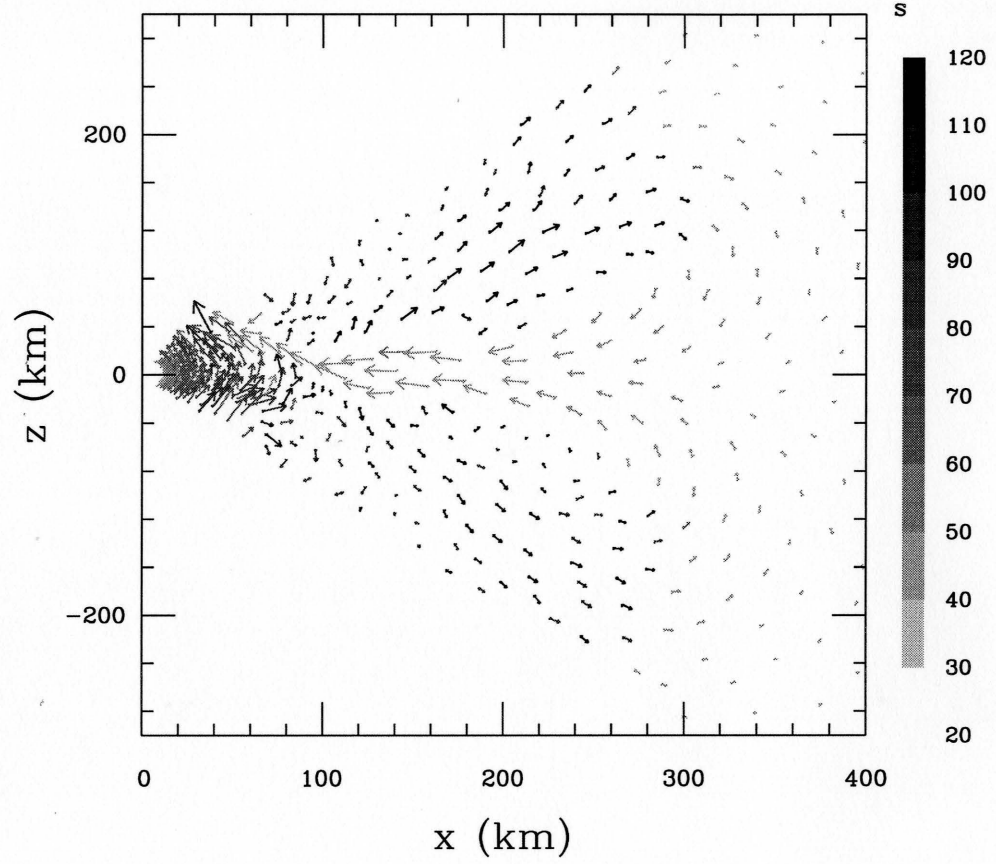


Figure 2.9 entropy-driven convection for an $S_{\text{tot}} = 50$ equilibrium atmosphere 200 ms after turning on neutrino processes. The negative entropy gradient is induced by neutrino heating and drives convection. The mean outflow velocity is 4000 km/s and the mean inflow is 9000 km/s.

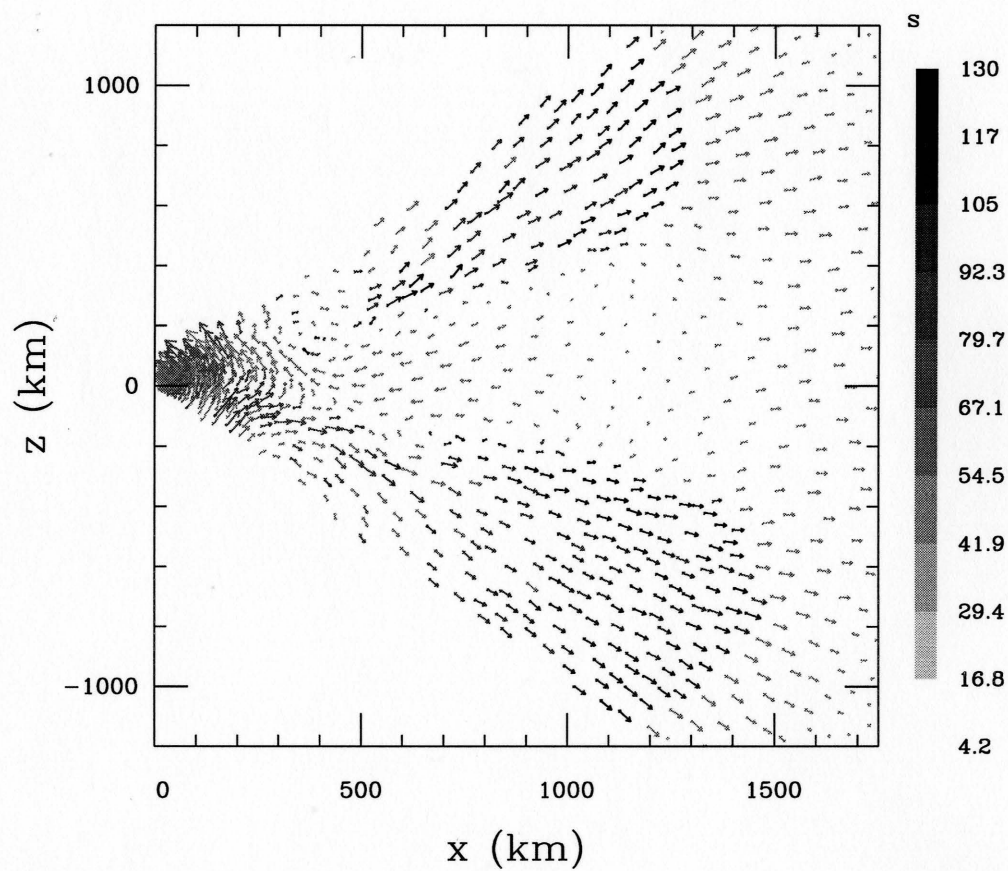


Figure 2.10 the same simulation from Figure 4 after 500 ms. The atmosphere is now exploding with a kinetic energy of 2×10^{-6} foe. The mean outflow velocity is 5000 km/s and the mean inflow is 3000 km/s.

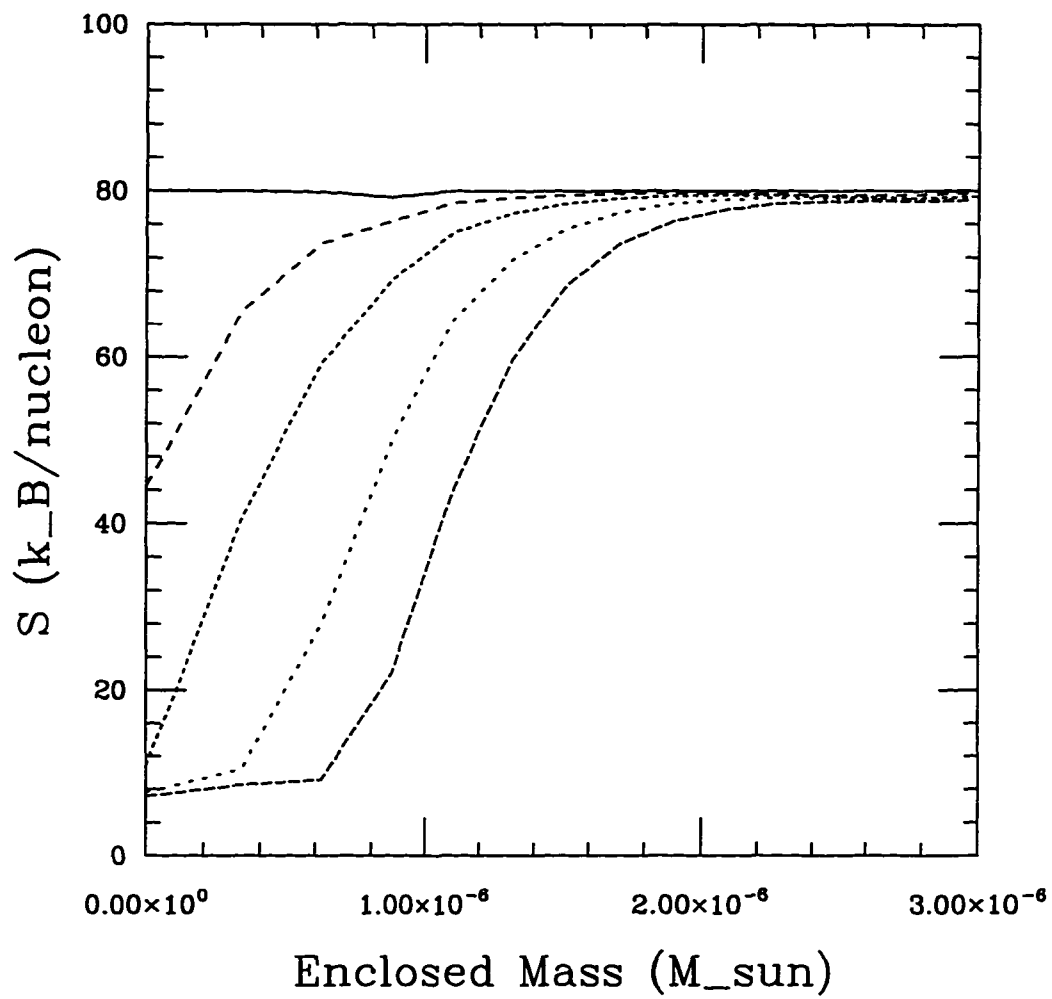


Figure 2.11 entropy vs. mass at 80 ms intervals for an $S_{\text{tot}} = 80$ equilibrium atmosphere. Note that the inner material radiates its energy through neutrino losses, lowering its entropy.

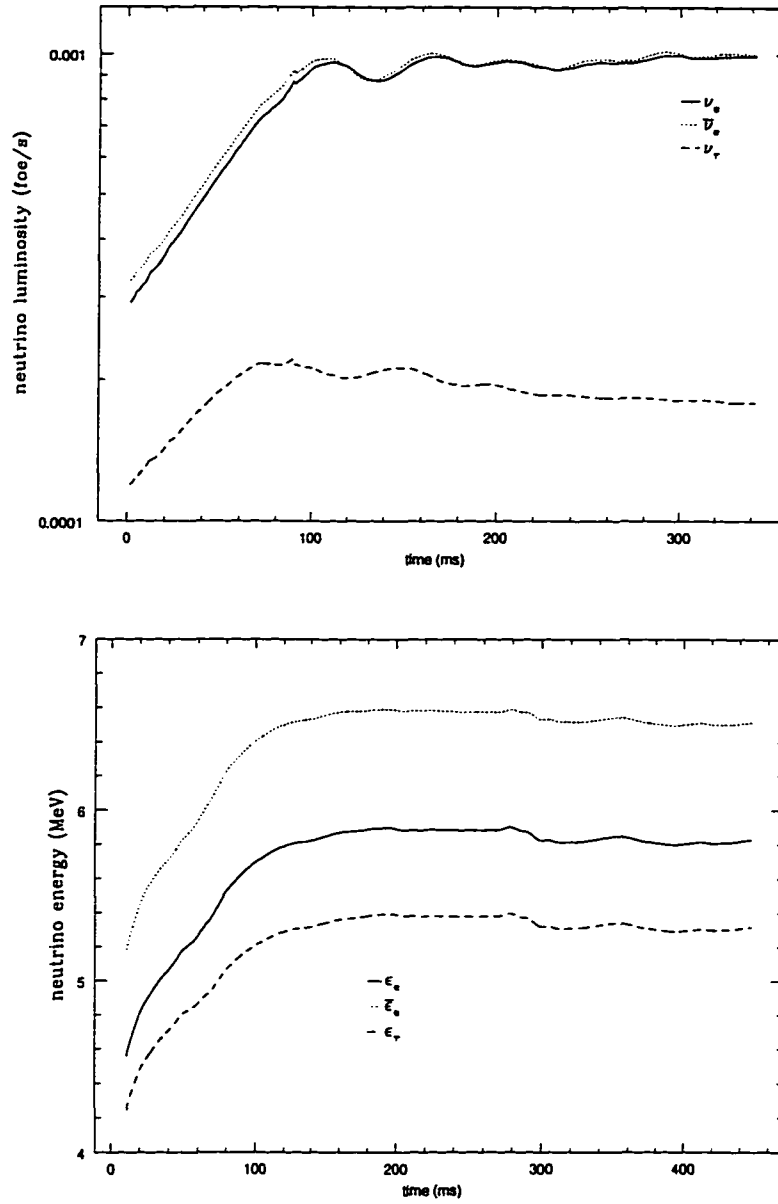


Figure 2.12 Neutrino luminosity and mean neutrino energy as a function of time for an $S_{\text{tot}} = 80$ equilibrium atmosphere.

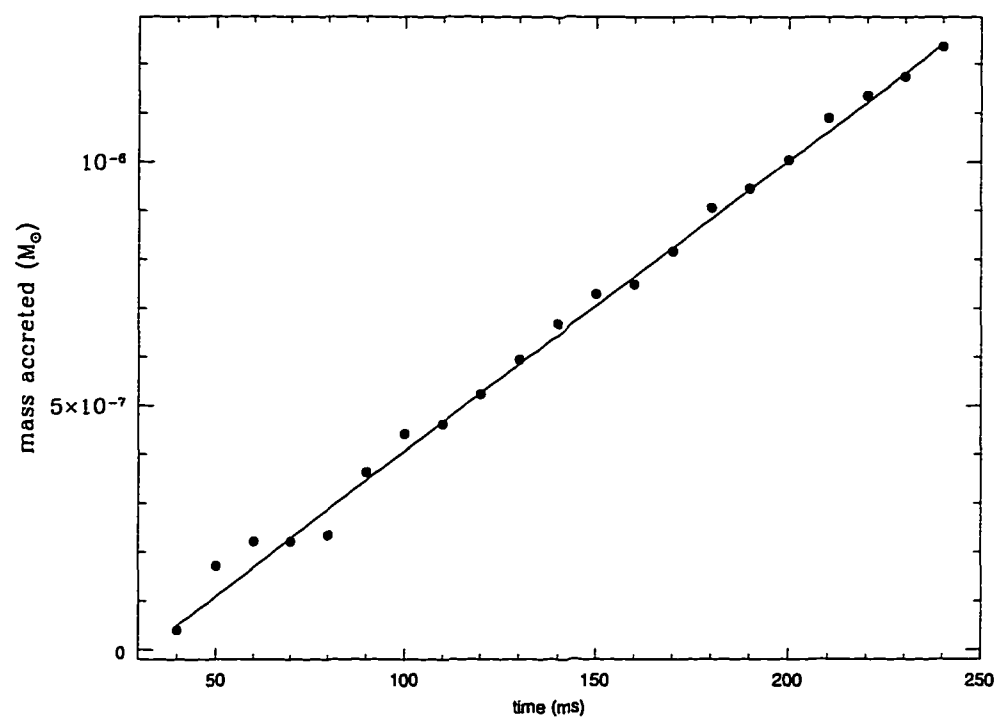


Figure 2.13 total mass accreted versus time with the best constant accretion fit for an $S_{\text{tot}} = 80$ equilibrium atmosphere.

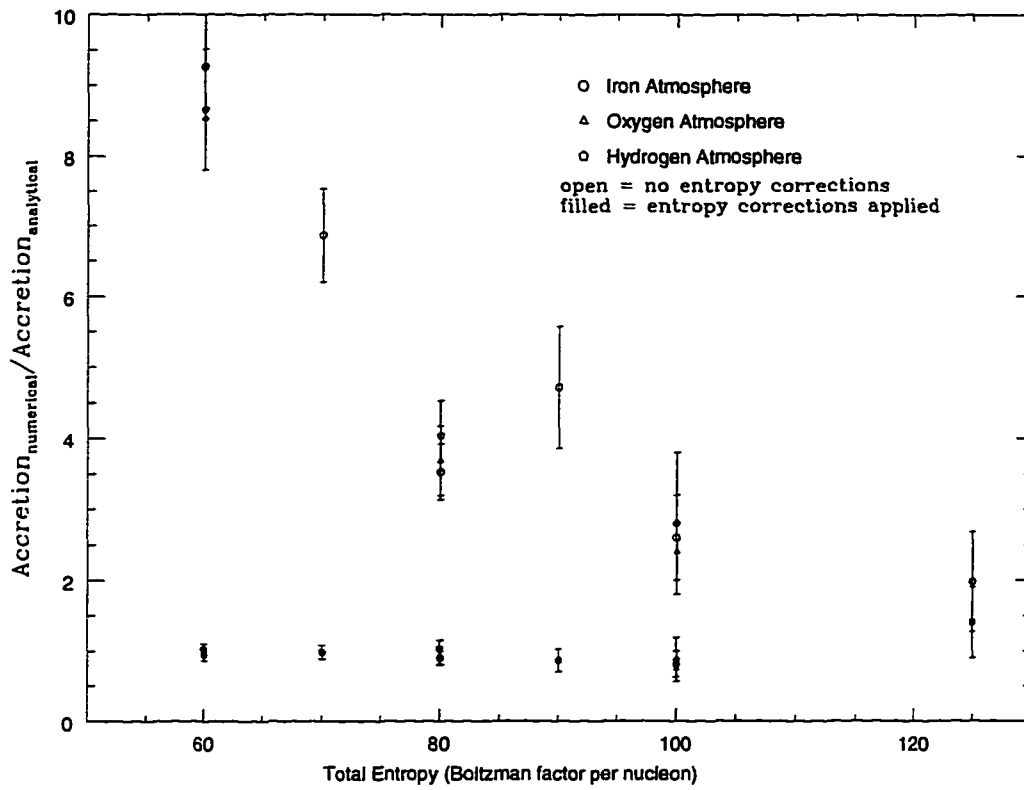


Figure 2.14 a comparison between numerical accretion rates and the analytical results of Colgate et al. (1993). The filled circles compare analytical results using only the radiation entropy from the numerical calculations, whereas the open symbols use the total entropy.

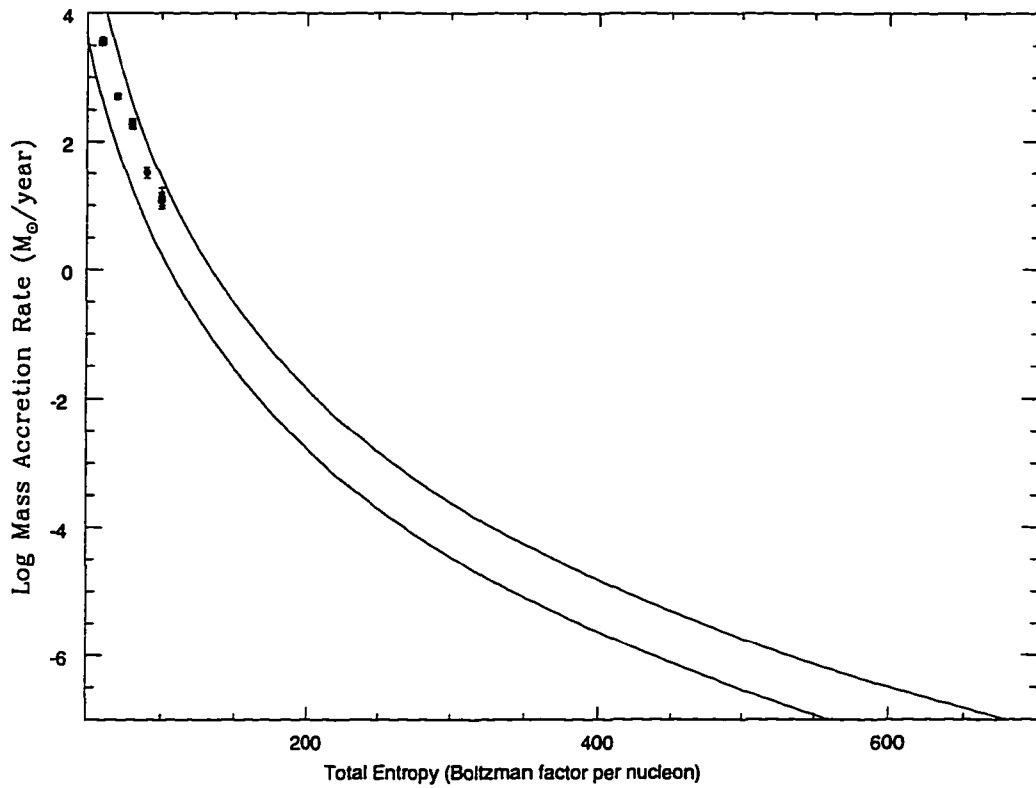


Figure 2.15 accretion rate versus entropy. The two lines denote analytical results using outer pressures of 0% and 0.25% that of the pressure at the surface of the neutron star. The points are results from the simulations.

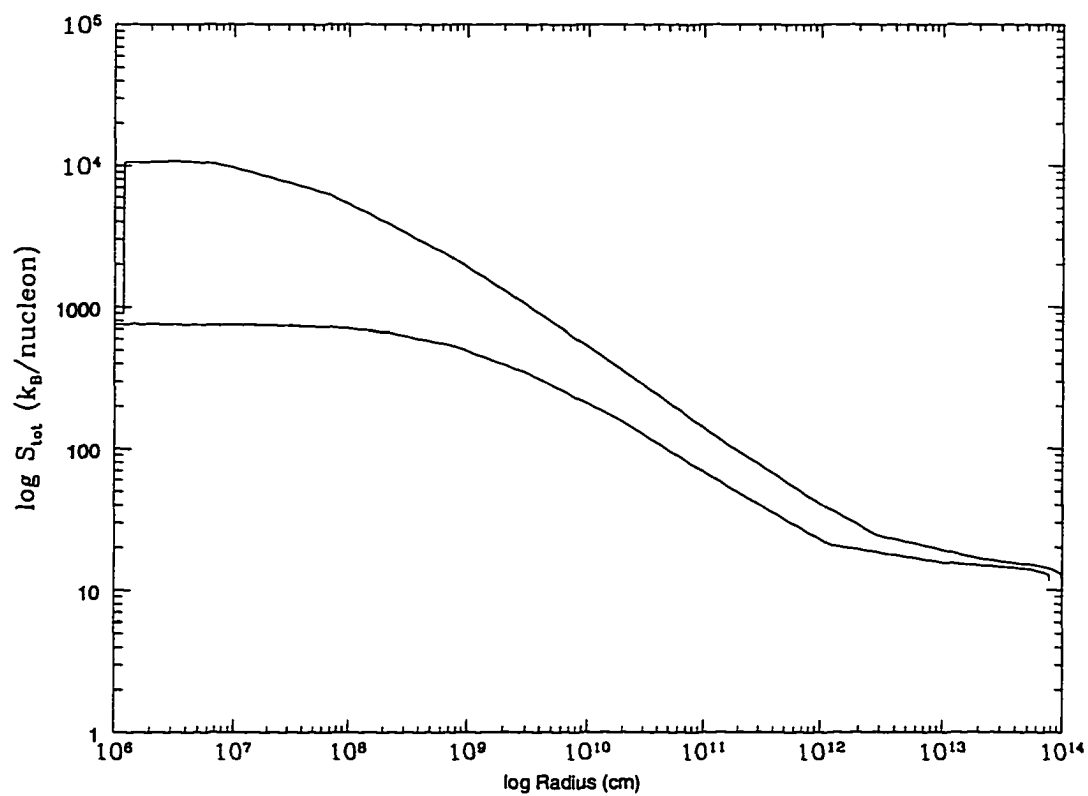


Figure 2.16 entropy profiles versus radius for the nucleosynthesis models of Cannon (top line) and Biehle (bottom line).

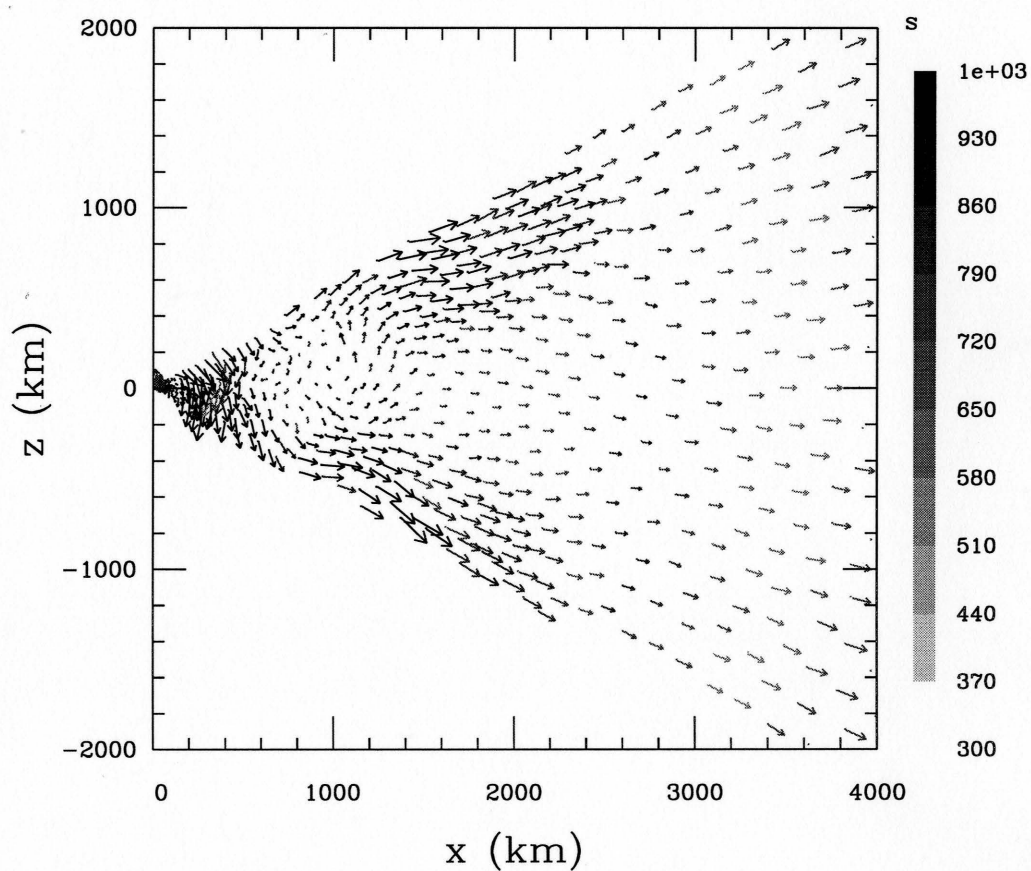


Figure 2.17 Biehle's structure model after 0.5 s. The high entropy material is driving the atmosphere outward. Outward velocities approach 6000 km/s.

CHAPTER 3

DOUBLE NEUTRON STAR SYSTEMS: EVIDENCE FOR KICK VELOCITIES

Brief Summary We study the four double neutron star systems found in the Galactic disk in terms of the orbital characteristics of their immediate progenitors and the kicks imparted to neutron stars at their formation. First, we address the issue of the nature of the radio pulsar companions. We find the evidence that they are indeed neutron stars to be adequately convincing, although not conclusive. Analysis of the effect of the second supernova (SN) explosion on the orbital dynamics of the systems combined with results from simulations of common-envelope evolution and accretion onto neutron stars lead us to conclude that the observed systems could not have been formed had the explosion been symmetric. The conclusion is independent of the evolutionary sequence followed by the progenitors, and remains unaltered even when we account for post-SN orbital evolution due to gravitational radiation, as well as when we relax the assumption of pre-SN circular orbits.

The formation of the observed systems becomes possible only if kick velocities are imparted to the pulsar companions at birth. We study the limits imposed on the progenitor characteristics, orbital separations and masses of the exploding stars, and study their dependence on the magnitude of the kick velocity and the time elapsed since the explosion. For each of the double neutron stars, we are able to derive a minimum kick velocity required for their formation. For the two systems in close orbits ($\lesssim 10 R_\odot$), the lower limits are as high as 250 km/s. Moreover, we calculate the center-of-mass velocities acquired at the explosion and we find them to be in agreement with the current observations of proper motions.

Subject headings: stars: neutron – pulsars: general – supernovae: general

3.1. Introduction

The prototypical Double Neutron Star (DNS) system containing PSR 1913+16 was discovered in 1975 by Hulse & Taylor. This discovery was the first of a binary pulsar for which observational data strongly suggested that both components are compact objects. One of the two members is undoubtedly a neutron star since it is detected as a radio pulsar. Over the years, several astrophysical tests have been developed to reveal the nature of the pulsar companion. Their results strongly indicate that it is either another neutron star or a black hole (for detailed discussions see Taylor & Weisberg 1982, 1989).

Following PSR 1913+16¹, additional DNS candidate systems have been

¹Hereafter, we will refer to the double neutron star systems using the designation of their radio pulsar component

discovered: PSR 2303+46 (Stokes, Taylor, & Dewey 1985), PSR 2127+11C (Anderson et al. 1990), PSR 1534+12 (Wolszczan 1991), and PSR J1518+4904 (Nice, Sayer, & Taylor 1996). Their relatively recent discoveries have not allowed a detailed investigation of the pulsar companions in these systems. However, the inferred total masses for all of these systems lie within a narrow range of values, $\sim 2.5 - 2.8 M_{\odot}$, and their orbits are highly eccentric. These parameters are sufficiently similar to those of PSR 1913+16 to suggest that they are also DNS systems.

Despite their small number, double neutron stars have proven to be highly important objects for relativistic astrophysics. The orbital evolution of PSR 1913+16 due to gravitational radiation has provided additional confirmation of general relativity, which may be corroborated by PSR 2127+11C and 1534+12 in the future (Taylor & Weisberg 1982, 1989). Furthermore, mergers of close DNS systems represent one of the primary sources of gravitational wave emission expected to be detected by observatories such as LIGO and VIRGO (for a review see Thorne 1996). Such mergers have also been invoked in theoretical models for the origin of gamma-ray bursts (Paczynski 1986).

The existence of DNSs has instigated studies of their origin and a variety of evolutionary sequences have been proposed for their formation (Webbink 1975; Smarr & Blandford 1976; Srinivasan & van den Heuvel 1982; Burrows & Woosley 1986; Brown 1995; Terman, Taam, & Hernquist 1995). Regardless of the details of prior evolution, all formation mechanisms converge to a helium-star/neutron-star binary systems for the immediate progenitors of the observed double neutron stars. The helium star then collapses to form the companion to the observed pulsar, a neutron star (or possibly a black hole).

In this paper, our goal is to study the origin of the observed double neutron star systems and in particular, to constrain the binary characteristics of their immediate progenitors. Before addressing the evolutionary issues involved, we examine in detail the existing evidence that the pulsar companions in all five systems are indeed compact objects by applying the tests previously developed for PSR 1913+16 (§ 3.2). In § 3.3 we review the various formation mechanisms for DNSs and identify the qualitative properties of their immediate progenitors. The possibility that such progenitors lead to the formation of DNSs via symmetric supernova explosions is investigated in § 3.4. Considerations of the orbital dynamics related to such explosions, along with recent results on the fate of neutron stars in common envelope phases (Chevalier 1993, 1996; Brown 1995; Terman, Taam, & Hernquist 1995; Fryer, Benz, & Herant 1996) lead us to the conclusion that the second supernova in DNSs could not have been symmetric, and that kick velocities were imparted to the neutron stars at birth. Our conclusion holds even when we take into account post-supernova orbital evolution due to gravitational radiation and allow for eccentric pre-supernova orbits. In view of these results, in § 3.5 we expand our study of DNS formation to include the effects of kick velocities and find that double neutron stars are then formed. We are able to identify the properties of DNS progenitors, i.e. orbital separations and masses, which we find to be restricted in relatively narrow ranges. In addition, we derive an absolute lower limit on the magnitude of the kick needed for the formation of the observed systems. For reasons of completeness, the case of eccentric pre-supernova orbits is also studied. We conclude with a discussion of the implications of our results for the intrinsic kick velocity distribution and the center-of-mass velocities of double neutron stars.

3.2. The Nature of the Pulsar Companion

Before studying the origin of double neutron star systems, we must first understand the nature of the companions to the observed radio pulsars. Although the pulsars are assuredly neutron stars, the properties of their companions are not so easily constrained. In principle, they can be either extended stars (main sequence or helium stars) or compact objects, such as white dwarfs, neutron stars, or black holes. For PSR 1913+16, a variety of tests has been developed supporting the idea that the pulsar companion is a compact object (Taylor & Weisberg 1982, 1989). In this section, we apply these tests to the entire set of DNS candidates.

The current sets of measured and inferred properties of all five double neutron star candidate systems are listed in Table 3.1. The results from some of the tests that we discuss here rely upon having accurate determinations of the masses of each of the binary components. For two of the systems, PSR 1913+16 and 1534+12, the timing observations are precise enough that not only the periastron advances but also the gravitational redshifts and second-order Doppler shifts can be measured. These are used to determine the individual masses of the two components to a high accuracy (less than 3% under the assumption that the rate of periastron advance is purely relativistic). For the other three systems, only the total mass has been accurately determined. Although, one can use statistical arguments to estimate the individual masses, direct measurements are not yet available. Given that the values of the well-determined component masses in two of the systems are strikingly similar, for the three remaining systems we simply assume that the individual component masses are equal. Our results do not change significantly by using the range of masses from the statistical estimates.

3.2.1. Roche Lobe Overflow

We consider the case that the companions to the pulsars are extended stars. Roche lobe overflow at some position along the binary orbit would then result in accretion onto the pulsar (Davidsen et al. 1975). Since no X-rays are detected from the observed systems, we can exclude extended companions with radii greater than the Roche lobe radii at periastron (Masters & Roberts 1975).

The radius of the Roche lobe of the pulsar companion at periastron is given by

$$R_L = \frac{0.49q_c^{2/3}}{0.6q_c^{2/3} + \ln(1 + q_c^{1/3})} A (1 - e), \quad (51)$$

where $q_c \equiv M_c/M_p$, M_p and M_c being the pulsar and companion masses respectively, A is the orbital separation, e is the eccentricity, and we have used the expression for the Roche lobe radius normalized to the orbital separation given by Eggleton (1983). For main-sequence stars, we use the radius-mass fitting relation given by Kalogera & Webbink (1996), and for helium stars we use the relation given by Wijers, van Paradijs, & van den Heuvel (1992). The calculated ratios of Roche lobe radius, R_L , to the radii of a main-sequence and a helium star, R_{MS} and R_{He} , are given in Table 3.1 for all five systems.

It is evident that for PSR 1913+16, 1534+12, and 2127+11C, the companion cannot be a main sequence star since the above ratio is smaller than unity. The conclusion is not altered by the use of other radius-mass relations existing in literature such as Iben (1967), Cisneros-Parra (1970), and Allen (1973). However, the orbits of PSR 2303+46 and PSR 1518+4904 are wide enough to accommodate a main sequence companion even at periastron. Helium stars are so compact that they could fit within their Roche lobes in all five systems.

3.2.2. Rate of Periastron Advance

Precession of the longitude of periastron in the DNS orbits is one of the primary quantities derived from detailed pulsar timing models fit to observational data. Under the assumption that the periastron advance (also referred to as apsidal motion) is purely relativistic, it can be used as a constraint to the total mass of the binary (Masters & Roberts 1975; Smarr & Blandford 1976). However, tidal and rotational distortions may, in principle, contribute to the observed precession rate. In the case of compact objects, these effects are negligible. On the other hand, the precession rate for extended stars may exceed the observed value, thus excluding such pulsar companions. In what follows, we examine in detail the possible contributions to the measured periastron advance rates of extended stars due to both tidal and rotational effects.

Provided that the companion reacts to an external torque as a rigid body and the angle between the total and orbital angular momentum axes is small (see Smarr & Blandford 1976), the periastron advances due to both tidal and rotational effects are given by²

$$\dot{\omega}_{\text{tid}} = 5.4 \times 10^3 k \frac{M_p}{M_c} \left(\frac{R_c}{A} \right)^5 F(e) P^{-1} \text{ deg yr}^{-1}, \quad (52)$$

$$\dot{\omega}_{\text{rot}} = 2.4 k \frac{R_c^5}{A^2 M_c P_c^2 P} (1 - e^2)^{-2} \left(1 - \frac{3}{2} \sin^2 \theta \right) \text{ deg yr}^{-1}, \quad (53)$$

where k is a measure of the central concentration of the companion³, P is the orbital period in years, $F(e) \equiv (1 - e^2)^{-5} (1 + \frac{3}{2}e^2 + \frac{1}{8}e^4)$, θ is the angle

²Hereafter, all masses and radii are expressed in solar units

³We use $0.005 < k < 0.01$ main-sequence stars (Schwarzschild 1958) and $k = 0.06$ for helium stars (Roberts, Masters & Arnett 1976).

between the companion's spin and the orbital angular momentum axes, and P_c is the spin period of the companion in days. Unless the companion is spinning very rapidly, the rotational apsidal progression is small compared to the tidal advance. Depending on the angle θ , the rotational precession can acquire negative values causing a periastron *regression*. In principle, this could cancel out the tidal and relativistic rate; however, it is typically too small to appreciably affect the total precession rate. We evaluate both precession rates for main-sequence and helium stars adopting a typical spin period of 1 day and assuming that the spin and orbital angular momentum axes are aligned, $\theta = 0$; the results are given in Table 3.1.

For PSR 1913+16, 1534+12, and 2127+11C, both main-sequence and helium-star companions are safely ruled out since the predicted tidal advances typically exceed the observed value and the rotational part is too small to cancel the tidal effect. For the other two systems, the rates are all too small to have a significant contribution, and hence they can't be used to exclude extended companions.

3.2.3. Optical Identification of the Companion

The most direct way of revealing the nature of the companion is to actually observe it! Optical observations can be used to exclude both extended stars and white dwarfs (Davidsen et al. 1975). We estimate visual magnitudes using the information about the companion masses, distances and positions on the sky. For main-sequence stars we adopt an F5 spectral type ($M_V = 3.5$), which is appropriate for the measured companion masses (Allen 1973), and for white dwarfs of different temperatures, and hence ages, we use the models by Bergeron, Wesemael, & Beauchamp (1995). We also apply a reddening correction using the maps of Burstein & Heiles (1982) and the extinction relation: $A_V = E(B - V)/0.3$. The

estimated values are given in Table 3.1. We note that helium stars are typically more luminous than main sequence stars of the same mass (Habets 1985; Allen 1973). Main sequence and helium star companions would be easily detected for all five systems. White dwarfs on the other hand would be detected in PSR 1534+12, 1518+4904, and possibly PSR B2303+46. Relatively deep optical searches have been performed only for PSR 1913+16 and 1518+4904 (Crane, Nelson, Tyson 1979; van Kerkwijk 1996). These safely exclude main sequence and helium star companions but not the possibility of white dwarf companions.

3.2.4. Summary

For four of the pulsars (1913+16, 1534+12, 1518+4904, and 2127+11C), the presence of an extended companion is excluded based on their stellar size, their implied periastron advances and/or their non-detection in optical. For PSR 2303+46 such a companion can be easily ruled out by optical observations (down to a visual magnitude of 16-17). White dwarf companions can in principle be excluded for three of the five pulsars (1534+12, 2303+46, 1518+4904) using deep enough optical observations, whereas the distances to PSR 1913+16 and 2127+11C are so high that even hot white dwarfs would remain undetected.

However, additional arguments have been proposed to rule out white dwarf companions. In the Galactic field, all binary pulsars known to have white dwarf companions are found in circular orbits (van den Heuvel 1994, 1995), in contrast to the five systems studied here. Provided that the observed pulsars have indeed been recycled, as suggested by Srinivasan & van den Heuvel (1982) based on their low inferred magnetic fields (see Table 3.1), the recycling process must have circularized the orbit. The observed eccentricities then can only be explained by invoking a supernova explosion following the mass transfer phase, which would

then lead to the formation of a compact companion, a neutron star or a black hole. Furthermore, this second supernova explosion (and, in particular, an explosion imparting a kick to the collapsed object) is supported by observational evidence for the spin axis of the pulsar being misaligned with the orbital momentum axis, in the case of PSR 1913+16 (Kaspi et al. 1996).

Given all of the above arguments that these pulsar companions are neither extended stars nor white dwarfs, we regard the evidence for neutron star (or black hole) companions to be quite convincing.

3.3. Formation Mechanisms

The standard formation mechanism for double neutron stars (Srinivasan & van den Heuvel 1982) involves the evolution of a massive binary system. As the more massive star evolves, it fills its Roche lobe and transfers mass to its companion until its hydrogen envelope is exhausted. Further evolution of the remnant helium core leads to a supernova explosion and the formation of a neutron star. As its massive companion evolves to become a red giant, the neutron star accretes matter from the stellar wind and the system appears as a high-mass X-ray binary. Further expansion of the companion eventually leads to Roche lobe overflow and spiral in of the neutron star into the hydrogen envelope of its companion. Provided that the orbit at the onset of the common envelope (CE) phase is sufficiently wide, the stars do not merge and a binary consisting of a neutron star and a helium star remains after the ejection of the envelope. Due to mass transfer before and/or during the common envelope phase, the neutron star is recycled to short (\sim ms) spin periods. Furthermore, dissipative processes during mass transfer lead to a tight circular orbit for the He-star/neutron-star binary. Depending on its mass, the

helium star may terminate its evolution with a supernova explosion (the second in the evolutionary history of the system) and the formation of another neutron star.

Variations of the above evolutionary sequence have been proposed by Terman & Taam (1995) to ensure that the neutron star will not merge with its companion during the CE phase. This requires that the pre-CE orbits be sufficiently wide, which can be achieved: (i) by partial loss of mass and angular momentum during the first mass transfer phase, or (ii) by avoiding this mass transfer phase altogether with the binary members evolving independently until the formation of the neutron star. Another variation has been proposed by van den Heuvel, Kaper, & Ruymaekers (1994) to explain the existence of the double neutron star systems with wide orbits (PSR 2303+46, 1518+4904). In this evolutionary sequence, the neutron star does not go through a common envelope phase, but instead the hydrogen envelope is lost in a strong wind.

Studies of highly supercritical accretion onto neutron stars (Chevalier 1993; Brown 1994) indicate that matter can be accreted at rates much in excess of the photon Eddington limit, leading to the collapse of the neutron star into a black hole (although spiral-in through a hydrogen envelope may still be viable; see Chevalier 1996; Fryer et al. 1996). To overcome this difficulty Brown (1995) suggested that double neutron stars are formed by stars with masses within 4% of each other, which evolve through two mass transfer phases to a binary consisting of two helium stars of almost equal mass. The subsequent supernova explosions of these lead to the formation of two neutron stars.

In this paper, we focus our interest on the binary characteristics of the immediate progenitors of double neutron star systems and the nature of the second supernova explosion. From the description of the various evolutionary channels,

it becomes evident that they all converge to the same configuration prior to the formation of the second neutron star: a binary consisting of a neutron star and a helium-star in a circular orbit. Therefore, this is the configuration on which we base the analysis that follows.

One of the five double neutron star systems, PSR 2127+11C, is found in a globular cluster (Anderson et al. 1990). Anderson et al. showed that, given the dense stellar environment for this system it is quite possible that it was formed via dynamical interactions (capture or exchange) and not through one of the evolutionary sequences described in this section. For this reason, we will not study it further.

3.4. Symmetric Explosions

According to all the formation mechanisms suggested so far, the immediate progenitors of double neutron star systems consist of a helium star and a recycled pulsar. In this section, we investigate the formation of the companion neutron star via the supernova explosion of the helium star. We use the knowledge of the present binary characteristics to derive the corresponding parameters of the progenitors just prior to the explosion (pre-SN). As a first step, we assume that the explosion is symmetric, its only effect being an instantaneous mass loss from the system. Since the radius of the pulsar is much smaller than the orbital separation ($\sim 1 R_{\odot}$), we may neglect the effect of the interaction between the pulsar and the supernova ejecta. Combining our results for the pre-SN configuration and recent developments on common envelope evolution of inspiraling neutron stars, we conclude that the four observed double neutron star systems cannot be formed unless a kick velocity is imparted to the nascent neutron star.

3.4.1. Orbital Dynamics

We assume, for simplicity, that the double neutron star systems have experienced no post-supernova orbital evolution (the validity of this assumption will be examined in §3.4.1.1). Then for each of the observed systems, the post-SN characteristics are known: eccentricity, e , pulsar mass, M_p , companion mass, M_c , and orbital separation, A , or period, P . We denote the corresponding parameters for the pre-SN system with a subscript “ o ”. The pulsar mass remains the same before and after the explosion, while the mass of the exploding star is M_o .

For the general case of eccentric pre-SN orbits, the relations connecting the pre- and post-SN states have been derived by Hills (1983):

$$\frac{A}{A_o} = \frac{(M_o + M_p) - (M_o - M_c)}{(M_o + M_p) - 2(A_o/r)(M_o - M_c)}, \quad (54)$$

and

$$e = \left\{ 1 - (1 - e_o^2) \left(1 - 2 \frac{A_o}{r} \frac{M_o - M_c}{M_o + M_p} \right) \left(1 - \frac{M_o - M_c}{M_o + M_p} \right)^{-2} \right\}^{1/2}, \quad (55)$$

where r is the distance between the two stars, M_o and M_p , at the time of the supernova explosion. For a circular pre-SN orbit $r = A_o$.

As discussed in §3.3, all current formation mechanisms for double neutron stars involve mass transfer to and recycling of the first neutron star, and thus lead to the circularization of the orbit prior to the formation of the second neutron star. Accordingly, we assume that the pre-SN orbit is circular. We then use equations (3) and (4) to solve for the pre-SN orbital separation, A_o

$$\frac{A_o}{A} = \frac{M_p + 2M_c - M_o}{M_p + M_c}, \quad (56)$$

and the mass of the exploding star, M_o

$$M_o = e(M_p + M_c) + M_c. \quad (57)$$

According to the formation mechanisms, the exploding star is an evolved helium star, which is also the most compact possible configuration for the progenitor of the pulsar companion. During the course of their evolution, helium stars less massive than $3.5 M_{\odot}$ expand significantly. We use a fit for the maximum helium-star radius, R_{max} , as a function of its mass, M_{He} , (Kalogera & Webbink 1996) based on helium star models calculated by Habets (1985) (in agreement with Woosley, Langer, & Weaver 1995):

$$\log R_{max} = \begin{cases} 3.0965 - 2.013 \log M_{He} & M_{He} \leq 2.5 M_{\odot} \\ 0.0557 (\log M_{He} - 0.172)^{-2.5} & M_{He} > 2.5 M_{\odot}. \end{cases} \quad (58)$$

The results for the pre-SN orbital separations and helium star masses, and the corresponding helium-star maximum radii are listed in Table 3.2 for all DNS systems. It is evident that in all cases, the stellar radius of the NS progenitor is greater than the orbital separation. In other words, under the assumption of a symmetric supernova explosion, we find that for the progenitors of *all* the observed systems, the pulsar lies within its companion at the time of the supernova explosion. For PSR 1913+16, this problem was also recognized by Burrows & Woosley (1986). In what follows we investigate the robustness of this conclusion.

Gravitational Radiation

In the previous analysis, we assumed, as all work to date has, that the observed double neutron star systems have not experienced any orbital evolution since their formation (Wijers, van Paradijs, & van den Heuvel 1992 recognized the possibility but did not account for the effect). However, both orbital separations and eccentricities do evolve because of gravitational wave emission. Hence, the observed orbital parameters are not necessarily identical with those of the post-SN

binaries.

We use the expressions derived by Junker & Schaefer (1992) for orbital evolution due to gravitational radiation, and calculate the post-SN orbital separation and eccentricity as a function of the time elapsed since the explosion, T_{SN} . This effect is most evident for the close systems, PSR 1913+16 and 1534+12 (see Figure 1).

Allowing for orbital evolution due to gravitational radiation we re-calculate the pre-SN separations, A_o , progenitor masses of the pulsar companions, M_o , and the ratios of Roche lobe over helium-star maximum radii, R_L/R_{He} , as functions of T_{SN} . The results for PSRs 1913+16 and 1534+12 are shown in Figure 2, while the range of radii ratios for all systems are given in Table 3.2. Based on these results we conclude that post-SN orbital evolution does not alter our conclusion: the progenitors of the second neutron stars for all observed systems overfill their Roche lobes prior to the explosion, even in this case. Hence, under the assumption of a symmetric supernova, the explosion occurred during a common envelope phase.

Eccentric Pre-SN Orbits

Despite the fact that all current evolutionary sequences for the formation of double neutron stars involve a circular orbit, we can still investigate the robustness of our conclusion that the pulsar enters a common envelope phase, by allowing for eccentric pre-SN orbits.

In this case, we use the general equations (3) and (4). There are four unknown pre-SN characteristics: orbital separation, helium-star mass, pre-SN eccentricity, e_o , and the distance, r , between the two stars at the time of the explosion. Since

we only have two equations, we treat two of the above quantities, e_o and M_o , as parameters and solve for A_o and r . Note that r can acquire values within a restricted range, between periastron and apastron of the pre-SN orbit (from $A_o(1 - e_o)$ to $A_o(1 + e_o)$). The ratio of the Roche lobe radius to the maximum radius for the helium star as a function of M_o and for a complete range of pre-SN eccentricities is shown in Figure 3 for all four of the observed systems (see also Table 3.2). We see for PSR 1913+16 and 1534+12 that the helium star overfills its Roche lobe, whereas for PSR 2303+46 and 1518+4904 the ratio R_{He}/R_L may exceed unity by a small factor. However, even in these cases it is quite improbable that the pulsar will not spiral into its companion's envelope, because of the onset of the tidal instability (e.g. Rasio 1996). Such an instability sets in when the sum of spin angular momenta of the binary members exceeds one third of the orbital angular momentum. This can occur when one of the stars expands appreciably and almost fills its Roche lobe, as is the case for PSR 2303+46 and 1518+4904. Therefore, even for the extreme case of eccentric pre-SN orbits our conclusion remains unaltered and, under the assumption of a symmetric supernova explosion, the pulsar experiences common envelope evolution before the explosion.

3.4.2. Neutron Stars in Common-Envelope Phases

For a symmetric explosion, the immediate progenitors of double neutron star systems must evolve through a common-envelope (CE) phase. Therefore, it is essential to investigate the fate of neutron stars spiraling into the envelope of an evolved helium star. In this section, we use recent results on CE evolution and conclude that survival of a neutron star through such a phase is not possible.

Terman, Taam, & Hernquist (1995) have studied the inspiral of a neutron star in the hydrogen envelope of a massive star. They find that the inspiral time is

very short ($\sim 1 - 100$ yr). Whether or not the neutron star merges into the core depends not only on the amount of orbital energy at the onset of the spiral-in (which should be large enough to overcome the binding energy of the envelope), but also on the evolutionary stage of the extended star. Their simulations indicate that the massive star must be sufficiently evolved to form a steep density gradient in its interior.

Although massive stars with hydrogen envelopes develop steep density profiles during their core helium burning, evolved helium stars do not exhibit such a distinct core-envelope separation (helium-star models by Woosley 1996). Their density structure is smoother, and hence the neutron star would spiral all the way into the core with the infall time-scales ($\sim 1 - 100$ yr) predicted by Terman et al. (1995). As a result the binary system is destroyed unless the helium star can evolve more rapidly than the infall phase and explode as a supernova before the neutron star merges into the core. Using the pre-SN parameters derived in § 3.4.1 and helium-star evolutionary models by Habets (1985), we calculate the time interval, T_{ev} , between Roche lobe overflow and collapse (Table 3.2). For all of the systems, these evolutionary time scales greatly exceed the predicted spiral-in times indicating that the neutron star merges before the explosion occurs. We should note, however, that the above calculations have received some criticism (Rasio & Livio 1996) because of the very low resolution (3000 particles for a three-dimensional model) of the Smooth Particle Hydrodynamics (SPH) simulations. Although low-resolution effects render the quantitative results suspect, the qualitative conclusions for the fate of the CE phase may still be valid.

Accretion of matter onto the neutron star is another aspect of CE phases which has recently been studied by various investigators (Chevalier 1993, 1996;

Brown 1995; Fryer et al. 1996). In common envelope situations, the Bondi-Hoyle accretion rate (Bondi 1952) typically exceeds $\sim 10^{-4} M_{\odot} \text{y}^{-1}$, which is much greater than the photon Eddington limit for neutron stars. For such high accretion rates, neutrino emission dominates the cooling processes. In these cases, accretion is not limited by the photon Eddington limit, but instead by the corresponding limit for neutrinos, which is 20 orders of magnitude greater than the photon Eddington limit. For the calculated Bondi-Hoyle rates, neutrino emission carries away the energy released by accretion and a steady state flow is achieved. At these high rates, the pulsar collapses into a black hole on a time scale of hours or months soon after it enters the envelope of its companion.

In the standard formation mechanism (and its variations) for double neutron stars, the pulsar spirals into a hydrogen rich envelope before the helium-star/neutron star binary is formed. The above results imply that the DNS progenitors are destroyed at that early stage. These considerations led Brown (1995) to suggest an alternative formation mechanism which circumvents such a CE phase. However, depending on the conditions in the common envelope, other physical processes can facilitate the survival of the neutron star. Chevalier (1996) showed that angular momentum accreted with the material onto the neutron star may prevent collapse. Also, Fryer et al. (1996) found that the neutrinos emitted close to the neutron star may be able to heat a region of the infalling atmosphere, and ultimately drive an explosion which temporarily halts mass accretion. A series of such explosions may also prohibit the collapse of the neutron star into a black hole. However, in the envelopes of helium giants, the densities and temperatures are such that neither of these processes are sufficiently important to prevent accretion from reaching high rates.

Effects of Angular Momentum

Material being accreted onto the neutron star is expected to contain a certain amount of angular momentum due to density and velocity gradients in the flow. Infall of material is halted at all polar angles except in a cone around the poles defined by the angular momentum axis. For a given value of the specific angular momentum, j , we can define a critical polar angle, θ_c , within which angular momentum does not affect the inflow appreciably. This angle is set by the balance between the centrifugal and gravitational forces at the neutron star radius:

$$\frac{j^2 \sin^2 \theta_c}{R_{NS}^3} = \frac{G M_{NS}}{R_{NS}^2}, \quad (59)$$

where M_{NS} and R_{NS} are the mass and radius of the neutron star. For the specific angular momentum we use the analytical estimates by Ruffert & Anzer (1995):

$$j \equiv \frac{\dot{J}}{\dot{M}} = \frac{1}{4} (6\epsilon_v - \epsilon_\rho) V R_B, \quad (60)$$

where \dot{J} and \dot{M} are the angular momentum and mass accretion rates respectively, V is the velocity of the neutron star, R_B is the Bondi-Hoyle accretion radius (Bondi 1952), and ϵ_v , ϵ_ρ are the velocity and density gradient parameters, as defined in Ruffert & Anzer (1995).

For the observed systems, we have derived the mass of the progenitor of the second neutron star as well as the position of the pulsar in the envelope of its companion, that is the pre-SN orbital separation (Table 3.2). Using helium star models by Woosley (1996) we calculate the Bondi-Hoyle accretion rates and radii appropriate for the conditions in the stellar envelopes. We have assumed that the neutron star velocity in the envelope is equal to the pre-SN relative orbital velocity. The results for both cases, with and without angular momentum accretion, are listed in Table 3.2. Also, the ratio of the Bondi-Hoyle radius to that of the helium

stars are listed; this ratio must remain smaller than unity to ensure that the flow region is included in the stellar envelope.

Given the above accretion rates we can calculate the time T_{BH} required for the neutron star to accrete $\sim 1 M_{\odot}$ of matter and collapse to a black hole (see Table 3.2). Only when T_{BH} is greater than T_{ev} , the time interval between Roche lobe overflow and collapse of the helium star, will the neutron star survive the CE phase. For all observed systems (with the possible exception of J1518+4904), the collapse time scale is many orders of magnitude *shorter* than the evolution time scale, clearly indicating that the pulsar becomes a black hole long before the SN explosion. We note that numerical calculations indicate that equation (60) overestimates the amount of angular momentum accreted onto the neutron star (Ruffert & Anzer 1995). Moreover, we have ignored any effects of angular momentum transport which must be present to some degree (Chevalier 1996). Ignoring these effects underestimates the mass accretion rate and overestimates the time required for collapse.

Until now we have implicitly assumed that the derived distances of the pulsars prior to the explosion represent the pre-SN orbital separations. However, this may not be necessarily true. It is possible that the neutron star has reached such a short distance from the helium-star core because of spiral into the envelope. We can still apply the above time scale arguments, but rather than T_{ev} , we use the shortest possible time from the onset of the CE phase to the supernova stage. This is defined as the interval, T_{CE} , between the time that the helium star acquires its maximum radial extent and the time of its collapse (see Table 3.2). We note that T_{CE} is prohibitively long for all the observed pulsar systems.

In view of the above analysis, we conclude that the pulsar does not survive a

common envelope phase with its helium star companion. A merger with the core and, more importantly, a collapse into a black hole will precede the supernova explosion of the helium star. These circumstances do not lead to the formation of a double neutron star system.

3.5. Asymmetric Explosions

We have already shown that, under the assumption of symmetric supernova explosions, the pre-SN orbital separations for the progenitors of the observed double neutron star systems places the pulsars within the envelopes of their helium-star companions. The times required for both inspiral and black-hole collapse are much shorter than the evolution time interval from the onset of the CE phase to helium-star SN explosion. Under these conditions, double neutron star formation is aborted. Neither post-SN orbital evolution due to gravitational radiation nor pre-SN eccentric orbits alters this conclusion. The only remaining assumption, is that of a symmetric supernova explosion. To form double neutron star systems we are then forced to relax this assumption and examine the case that asymmetries are present and a kick is imparted to the nascent compact object.

Kick velocities acquired at the supernova explosion indeed allow the observed double neutron stars to be formed. However, the range of pre-SN binary parameters is restricted to relatively narrow ranges. We study the dependence of these parameters on the magnitude of the kick velocity, the time elapsed since the SN explosion, and eccentric pre-SN orbits. For each of the systems we calculate the minimum value of the kick velocity that is necessary for the pre-SN system to avoid a CE phase.

3.5.1. Circular Pre-SN Orbits

First, we study the case of circular pre-SN orbits, which is consistent with the DNS formation mechanisms. Using the orbital energy and angular momentum equations for eccentric orbits, and for a kick velocity of specific magnitude and direction, expressions for the pre-SN orbital separation, A_o , and mass of the helium star, M_o , as a function of the post-SN binary characteristics can be derived (e.g. Kalogera 1996):

$$V_k^2 + V_r^2 + 2V_k V_r \cos\theta = G(M_p + M_c) \left(\frac{2}{A_o} - \frac{1}{A} \right), \quad (61)$$

$$A_o^2 \left[V_k^2 \sin^2\theta \cos^2\phi + (V_k \cos\theta + V_r)^2 \right] = G(M_p + M_c) A (1 - e^2), \quad (62)$$

where V_r is the relative orbital velocity before the explosion

$$V_r = \left[\frac{G(M_o + M_p)}{A_o} \right]^{1/2}, \quad (63)$$

V_k is the magnitude of the kick, θ is the polar angle of the kick with respect to the pre-SN orbital velocity of the helium star relative to the pulsar, and ϕ is the corresponding azimuthal angle. For each of the observed double neutron star systems, the post-SN parameters are known (at this point we ignore orbital evolution due to gravitational radiation, although we will come back to it later). For a specified kick magnitude in any direction, we calculate the two unknown pre-SN parameters, A_o and M_o .

The region of allowed pairs of values is restricted by a set of constraints that DNS progenitors must satisfy. The first of the constraints arises from the fact that the post-SN orbit must include the position of the two stars at the time of the explosion (see e.g. Kalogera 1996), hence the pre-SN separation must be within the bounds set by the periastron and apastron distances in the post-SN orbit

$$A(1 - e) \leq A_o \leq A(1 + e). \quad (64)$$

These limits can be derived using equations (61) and (62) and requiring that $\cos^2 \phi \leq 1$, where the equality corresponds to kicks perpendicular to the orbital plane.

A second constraint is set by demanding that $\cos^2 \phi$ remains always positive. Using equations (61) and (62) we find that for a specific pre-SN separation the mass of the helium star is restricted by:

$$M_o \leq \frac{2 k^2 (M_p + M_c)}{2 \alpha [2 \alpha^2 (1 - e^2) - k] - 4 \alpha^2 (1 - e^2)^{1/2} [\alpha^2 (1 - e^2) - k]^{1/2}} - M_p, \quad (65)$$

where

$$k = 2 \alpha - \left[\frac{V_k^2 A}{G(M_p + M_c)} + 1 \right] \quad (66)$$

and $\alpha = A/A_o$. The extreme case of $\cos^2 \phi = 0$ corresponds to kicks restricted in the plane of the orbit before the explosion. We can physically understand this constraint in terms of the orbital angular momentum content of the system before and after the explosion. Equation (65) expresses the maximum allowed M_o for a given value of A_o , and hence it corresponds to a maximum value of the pre-SN orbital angular momentum. The post-SN parameters fix the angular momentum content after the explosion, which is comprised of contributions from both the pre-SN orbital velocity and the kick velocity. Since their sum is fixed, the maximum pre-SN contribution is obtained when the kick contribution is minimum, and in fact opposes that of the orbit. Any component outside the pre-SN orbital plane increases the angular momentum of the system, therefore the kick contribution becomes minimal only when it lies in the orbital plane ($\cos^2 \phi = 0$).

The final constraint arises from the condition that the pulsar must avoid a common envelope phase with the helium star. The ranges of allowed values for A_o and M_o are then restricted by the condition that the helium star must fit within its Roche lobe when its radius is at a maximum (equation 58). At a given value of

A_o , a lower limit is derived for the mass of the helium star.

The limits imposed on the values of A_o and M_o are shown in Figures 4 and 5 for the two observed systems for which the individual masses are accurately known (PSR 1913+16 and 1534+12). For the close systems, $A_o \sim 3 - 4.5 R_\odot$ and $M_o \gtrsim 4M_\odot$ whereas for the wide binary systems $A_o \sim 20 - 50 R_\odot$ and $M_o \gtrsim 3 M_\odot$. The solid thick vertical line corresponds to the geometrical constraint (equation 64) and sets an upper limit on the pre-SN orbital separation. Although there exists a lower limit to A_o , as well, its value is too low to restrict the parameter space. The thin lines correspond to kicks imparted in the pre-SN orbital plane ($\cos^2 \phi = 0$), and thus to maximum pre-SN orbital angular momentum. Of the three limiting curves only the latter depends on the assumed kick magnitude. The relative orbital velocity in pre-SN orbits leading to the formation of the observed systems increases with increasing kick velocity. Thus, systems with shorter separations and more massive helium stars are included in the progenitor parameter space when the kick magnitude increases (see Figure 4).

We have already shown that in the absence of kick velocities none of the progenitors are wide enough to accommodate the evolved helium stars. Instead, sufficiently large separations and He-star masses are required to avoid Roche lobe overflow, which correspond to higher relative orbital velocities as well as larger amounts of mass lost in the explosions, compared to the case of symmetric explosions. Such progenitors are permitted only if the magnitudes of the kick velocities exceed a certain minimum value (see Figure 5), which is unique to each of the observed systems. For the two close systems, PSR 1913+16 and 1534+12 the minimum kick velocities that the pulsar companion acquired at its birth are as high as 290 and 230 km/s, respectively. For the wider systems, PSR 2303+46 and

1518+4904, the minimum kick magnitudes are lower, 70 and 50 km/s, respectively.

In the case of the observed double neutron star systems with small orbital separations ($\lesssim 5 R_\odot$), orbital evolution after the supernova explosion due to emission of gravitational waves has been found to be significant (see § 3.4.1.1). Therefore, post-SN orbital parameters for these systems may have been different than the ones observed at present. Consequently, the limits on the range of pre-SN parameters are also altered, with the exception of the limiting curve related to the size of evolved helium stars (thick solid lines in Figure 5). As the time, T_{SN} , elapsed since the explosion increases, post-SN separations and eccentricities increase too, and hence the maximum allowed pre-SN separations are shifted to higher values (equation 64). On the other hand, an increase in e and A may result in either an increase or decrease of the post-SN orbital angular momentum depending on whether the change in A or e , respectively, is more dominant. In either case, the change in the post-SN angular momentum is followed by an analogous change in that of the pre-SN orbit, and thus can lead to either an increase (PSR 1534+12) or a decrease (PSR 1913+16) of the upper limit on the mass of the helium star. The region of the A_o , M_o space allowed to progenitors becomes more extended the longer the time since the explosion, and progenitors become wider and wider. The decrease in relative orbital velocity before the explosion also results in a decrease of the minimum kick magnitude required for the formation of the observed systems, but not by a large amount. For values of T_{SN} equal to the characteristic age, τ_c , of the observed pulsar (Table 3.1), the minimum kick magnitude required decreases to ~ 250 km/s for PSR 1913+16. For the rest of the systems the effect is negligible.

3.5.2. Eccentric Orbits

Despite the fact that none of the current formation mechanisms requires an eccentric orbits for the pulsar-helium star binary, we explore such a possibility and its effect on the pre-SN binary parameters for completeness. As already discussed, in the case of eccentric orbits, the pre-SN parameter space becomes four-dimensional: the eccentricity, e_o , and the position along the orbits at the time of the explosion, expressed by the eccentric anomaly, E_o , are added to the orbital separation, A_o , and helium-star mass, M_o . We have sampled the complete range of values for both e_o (0 to 1) and E_o (0 to π), and calculated the outer envelope of the limits imposed on pre-SN separation and mass of the exploding star, based on the three physical constraints discussed above. These limits are shown in Figure 6 for PSR 1913+16 and 1534+12 for three different values of the kick magnitude and ignoring any post-SN orbital evolution. value. The lower limit on helium-star masses is not affected by eccentric orbits, although a significant expansion of the parameter space occurs towards more massive progenitors for the pulsar companion. However, we note that helium stars are known to lose mass in strong stellar winds and thus their masses at collapse are expected to be relatively small ($\lesssim 5 M_\odot$) (Woosley, Langer, & Weaver 1995). Finally, the minimum magnitude of a kick required for the system also remains unaltered.

3.6. Discussion

We have shown that for all candidate DNS systems detected so far, the evidence that the radio companions to the pulsars are not extended stars (main sequence or a helium stars) is adequately strong. The possibility that they are white dwarfs can not be completely excluded yet and deep optical observations would be decisive

PSR 1534+12 and 1518+4904. Support for the formation of these companions in a supernova explosion is also provided by the high measured eccentricities. Given the results of the detailed analysis presented in § 3.2 we conclude that white dwarf companions are unlikely.

A careful account of the change in orbital characteristics of binaries systems experiencing symmetric supernova explosions, the sizes of helium stars approaching collapse into a neutron star, and the fate of neutron stars in common envelope phases with helium stars led to our conclusion that the observed double neutron star systems in the galactic disk could not have been formed if the SN explosions forming the pulsar companions were symmetric. Kick velocities imparted to neutron stars at birth are required to explain the observed parameters of DNS systems, even if they have experienced significant orbital evolution due to gravitational wave emission. We find that kicks not only need to exist but in fact their magnitudes must exceed some minimum values. It is only then that the progenitor orbits can be sufficiently wide to accommodate the evolved helium stars, and also produce the short separations observed for the systems. In other words, kicks are necessary because they allow the production of post-SN orbits smaller than those before the explosion, in contrast to symmetric supernovae, which always result in an expansion of the orbit. For the observed double neutron stars in close orbits the minimum kick velocities required are in excess of 200 km/s. We consider this as the most direct evidence so far that such high kicks are indeed imparted to neutron stars in nature. Whatever the physical mechanism responsible for the kick velocities, it must be efficient enough to give rise to kicks up to a few hundreds km/s.

The analysis presented here enable us to set limits on the orbital parameters of the immediate progenitors of the observed DNS systems, as well as, on the

kick velocities imparted to the pulsar companions. However, obtaining the most probable of the parameters within the allowed ranges requires modeling of the evolutionary history of the DNS progenitors up to the formation of the pulsar/helium-star binaries. Here, we use the population synthesis code (Monte Carlo) described in Fryer, Burrows, & Benz (1996) to estimate the most probable kick velocities, and hence progenitor parameters, for the observed systems. The standard DNS formation mechanism (Srinivasan & van den Heuvel 1982) is modeled, including the constraint that the helium stars must be accommodated in their orbits prior to collapse. The formation rate of DNS systems with separations less than $5R_{\odot}$ peaks at 200 km/s ($5 \times 10^{-8} \text{ yr}^{-1}$) and falls off sharply beyond 300 km/s. Although higher kicks are allowed by our analysis, they disrupt most of the binaries and do not contribute significantly to DNS formation. For double neutron star systems with separations $\lesssim 50 R_{\odot}$, the formation rate ($\sim 10^{-6} \text{ yr}^{-1}$) peaks at kicks lower than 100 km/s, and is consistent with the rate inferred observationally (van den Heuvel 1995). These results indicate that kick velocities comparable to the derived lower limits are mostly favored. Consequently, orbital separations and masses of $\sim 4.5 R_{\odot}$ and $\sim 4.5 M_{\odot}$ are favored for the close systems (PSR 1913+16 and 1534+12). Separations of $\sim 50 R_{\odot}$ are more probable for PSR 2303+46 and $\sim 30 R_{\odot}$ for PSR 1518+4904, and the helium star mass is $\sim 3 M_{\odot}$ for both of these systems.

We may use our knowledge of the parameters of DNS progenitors, to calculate the center-of-mass velocities, V_{CM} , acquired by the systems after the explosion (equation 34 in Kalogera 1996) for specific kick magnitudes. Their lowest possible value depends solely on the parameters of that progenitor binary with the lowest orbital relative velocity. For the systems in close orbits (PSR 1913+16 and 1534+12) we find minimum center-of-mass velocities of $\sim 240 \text{ km/s}$

and ~ 230 km/s, respectively. These minimum velocities also correspond to the lower kick magnitudes which, from our population synthesis calculations, are the most probable velocities. Post-SN orbital evolution affects only mildly these minima. For the two wider systems the minimum values of V_{CM} are considerably lower, ~ 50 km/s. Because the pre-SN orbital velocities increase with increasing magnitude of the kick (Figure 4), the center-of-mass velocities tend to increase, as well. Measurements of proper motions of the observed have been reported in the literature the past few years (Taylor 1993; Arzoumanian *et al.* 1993; Nice 1996). The inferred values of transverse velocities are relatively accurate for the two close systems, PSR 1913+16 and 1534+12, 110 ± 25 km/s and 160 ± 10 km/s. For PSR 1518+4904 only an upper limit of 40 km/s can be set, while for PSR 2303+46 there is no significant measurement. We note that no errors in the distance estimates has been taken into account for the inferred values. Moreover, in the theoretical estimates we have neglected any center-of-mass velocities of the pre-SN system as well as the effects of the galactic potential. We should also bear in mind that only transverse velocities are measured and that the number of systems is too low for any statistically significant conclusions to be drawn. Considering all of these caveats, we conclude that comparison of the observationally inferred and theoretically predicted values provide a positive consistency check for our results.

TABLE 1
DOUBLE NEUTRON STAR SYSTEMS

	Units	PSR B1913+16 ^a	PSR B1534+12 ^b	PSR B2303+46 ^c	PSR J1518+4904 ^d	PSR B2127+11C ^e
Orbital Characteristics						
M_{tot}	M_{\odot}	2.82827 ± 0.0004	2.68 ± 0.003	2.53 ± 0.08	2.62 ± 0.07	2.706 ± 0.011
M_p	M_{\odot}	1.442 ± 0.003	1.32 ± 0.03	~ 1.265	~ 1.31	~ 1.35
M_c	M_{\odot}	1.386 ± 0.003	1.36 ± 0.03	~ 1.265	~ 1.31	~ 1.35
e		0.617	0.274	0.658	0.249	0.681
P	sec	27906.98	36351.70	1066136.65	745978.02	28968.36
A	R_{\odot}	2.80	3.28	30.5	24.4	2.83
Pulsar Properties						
P_s	ms	59.030	37.904	1066.372	40.935	30.529
\dot{P}_s	$10^{-18} \text{ s s}^{-1}$	8.626	2.43	569.3	< .04	4.99
τ_c	yr	1.1×10^8	2.5×10^8	3.0×10^7	$> 1.6 \times 10^{10}$	9.7×10^7
B	$10^{10} G$	2	1	80	0.1	1
Accretion and Apsidal Motion						
R_L/R_{MS}		0.31	0.68 – 0.73	3.4	5.7	0.27 – 0.29
R_L/R_{MS}		1.5	3.3 – 3.5	16	27	1.3 – 1.4
ω_{obs}	deg yr ⁻¹	4.23	1.76	0.011	0.0099	4.46
$\dot{\omega}_{\text{tid}}(\text{MS})$	deg yr ⁻¹	$1.2 \times 10^4 - 2.4 \times 10^4$	290 – 810	$1.8 \times 10^{-3} - 3.7 \times 10^{-3}$	$5.4 \times 10^{-4} - 1.1 \times 10^{-3}$	$1.5 \times 10^4 - 4.1 \times 10^4$
$\dot{\omega}_{\text{rot}}(\text{MS})$	deg yr ⁻¹	12 – 24	2.5 – 6.5	$2.0 \times 10^{-3} - 4.0 \times 10^{-3}$	$2.0 \times 10^{-3} - 4.0 \times 10^{-3}$	12 – 27
$\dot{\omega}_{\text{tid}}(\text{He})$	deg yr ⁻¹	53	1.7	1.1×10^{-5}	2.7×10^{-6}	70 – 97
$\dot{\omega}_{\text{rot}}(\text{He})$	deg yr ⁻¹	0.053	0.014	1.2×10^{-5}	1.0×10^{-5}	0.056 – 0.064
Position and Companion Flux						
distance	kpc	~ 5	$\lesssim 0.5$	~ 2.3	~ 0.70	~ 9.8
E(B-V)	mag	~ 1.1	$\lesssim 0.03$	~ 0.3	$\lesssim 0.03$	$\lesssim 0.09$
V (MS star)	mag	~ 20	~ 12	~ 16	~ 13	~ 19
White Dwarf						
Temp/Age	mag					
V (60000 K/10 ⁶ yr)	mag	~ 26	~ 18	~ 22	~ 19	~ 25
V (30000 K/10 ⁷ yr)	mag	~ 27	~ 19	~ 23	~ 20	~ 26
V (17000 K/10 ⁸ yr)	mag	~ 29	~ 21	~ 25	~ 22	~ 28
V (9000 K/10 ⁹ yr)	mag	~ 30	~ 22	~ 26	~ 23	~ 29

^aTaylor & Weisberg 1992

^bWolszczan 1991

^cLyne & Bailes 1990

^dNice, Sayer, & Taylor 1996

^ePrince et al. 1991

TABLE 2
DOUBLE NEUTRON STAR SYSTEMS

	PSR B1913+16	PSR B1534+12	PSR B2303+46	PSR J1518+4904
		Symmetric Explosion		
$A_o (R_\odot)$	1.068	2.373	10.4	18
$M_o (M_\odot)$	3.13	2.37	2.9	~ 2.0
$R_{He} (R_\odot)$	~ 8.7	300	15	~ 320
$R_L/R_{He}(\text{GR})$	$0.055 - 0.17$	$0.0032 - 0.0047$	0.31	0.024
$R_L/R_{He}(\text{ecc})$	$\lesssim 0.13$	$\lesssim 0.21$	$\lesssim 1.3$	$\lesssim 1.6$
		Accretion		
models	$4.2M_\odot - 2.5M_\odot$	$2.0M_\odot - 2.25M_\odot$	$2.5M_\odot$	$2.0M_\odot$
$\dot{M} (M_\odot \text{yr}^{-1})$	$370 - 1.5 \times 10^3$	$0.9 - 250$	2.5	0.11
$\dot{M}_j (M_\odot \text{yr}^{-1})$	160 - 200	0.01 - 75	0.01	10^{-6}
R_B/R_{He}	$0.13 - 2.6 \times 10^{-3}$	$3.8 \times 10^{-3} - 4.5 \times 10^{-3}$	2.5×10^{-2}	2.1×10^{-2}
$T_{BH} (\text{yr})$	$2.7 \times 10^{-3} - 6.5 \times 10^{-4}$	$1.1 - 4.0 \times 10^{-3}$	1.4	8.5
$T_{BH,j} (\text{yr})$	$6.3 \times 10^{-3} - 5.0 \times 10^{-3}$	100 - 0.013	110	1.0×10^6
		Evolution		
models	$3.2M_\odot - 2.9M_\odot$	$2.0M_\odot - 2.2M_\odot$	$3.2M_\odot - 2.9M_\odot$	$2.0M_\odot$
$T_{ev} (\text{yr})$	$3 \times 10^4 - 6 \times 10^4$	$3 \times 10^4 - 9 \times 10^4$	7×10^3	1×10^4
$T_{CE} (\text{yr})$	$10 - 1 \times 10^3$	9×10^3	1×10^3	9×10^3

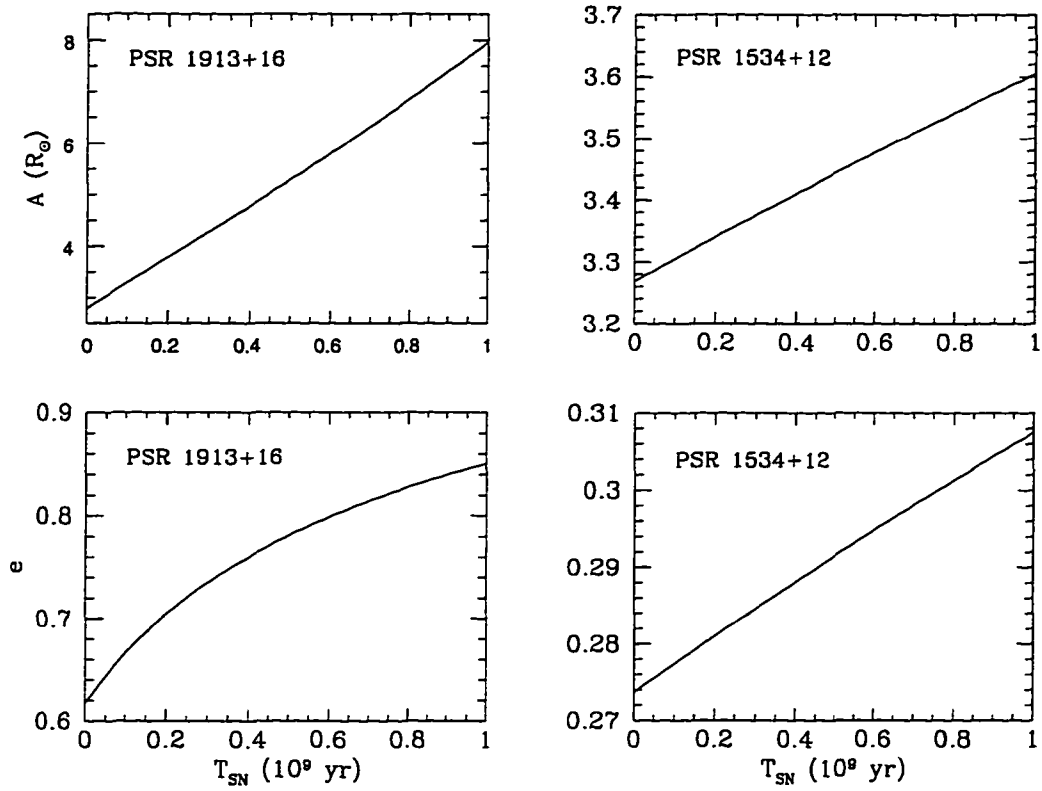


Figure 3.1 Post-supernova orbital separation, A , and eccentricity, e , as a function of the time, T_{SN} , elapsed from the supernova explosion, for PSR 1913+16 and PSR 1534+12.

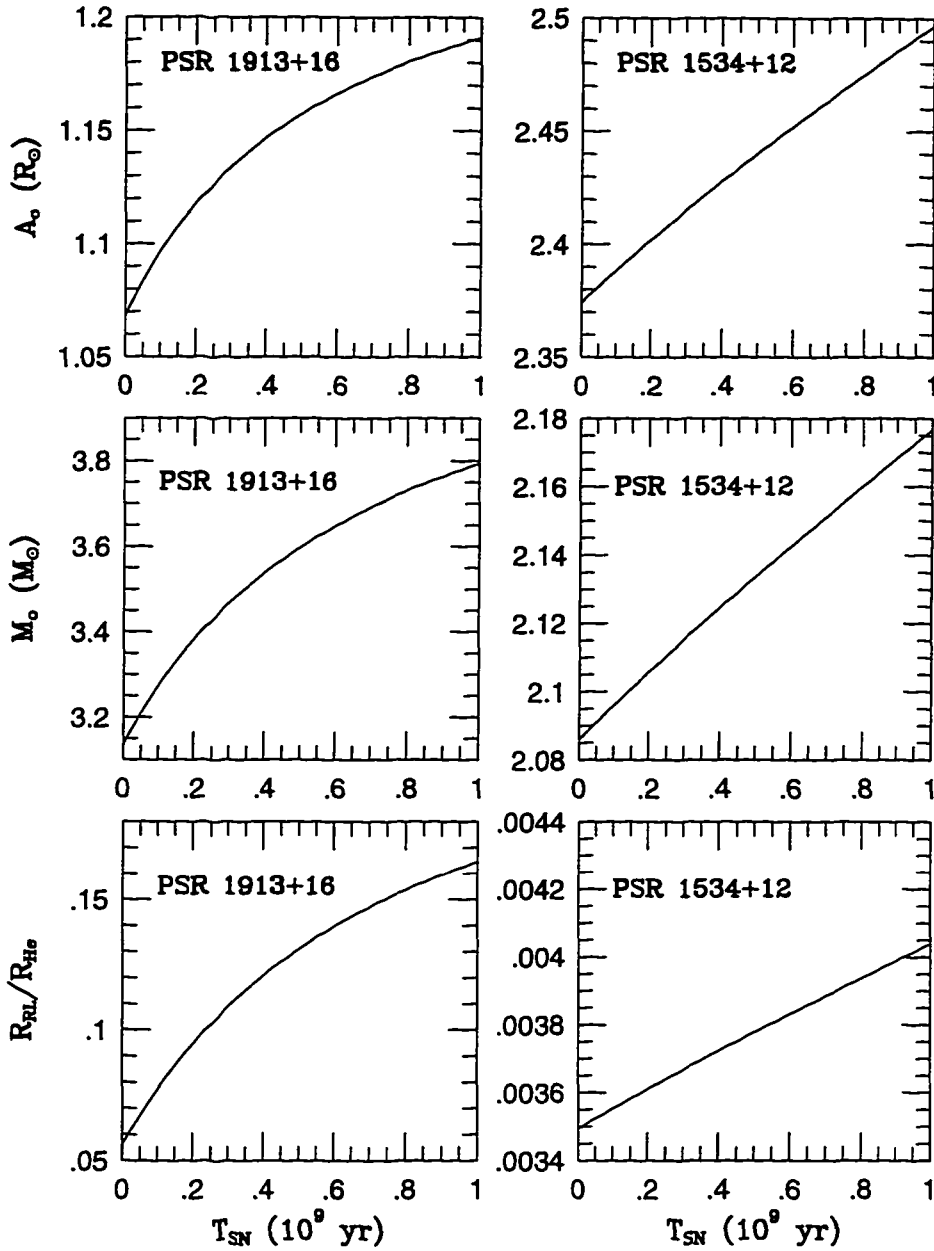


Figure 3.2 Pre-supernova orbital separation, A_o , mass of the exploding (helium) star, M_o , and ratio, R_L/R_{He} , of the Roche lobe radius to the maximum radius acquired by a helium star prior to the supernova, as a function of the time, T_{SN} , elapsed from the explosion. Quantities are plotted for PSR 1913+16 and PSR 1534+12 and under the assumptions of circular pre-supernova orbits and symmetric supernovae.

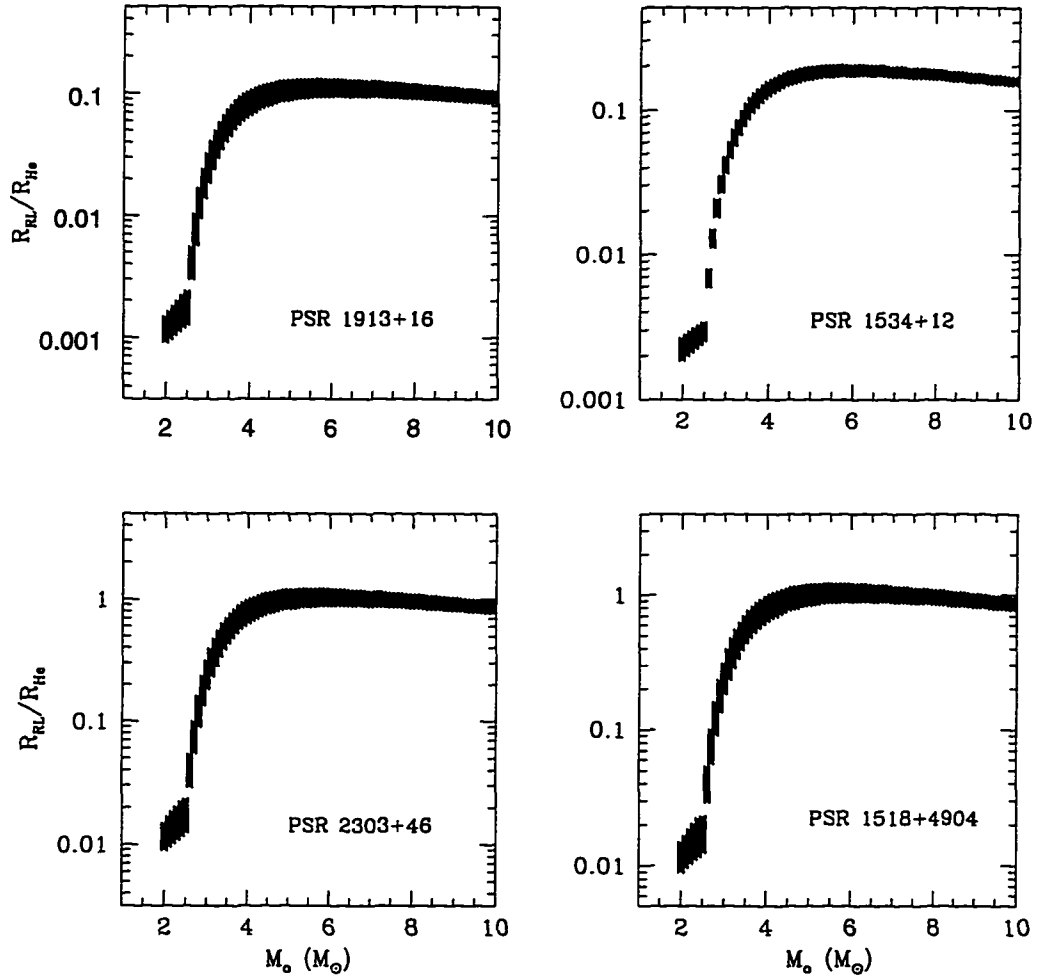


Figure 3.3 Ratio, R_L/R_{He} , of the Roche lobe radius to the maximum radius acquired by a helium star prior to the supernova, as a function of the mass, M_0 , of the helium star, for a complete range of pre-supernova eccentricities. Plots are shown for PSR 1913+16 and PSR 1534+12 and for symmetric supernovae. A minimum helium star mass for neutron star formation of $2 M_\odot$ has been assumed.

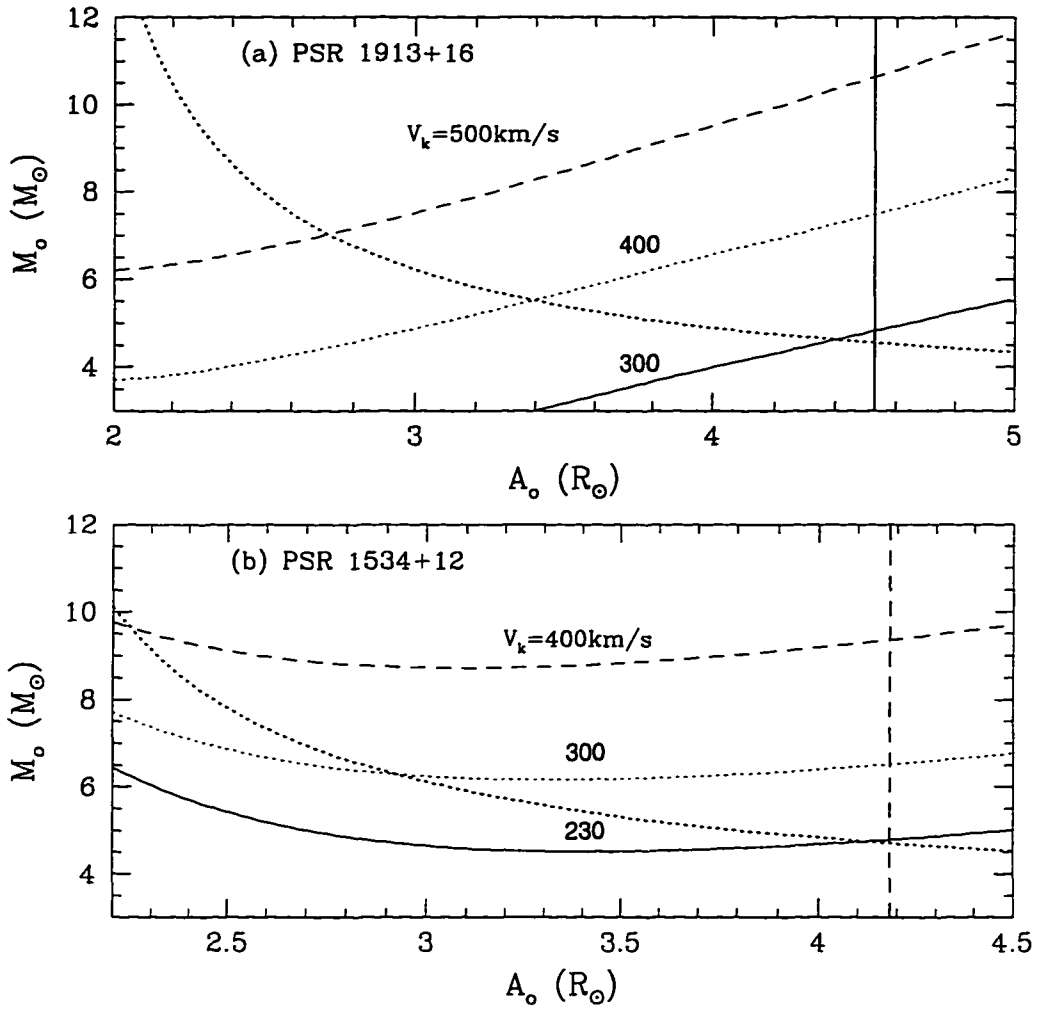


Figure 3.4 Limits on the pre-supernova orbital separation, A_o , and mass of the helium star, M_o for (a) PSR 1913+16 and (b) PSR 1534+12, and for three different magnitudes of the kick velocity, V_k . The thick dashed vertical line corresponds to the maximum separation set by the geometrical constraint; the thick dotted line corresponds to the minimum helium-star mass that can be accommodated in the orbit; the thin lines correspond to the maximum possible pre-supernova orbital angular momentum and their position depends on the kick magnitude. Limits are calculated for circular pre-supernova orbits and neglecting any post-supernova orbital evolution.

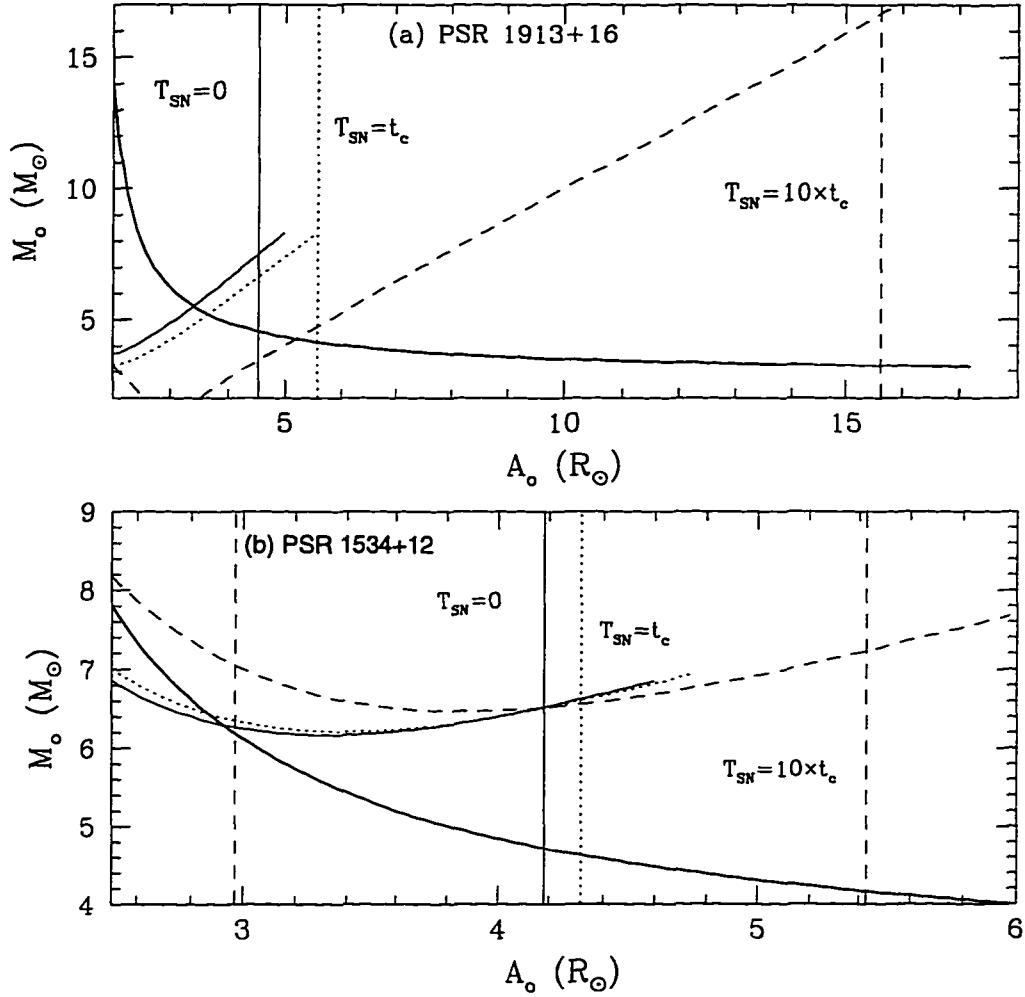


Figure 3.5 Limits on the pre-supernova orbital separation, A_o , and mass of the helium star, M_o for (a) PSR 1913+16 and (b) PSR 1534+12, and for three different values of the time, T_{SN} elapsed from the supernova in units of the pulsar characteristic ages, τ_c . The thick solid line corresponds to the minimum helium-star mass that can be accommodated in the orbit; the thin lines correspond to the geometrical (vertical) and the angular momentum constraints, and depend on the value of T_{SN} . Limits are calculated for circular pre-supernova orbits and for kick velocity magnitudes (a) $V_k = 400$ km/s and (b) $V_k = 300$ km/s.

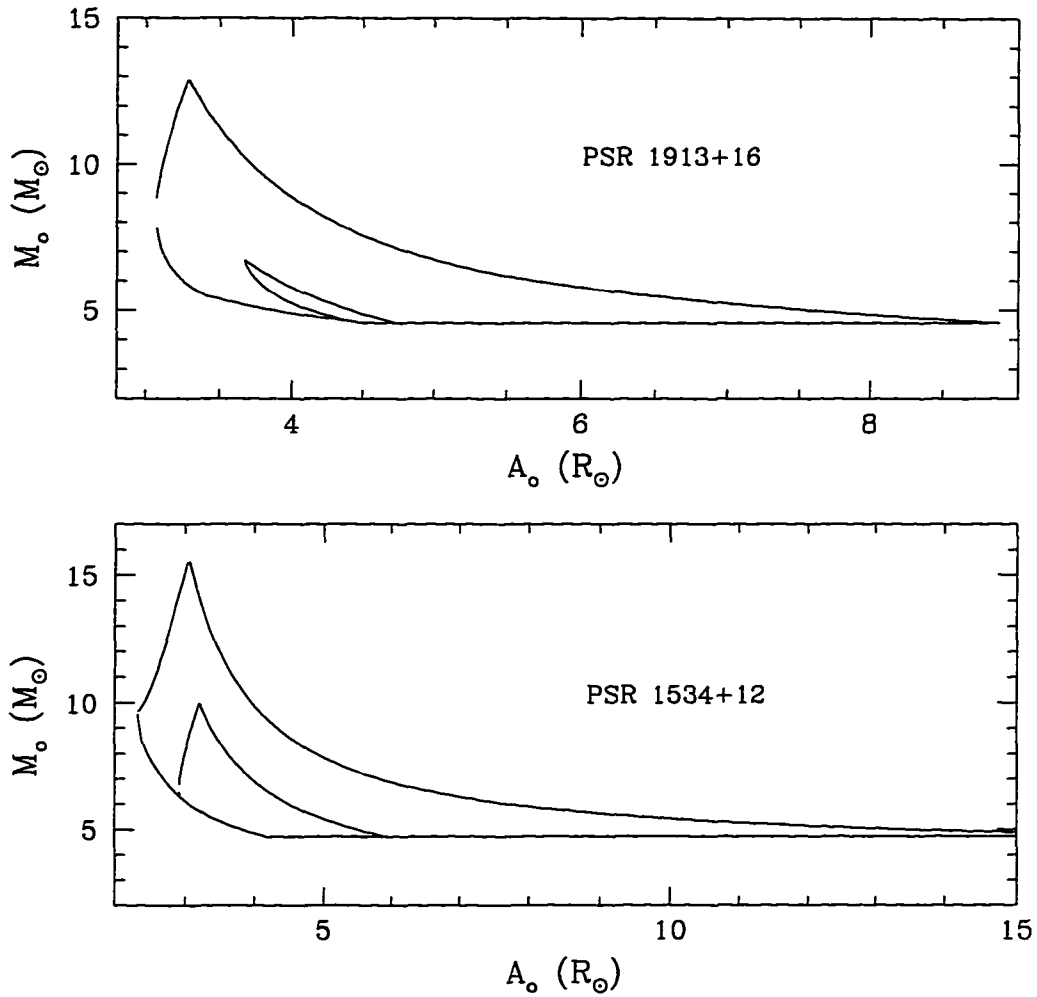


Figure 3.6 Limits on the pre-supernova orbital separation, A_o , and mass of the helium star, M_o for (a) PSR 1913+16 and (b) PSR 1534+12, for eccentric pre-supernova orbits and for different values of the magnitude of the kick velocity, V_k . Post supernova orbital evolution has been neglected.

CHAPTER 4

POPULATION SYNTHESSES FOR NEUTRON STAR SYSTEMS WITH INTRINSIC KICKS

Brief Summary

We use a Monte-Carlo binary synthesis code to model the formation and evolution of neutron star systems including high-mass X-ray binaries, low-mass X-ray binaries, double neutron star systems and radio pulsars. Our focus is on the signature imprinted on such systems due to natal or post-natal kicks to neutron stars over and above that imparted by orbital motions. The code incorporates the effect of the galactic potential on the velocities of these systems. A comparison between our models and the observations leads us to infer mean natal kicks $\gtrsim 400 - 500 \text{ km s}^{-1}$. Moreover, to be consistent with all the data, we derive that the kick distribution is bimodal with one peak near 0 km s^{-1} and the other above 600 km s^{-1} .

4.1. Introduction

Support for the claim that many neutron stars have high velocities continues to mount. Probably the most compelling evidence lies in the velocities, and to a lesser extent, the scale height off the galactic plane of the observed radio pulsar population. With the most recent proper motion observations and the newly-corrected distance determinations of Taylor & Cordes (1993), Lyne & Lorimer (1994) have derived a mean pulsar velocity of 450 km s^{-1} , an increase of almost a factor of 2 over previous estimates. Velocities as high as $\sim 800 \text{ km s}^{-1}$ have been inferred by associating pulsars with supernova remnants (Caraveo 1993 and Frail, Goss & Whiteoak 1994) and from observations of the bow shocks produced by neutron stars as they plow through the interstellar medium (Cordes, Romani, & Lundgren 1993). Neutron star kicks have been invoked to explain characteristics of O/B runaway stars (Blaauw 1961), double neutron star systems (DNS) such as PSR B1913+16 and PSR B1534+12 (Flannery & van den Heuvel 1975, Burrows & Woosley 1986, Yamaoka, Shigeyama, & Nomoto 1993), the angle between the spin and orbit axes of recycled pulsar systems (Kaspi et al. 1996, Wasserman, Cordes, & Chernoff 1996), galactic gamma-ray bursters (Colgate & Leonard 1994, Lamb 1995), and highly eccentric Be/NS binaries (van den Heuvel & Rappaport 1986).

Iben & Tutukov (1996) have claimed that these high velocities can be explained using binary effects alone. By considering a $16M_{\odot}$ helium star with a neutron star companion, they have shown that NS velocities as high as 1000 km s^{-1} can be obtained. Thus, the existence of a single high-velocity neutron star does not require neutron star kicks. However, we show in this paper that neutron-star kicks are required to explain the transverse-velocity *distribution* of pulsars. We present the results of a series of Monte-Carlo simulations of massive star systems through

binary evolution and compare our simulated pulsar transverse velocities with the pulsar sample, including the effects of the galactic potential. This technique is similar to that of Dewey & Cordes (1987), who, however, were limited to the old pulsar velocity data. Even with this old data set, Dewey & Cordes (1987) found that $100 - 150 \text{ km s}^{-1}$ kick velocities were required to explain the observed pulsar proper motions.

The radio pulsar velocity data alone provide evidence for kicks, but they are unable to restrict the actual kick distribution itself. We show that Maxwellian distributions, flat distributions, even a delta function kick distribution, will match the observed radio pulsar data with varying degrees of success. To learn more about the kick distribution, we expand our study to include additional neutron star populations: Low-Mass X-ray Binaries (LMXBs), High-Mass X-ray Binaries (HMXBs), DNSs, and globular cluster neutron stars. Employing the constraints of all these systems, we can rule out many of the kick distributions in the literature. The most probable distribution is double-peaked, with one peak at $\sim 650 \text{ km s}^{-1}$ and the other near 0 km s^{-1} . This bimodal kick distribution is a challenge to any theory of kick origins.

In §4.2, we discuss the methods we employ for the simulations of each massive binary population and our comparison with the observations. In §4.3, we describe our model of the galactic potential and our approach to calculating neutron star retention fractions in globular clusters. Section 4.4 discusses the various uncertainties in binary population synthesis, along with results from the individual parameter studies. Sections 4.2-4.4 are devoted entirely to a description of our Monte-Carlo simulations and a careful analysis of the uncertainties and difficulties involved in these population synthesis calculations. In §4.5, we discuss the results

and implications of these new simulations and the constraints they place on the neutron star kick velocity distribution.

4.2. Neutron Star Populations

We use not only the radio pulsar proper motion data, but also the estimated formation rates of LMXBs, HMXBs and DNSs, to constrain the neutron star kick distribution. The birthrate (BR) for the binary systems is given by:

$$BR = \frac{\text{Number of Systems}}{SN} \times \frac{SN}{yr} \times f_{binary}. \quad (67)$$

Using our Monte Carlo code, we simulate 10^6 binary systems and calculate the number of each type of system produced and the total number of supernovae (SN), from which we derive the first term in equation (67). By assuming a supernova rate (SN/yr) and the fraction of systems in binaries f_{binary} , we calculate the birthrate of each type of system.

The birthrate itself can not easily be compared with the observations and, hence, we resort to a variety of indirect techniques to constrain the models. Since we use a different technique for each system, we discuss each system separately. When we encounter any uncertainty in a calculation, we choose the conservative bound. Thus, our simulated birthrates are always upper limits.

There are a number of ways to determine the supernova rate. Kalogera & Webbink (1996b, KW96) use the star formation rate along with an initial mass function (IMF) and obtain a supernova rate $\sim 7.7 \times 10^{-3} \text{ SN y}^{-1}$. Iben, Tutukov, & Yungelson (1996a, 1996b) also use the star formation rate and estimate a similar rate ($\sim 9.1 \times 10^{-3} \text{ SN y}^{-1}$). Dalton & Sarazin (1995, DS95) use the galactic Lyman continuum flux (which is dominated by massive stars) along with an IMF with

an upper mass cutoff and derive $\sim 7 \times 10^{-3} \text{ SN y}^{-1}$. However, galactic SN rates themselves are typically estimated to be in the range $10^{-2} - 3 \times 10^{-2} \text{ SN y}^{-1}$ (Tammann, Loeffler, & Schroeder 1994). We assume a supernova rate of $10^{-2} \text{ SN y}^{-1}$ for our simulations. The binary fraction depends upon the mass ratio of binaries that we adopt. We discuss the various mass ratios and their resultant binary fractions in §4.4.

4.2.1. Low-Mass X-ray Binaries

The X-ray emission of an LMXB is powered by Roche-lobe overflow from its low-mass companion. Although a necessary condition in LMXB creation is that the low-mass companion remain bound to the neutron star after the supernova explosion, this condition is not sufficient. The bound system must evolve to a phase in which stable Roche-lobe overflow occurs. For our simulations, we use the technique of KW96. We evolve the orbital separation by both gravitational radiation and magnetic braking. Following the work of Kalogera & Webbink (1996a), we restrict our sample to those systems that develop stable sub-Eddington or super-Eddington accretion. Since systems with super-Eddington accretion may not be observed as LMXBs and since this accretion occur an order-of-magnitude more often than sub-Eddington accretion, the inclusion of of super-Eddington systems may overestimate by a factor of 10.

The astute reader may worry that our simulations do not consider all of the possible formation scenarios for LMXBs and, hence, that we are underestimating their formation. Our simulations include the standard formation scenario which uses a common-envelope phase to tighten the pre-SN orbit. In addition, we include scenarios which use the kick to reduce the orbital separation after the supernova without the aid of a common-envelope phase (Kalogera 1996). We do

not include any scenarios involving a Thorne-Żytkow phase (Eggleton & Verbunt 1986). Models of common-envelope evolution (Chevalier 1993, Brown 1995, Fryer, Benz, & Herant 1996) show that the neutron star would collapse into a black hole before it could spiral into the core of its companion to form a Thorne-Żytkow object. Similarly, we ignore the accretion-induced collapse (AIC) route to LMXBs. Simulations by Woosley & Baron (1992) limit the total rate of AICs to 10^{-4} y^{-1} to avoid nucleosynthetic contamination by their ejecta. This rate is comparable to the rate predicted by Iben, Tutukov, & Yungelson (1996b), who conclude that AICs make up no more than a few percent of the LMXB population. Recent simulations of AICs by Fryer et al. (1996) suggest that the upper limit set by Woosley & Baron is an order-of-magnitude lower still. Hence, it is unlikely that AICs contribute to the LMXB population.

With this information, we can calculate the number of LMXBs formed per supernova (the first term in equation 67). To compare with the observations, we would like to multiply our birthrate with the lifetime of our LMXBs to derive the number of galactic LMXBs. However, the lifetime of LMXBs is very difficult to estimate. Instead, we calculate an upper limit to the X-ray flux of these systems collectively by assuming that the low-mass companion is completely consumed by the neutron star and that all of the energy from mass accretion is converted into X-ray photons. This galactic luminosity is:

$$L_X^{tot} = \frac{GM_{co}M_{NS}}{r_{NS}} \times BR, \quad (68)$$

where G is the gravitational constant and M_{NS} and r_{NS} are the mass and the radius of the neutron star, respectively. BR is the LMXB birthrate calculated in our Monte-Carlo simulations (eq. 67). KW96 estimate the X-ray flux from galactic LMXBs to be $L_{X,tot} = 1.7 \pm 0.1 \times 10^{39} \text{ erg s}^{-1}$. In §4.5, we make use of the fact

that we have overestimated both the LMXB formation rate and the LMXB X-ray emission. If, for a given kick distribution, our calculated upper limit falls below the observed value, that kick distribution is excluded.

4.2.2. High-Mass X-ray Binaries

HMXBs are thought to be powered by material from the massive companion's wind. For these systems, we use the same technique as DS95. Using the models of Schaller et al. (1992), we determine the high-mass companion's radius, its mass loss rate, etc., from which we can estimate the mass accretion rate onto the neutron star as a function of time. Then

$$L_X^{tot} = \frac{G\dot{M}_{acc}M_{NS}}{r_{NS}} \quad (69)$$

where \dot{M}_{acc} is determined in the same manner as in DS95. DS95 introduce an efficiency parameter for the conversion of potential energy into X-ray photons, but we will assume, as we do in the case of LMXBs, that the conversion is 100% when calculating an upper limit to the formation rate of HMXBs.

Using the Schaller et al. (1992) models, we not only recover the X-ray luminosity, but the HMXB lifetime. For HMXBs, we can combine our estimated birthrate with this lifetime to determine a total HMXB population. We compare our brightest sources with the bright galactic sources. Meurs & van den Heuvel (1989) estimate the number of HMXBs with $L_X > 10^{36} \text{ erg s}^{-1}$ to be 55 ± 27 . We will require the upper limit from our simulations to give $N(L_X > 10^{36}) \gtrsim 28$. As in the case for LMXBs, if our simulated upper limit falls below the lower limit in the observations, we conclude that the kick distribution does not fit the data.

4.2.3. Double Neutron Star Systems

We calculate the birthrate of DNSs by including all bound double neutron star systems. This simple prescription is suggested by the fact that there are many opportunities during the evolution of these systems to tighten their orbits and recycle their pulsars. Our inclusion of all bound DNS systems gives us a reasonably solid upper limit. Although the birthrate of close DNS systems has been estimated to be $\sim 10^{-6}\text{y}^{-1}$, previous population syntheses have predicted almost 100 times more wide-orbit DNSs (van den Heuvel 1995). These systems are not observed, both because they are much more difficult to detect as binaries and because the pulsar in the wide binary systems is not recycled, and, hence, has a much shorter lifetime. We require only that our total number of bound DNS systems be greater than the $\sim 10^{-6}\text{y}^{-1}$ predicted by van den Heuvel (1995).

Alternate scenarios for double neutron stars do exist. In globular clusters, a viable formation scenario for DNSs such as PSR 2127+11C involves stellar collisions with binaries in cluster cores. This scenario is not a likely formation mechanism for the galactic disk DNSs. Brown (1995) has suggested an alternate formation scenario which includes a double helium star phase. This mechanism requires that the binary components have nearly equal masses. Our code models these systems, but for the mass-ratio distributions we use (see §4.4), this mechanism provides a negligible contribution to our DNS formation rate.

4.2.4. Radio Pulsars

Rather than calculate the birthrate of radio pulsars, we compare our simulated pulsar velocity distribution with the observations. In our simulations, we assume that each neutron star has an early pulsar phase. We extract from our simulations

the young pulsar population ($t_{age} < 3 \times 10^6$ y) within 5 kpc of the sun. Since our results depend sensitively upon the velocity distribution of the radio pulsar population, it is important to understand the uncertainties and biases connected with the pulsar observations.

Our pulsar sample is taken from the proper motion data of Taylor, Manchester, & Lyne (1993) with distances determined using the new electron density model of Taylor & Cordes (1993). For some pulsars, their new distances are different from their old ones by over a factor of two. Alternate distance estimation techniques provide some support for the Taylor & Cordes distances, but there exist specific cases such as PSR J0738-4042 where the preferred distance is 5 times smaller than that predicted by the electron density model (Johnston et al. 1996). The distance estimated by Taylor & Cordes for PSR J0738-4042 was quite high (> 11 kpc). By restricting our sample to the radio pulsars within 5 kpc of the sun, we hope to avoid the most greivous distance errors. Nonetheless, distance measurement errors are a major concern and we will discuss their effect on our results in §4.5.

Aside from uncertainties in the distance, we must be careful to avoid any biases in our radio pulsar sample. A clear selection bias is that very fast pulsars rapidly leave the galactic disk and can even escape the galactic potential. Slow pulsars, on the other hand, remain bound to the disk and are easily detected. We avoid this bias by limiting our sample to the young radio pulsar population ($t_{age} = P/2\dot{P} < 3 \times 10^6$ y). In addition, by restricting our sample to those pulsars whose ages are less than the typical luminosity decay times (Gunn & Ostriker 1970), we avoid uncertainties in the pulsar age-luminosity relation.

Iben & Tutukov (1996) have suggested that there may be a bias against slow-moving pulsars. The proper motion of a distant, slow-moving pulsar is difficult

to determine. Iben & Tutukov (1996) have claimed that there is a trend in the data supporting this hypothesis (see Figure 4.1). This bias is probably due to errors in the distance measurement and is akin to the luminosity/velocity relation suggested by Tutukov, Chugai, & Yungelson (1984). They noted a clear trend in the data showing that the lowest velocity pulsars had lower luminosities. By realizing that $v_{trans} \propto \text{proper motion} \times \text{distance}$ and that $\text{Luminosity} \propto \text{distance}^2$, Dewey & Cordes (1987) argued that this trend was not a bias, but a consequence of distance errors. This effect is illustrated in Figure 4.2. Distance errors also explain the trend upon which Iben & Tutukov (1996) base their selection bias (see Fig. 4.3). Therefore, we do not make any correction for this effect.

Using Monte-Carlo statistics, we compare our simulated pulsar population to the radio pulsar sample, constrained by our age ($t_{age} < 3 \times 10^6$ y) and distance ($D_{sun} < 5$ kpc) limits. For each kick distribution, we calculate a pulsar velocity distribution. We assume that the simulated pulsar velocity distribution does not fit the radio-pulsar sample only if the probability that the two data sets are not from the same population is 99% or greater.

4.2.5. O/B runaway stars

O/B runaway stars are O or B stars that have somehow been ejected into the galactic halo. One proposed mechanism for O/B runaway stars is ejection during a supernova event (Blaauw 1961). However, this mechanism requires that the O/B runaway stars remain bound to the newly-formed neutron star (Leonard 1990, Leonard & Dewey 1992) and the current observational evidence suggests that these O/B stars are not in close binaries (Gies & Bolton 1986, Sayer, Nice & Kaspi 1996, Philp et al. 1996). An alternate formation mechanism for these objects is dynamical ejection in cluster environments (Leonard 1995) and this mechanism

may well explain most O/B runaway stars. Without knowing the contribution the supernova ejection scenario of O/B runaway star formation, we can not use it to constrain the neutron-star kick distribution.

4.3. Galactic and Globular Cluster Potentials

To obtain the galactic velocity distribution of pulsars, we must place our evolved systems into a galactic or a globular cluster model. This allows us to directly compare the observed pulsar velocities with our simulated velocities. In addition, the escape fraction of neutron stars can be determined, and this is crucial in the case of globular clusters. In this section, we briefly describe our models for the galactic and globular cluster potentials.

4.3.1. Galactic Models

We use the galactic potential of Miyamoto and Nagai (1975)

$$\Phi(R, z) = \frac{GM_{gal}}{(R^2 + [a + (z^2 + b^2)^{1/2}]^2)^{1/2}} \quad (70)$$

where R is the distance from the galactic center in the plane of the disk, z is the distance off the disk and G is the gravitational constant. We use fits by Miyamoto and Nagai for a and b ($a = 7.258\text{kpc}$ and $b = 0.520\text{kpc}$). We normalize M_{gal} by insuring that the rotational velocity of the sun at 8.5 kpc is 225 km s^{-1} .

We distribute our initial binary systems randomly following the O/B disk population (Mihalas & Binney 1968) with a disk scale length of 3.5 kpc and a scale height out of galactic plane of 60 pc with a cutoff at 300 pc. The motion of each system consists of a component from the galactic rotation and a randomly oriented velocity due to binary and kick effects. The galactic rotation itself plays a very

small role in the pulsar velocity distribution ($\lesssim 5\%$ change in the mean transverse pulsar velocities). Including the galactic potential in our calculations leads to significant changes (up to 40%) in the pulsar velocities and can not be ignored.

4.3.2. Globular Clusters

The large population of neutron stars observed in globular clusters requires that a sizable fraction ($> 1 - 10\%$) of their neutron stars remain bound to the cluster (Bhattacharya & van den Heuvel 1991). If they form primarily from core-collapse supernova in situ, then the retention fraction places useful constraints upon the neutron-star kick distribution. An alternate formation mechanism in globular clusters involves the accretion-induced collapse of white dwarfs (e.g. Bailyn & Grindlay 1990). The role AICs play in globular clusters is restricted, just as with LMXBs, by the nucleosynthetic yields predicted by Woosley & Baron (1992) and Fryer et al. (1996). Bailyn & Grindlay (1990) estimate an AIC rate close to 10^{-4} y^{-1} to explain the neutron stars in globular clusters, an order of magnitude higher than the upper limit given by Fryer et al. (1996). It is therefore unlikely that AICs make up more than about 10% of the neutron stars in globular clusters.

However, if neutron stars created through core-collapse explosions do indeed receive large kicks, Drukier (1995) has shown that the retention fraction of these neutron stars can be quite low ($\lesssim 1\%$ of the neutron stars formed). We use the retention fractions versus kick velocity derived by Drukier (1995) to determine the retention fractions of neutron stars (both bound and unbound systems) for all of our kick distributions. Drukier uses both Fokker-Planck and Mitchie-King models to simulate the range of globular cluster retention fractions and includes specific models for NGC 6397 and ω Cen. Our limit for a satisfactory neutron-star kick distribution requires that 1% of the neutron stars formed in NGC 6397 remain

bound. We calculate the entire range of retention fractions derived using the Drukier models.

4.4. Simulations

To determine the birthrate of each neutron star system, we first calculate the number of systems formed per supernova. This is the first term in equation (67). To calculate this term, we have created a Monte-Carlo population synthesis code which chooses from a range of initial conditions and then evolves the binary system through one, and if the secondary mass is sufficiently high, a second explosion. A variety of uncertainties and “free-parameters” (both in the initial conditions and in the subsequent orbital evolution) results in a broad range of birthrates. Therefore, to attack the problem of neutron star kicks, we must explore the realistic range in these rates. In this section, we present the results of an intensive study of the effects of the initial conditions and free parameters on the production rates of LMXBs, HMXBs and DNSs, and on the radio pulsar velocity distribution. The results for the different populations is summarized in Figure 4.4. Although the birthrates for these systems can change by over an order of magnitude as we vary the parameters, if the kick is sufficiently strong, it will dominate the pulsar velocity distribution (Figure 4.5).

4.4.1. Initial Conditions

Four parameters are required to describe a binary system. These are the masses of the two stars, $M_{p,0}$ and $M_{c,0}$, the orbital separation, A_0 , and the initial eccentricity, e_0 . Unfortunately, for massive binaries observational data only moderately constrains these parameters (Habets 1985). Therefore, we are forced to consider a

wide range of initial conditions and to use the neutron star binary production rates themselves to limit the initial conditions.

Mass Ratios and the Initial Mass Function

In our simulations, we determine the initial mass of the primary by sampling an Initial Mass Function (IMF):

$$f(M_{p,0}) \propto M_{p,0}^{-\alpha_{IMF}}. \quad (71)$$

We retain α_{IMF} as a free parameter, but must choose a minimum and a maximum neutron star forming primary mass. Table 4.1 lists the range in results for the various binary populations as a function of α_{IMF} and Table 4.1 gives the range for various limits on the primary mass. The results are shown for several delta-function kicks to give some indication of the strength of these effects at different kick velocities. For most of our simulations, we will use $\alpha_{IMF} = 2.7$ (Scalo 1986) and primary mass limits of 10 and $40M_{\odot}$.

The companion mass distribution is much more difficult to determine. The standard technique prescribes a mass ratio ($q = \frac{M_s}{M_p}$) distribution $P(q)$ by

$$P(q) \propto q^{-\alpha_{MR}}. \quad (72)$$

Observational data for massive star binaries is limited and the effects of selection biases can be extreme. Garmany, Conti, and Massey (1980) claim a strong, bias-corrected, peak at $q = 1$. This led DS95 to choose $\alpha_{MR} = -1$ for the bulk of their simulations. However, by accurately accounting for the selection biases, Hogeveen (1991) found that the Garmany *et al.* results vastly underestimate the number of low-mass companions. Hogeveen favors a mass ratio distribution which

is peaked at low q values with $\alpha_{MR} = 2.7$ which flattens to $\alpha_{MR} = 0$ below some critical $q = q_0$. We use a range of values for α_{MR} and q_0 . In Table 4.1, we see that low values of α_{MR} such as those given by Garmany, Conti, and Massey (1980) lead to a maximum in the DNS production rate. However, the higher value of α_{MR} claimed by Hogeveen (1991) is required to explain the production rate of LMXBs. For most of our simulations we use the high $\alpha_{MR} = 2.7$ value, and vary only the critical value q_0 .

The binary fraction depends upon the choice for the mass ratio distribution parameters. For $\alpha_{MR} = 2.7$ and $q_0 = 0.35$, Hogeveen (1991) gives a binary fraction of 35%. For $\alpha_{MR} = 2.7$ and $q_0 = 0.15$, this value increases to $\sim 65\%$. For the mass ratio distributions derived by the Garmany, Conti, & Massey (1980), we use their calculated binary fraction of 43%.

Orbital Parameters

The distribution of initial eccentricities and separations is also not well known for massive systems. For orbital separation, we assume with Kraicheva et al. (1979) that

$$P(A_0) \propto 1/A_0. \quad (73)$$

We use an inner separation of twice the initial primary radius and a range of outer separations ($10^{4-6} R_\odot$). For eccentricity, we choose two distributions:

$$P(e_0) = \delta(e_0) \quad (74)$$

and

$$P(e_0) = 1. \quad (75)$$

For most of our simulations, we use an outer separation of $10^4 R_\odot$ and the eccentricity distribution from eq. (74). As can be seen in Table 4.1, the choice of these has very little effect upon the neutron star system production rates.

4.4.2. Stellar Models and Binary Evolution

We base our binary evolution calculations on stellar models of single stars, to which we add the effects of binary systems. For stellar radii and masses at different evolutionary periods, we use the fits from KW96 of the massive stellar models of Schaller et al. (1992) and the helium star models of Habets (1985) and Woosley, Langer, & Weaver (1995). Although many aspects of binary evolution are not well understood, the uncertainties have, either rightly or wrongly, been lumped into a few categories. Chief among these are mass transfer, common envelope evolution, and stellar winds.

When the primary star overfills its Roche Lobe, mass transfer begins. For binary systems with mass ratio $q < 0.4$, we assume that there is no stable mass transfer (Webbink 1979; Yungelson & Tutukov 1991; van den Heuvel 1983) and that the system immediately goes into a common envelope. For systems with less extreme mass ratios, we assume, as did DS95, that the mass transfer is initially stable. When the two stars attain equal masses, it is assumed that the mass transfer is no longer stable and a common envelope phase begins.

For stable mass transfer, we follow the prescription of van den Heuvel (1995):

$$\Delta M_s = -\Delta M_p \times (1 - f_{trans}) \quad (76)$$

where ΔM_s , ΔM_p are the change in mass of the secondary and primary star, respectively, and f_{trans} is the fraction of mass lost from the primary which does not accrete onto the secondary and is removed from the system. Table 4.2 depicts

the effects of the variation of f_{trans} between 0.1 and 0.9 and shows that the results depend only slightly on f_{trans} . Therefore, for most of the simulations, we use $f_{trans} = 0.5$. During this phase, the loss of orbital angular momentum is determined by the parameterization of de Loore & De Greve (1992):

$$\frac{\Delta J_{orb}}{J_{orb}} = 1 - \left(1 - \frac{\Delta M_{tot}}{M_{tot}}\right)^\gamma, \quad (77)$$

where J_{orb} and M_{tot} are the pre-overflow values. The value of the parameter γ is poorly constrained. However, as seen in Table 4.2, uncertainty in γ has very little effect on the results. For most of the simulations, we use $\gamma = 2.1$ as estimated by De Greve et al. (1985).

For common envelope evolution, we assume that no mass is gained by the secondary star and that the primary loses its hydrogen envelope. For the ratio of post-common envelope to pre-common envelope binary separation, we use Webbink (1984):

$$\frac{A_f}{A_i} = \frac{\alpha_{CE} r_{L_1} q}{2} \left(\frac{M_{He}}{(M_p - M_{He}) + \frac{1}{2} \alpha_{CE} r_{L_1} M_s} \right), \quad (78)$$

where r_{L_1} is the dimensionless Roche lobe radius of the primary (Eggleton 1983),

$$r_{L_1} = \frac{0.49q^{-2/3}}{0.6q^{-2/3} + \ln(1 + q^{-1/3})}. \quad (79)$$

M_{He} is the mass of the primary's helium core and α_{CE} represents the efficiency with which orbital energy is injected into the common envelope. The fate of close binary systems depends strongly upon this parameter and the current set of simulations (Rasio & Livio 1996, Terman & Taam 1996) provides no definitive value. Indeed, α_{CE} is probably a function of binary system. Iben, Tutukov, & Yungelson (1995a) use a slightly different equation for the post-common to pre-common ratio in which the efficiency parameter α_{CE} has a different meaning. However, as can be seen in Table 4.2, by choosing a higher efficiency, we increase the numbers for all the

binary populations. In our comparison with observation, we use our simulations only to provide upper limits and, to be conservative, we maximize the numbers by choosing a high efficiency ($\alpha_{CE} = 1$).

The theory of neutron stars in common envelopes has transformed in the past 4 years. The high densities of the medium that surrounds the neutron star in the common envelope phase imply that neutrinos, rather than photons, are the dominant coolant. Hence, the accretion rate onto the neutron star is not limited by the Eddington rate (Chevalier 1993,1996; Brown 1995; Fryer et al. 1996). For hydrogen giants, angular momentum (Chevalier 1996) or explosions induced by neutrino heating (Fryer et al. 1996) may restrict the accretion and allow the neutron star to survive this phase. However, in the denser environments of helium star giants, angular momentum and neutrino heating will not be sufficient to prevent black hole formation. In our simulations, we assume that neutron stars survive hydrogen-giant common envelope phases, but not helium-giant common envelope phases.

Mass loss due to stellar winds has a direct effect on stellar mass which, in turn, has a strong effect upon the stellar radius. For both the models of Schaller et al. (1992) and those of Woosley, Langer & Weaver (1995), we parameterize the wind mass loss with

$$\Delta M_{wind} = f_{wind} \times \Delta M_{wind}^{models}, \quad (80)$$

where ΔM_{wind}^{models} is the mass loss from winds predicted by Schaller et al. (1992) which agrees reasonably well with Woosley et al. (1995). In our simulations, $0.0 < f_{wind} < 1.0$ (see Table 4.7), but for most of our simulations f_{wind} is set equal to unity.

4.5. Natal Kick Distributions

Given a kick distribution, we can use our Monte-Carlo code to derive the production rate of LMXBs, HMXBs, and DNSs as well as the pulsar velocity distribution and the globular cluster retention fraction. We stress that for all of the neutron-star populations, we overestimate the production rate. The ratio of our simulated rates to the actual rates may well be greater than ten (see §4.2). Similarly, our globular cluster retention fractions are upper limits. Recall that we normalize the simulated LMXB luminosity with the estimate of KW96 ($L_{X,tot} = 1.7 \times 10^{39}$), the HMXB population by the lower limit of Meurs & van den Heuvel (1989) ($N = 28$ for $L_X > 10^{36} \text{ ergs}^{-1}$), our DNS formation rate by 10^{-6} y^{-1} (van den Heuvel 1995), and our derived retention fraction by 1% for the globular cluster NGC 6397 (Drukier 1995).

In sections 4.5.1 and 4.5.2, we present these ratios for a series of neutron-star kick distributions. Since we are calculating upper limits, we require that all ratios be greater than unity for a successful kick distribution. We use the results from §4.4 to create the best fit within the range of the many free binary-evolution parameters. Unless otherwise noted, we use the standard set of assumptions described in §4.4: $\alpha_{IMF} = 2.7$, mass limits = 10, $40M_{\odot}$, $\alpha_{MR} = 2.7$, $q_0 = 0.35$, $P(A_0) \propto 1/A_0$, $P(e_0) = 1.0$, $f_{trans} = 0.5$, $\gamma = 2.1$, $\alpha_{CE} = 1$, and $f_{wind} = 1.0$.

In §4.5.2, we use the results from our series of δ -function distributions to derive the neutron-star kick distribution which best fits all of the observations. We find that double-peaked kick distributions are best suited to explain both the pulsar velocity data and the binary system formation rates and we study these distributions in more detail. Our results depend most significantly on the distance measurements and we include a brief discussion of the distance errors on our

conclusions.

4.5.1. Maxwellian and Flat Distributions

We ran a series of simulations with Maxwellian kick distributions for a variety of $(v_{rms}^2)^{1/2}$'s. Figure 4.6 summarizes the results of these simulations, using the standard input parameters. Table 4.3 gives the total number of bound neutron stars given the globular cluster models by Drukier (1995), along with the specific results for NGC 6397 and ω Cen. The large kick velocities are required to explain the pulsar velocity distribution. Over 20% of the observed pulsars have transverse velocities greater than 500 km s^{-1} . Even without the effects of the galactic potential, high kick velocities are required to match the observations (Figure 4.7). We ran an alternate simulation using $q_0 = 0.15$ and the mass limits $= 10, 100M_{\odot}$. The lower value for q_0 increases the number of LMXBs, while the higher mass limit allows more very massive stars to contribute to the HMXB and DNS populations. The results are summarized in Figure 4.8 and Table 4.4 and can be directly compared to Figure 4.6 and Table 4.3. For this simulation, we set the binary parameters to maximize the production rate of the neutron-star populations. Nevertheless, we see in Figure 4.8 that there is no acceptable solution. Keeping in mind that all of our ratios are upper limits, we conclude that it is impossible to fit the data with a Maxwellian kick.

Similarly, we ran a series of simulations with flat kick distributions ranging from a magnitude of 0 km s^{-1} to a maximum of V_{max} . For these simulations, we used $q_0 = 0.15$ and the standard parameter set. We see in Figure 4.9 and Table 4.5 that the fit is worse for this kick distribution than for a Maxwellian. Again, we conclude that it is impossible to fit the data with a flat kick distribution.

4.5.2. Delta Function and Bimodal Distributions

We repeated this set of simulations once again for delta function kick distributions. Figure 4.10 shows that we can find a delta function kick distribution that is not inconsistent with the observed pulsar velocity distribution. However, the delta function kick distribution fails to explain our entire data set, especially the globular cluster retention fraction (Table 4.6). Note also in Figure 4.10 that the best fit to the pulsar data gives a kick distribution with a mean near 500-600 km s⁻¹, higher than the mean pulsar velocity calculated by Lyne & Lorimer (1994). The effects of binary evolution and the galactic potential lower the mean neutron-star velocity after its initial kick. As mentioned in §4.3, the galactic potential can alter the pulsar velocities by up to 40% for a given kick distribution.

Next, we use the results of the delta function simulations to determine the optimal kick distribution. We can approximate an arbitrary kick distribution as a weighted sum of delta functions of different kick magnitudes. For this study, we employ as constraints the LMXB, HMXB and DNS populations, as well as the globular cluster retention fractions. We bin the observed pulsar velocity distribution into 5 bins with roughly equal numbers in each bin. We bin the velocity distributions for each delta function simulation in a similar manner.

We calculate the kick distributions which satisfy the four population constraints (requiring that the formation rates exceed the minimum values we calculated in §4.2). For the pulsar velocity bins, we calculate χ^2 residuals. In our calculations, we use the velocity distributions from 7 delta function kicks ranging from 0 to 600 km s⁻¹. The χ^2 residuals do not improve significantly by including velocity distributions from additional delta function kick amplitudes, so we use only these 7 unknowns to explain our 9 constraints: three binary systems, the globular

cluster retention fraction, and five pulsar velocity bins. The solid curve in Figure 4.11 is our best fit to the entire data set. Varying the binning of the pulsar velocities does not change the qualitative and quantitative results noticeably. Notice that the best fit has a roughly double-peaked profile. The high-velocity peak is required to explain the pulsar velocities and the low-velocity peak is required to form the binary systems.

To determine the prevalence of this double-peaked profile, we fill the intervening velocity bins and calculate the resulting residuals. We note that the best-fitting distributions retain the double-peaked profile, but the χ^2 residuals increase dramatically as we force the distribution to fill the middle velocity bins, strongly supporting our claim that the neutron star kick velocity distribution is double-peaked (see Figure 4.11).

To ascertain the effect of the uncertainties in the radio pulsar distances, and hence their velocities, we have repeated these calculations for a set of velocity distributions in which we have artificially scaled down the observed velocities. If the distances are overestimated by some value, then the velocities will also be overestimated by this amount. By scaling down these velocities, we gain insight into the effect of overestimating the distances. Figure 4.12 shows the best-fitting distributions using a range of distance scale factors. The χ^2 residuals normalized by the best-fitting kick distribution are plotted in Figure 4.13. The double peaked profile disappears if we scale down the distances by just 25%.

We validate this double-peaked profile by repeating the process used on the previous kick distributions and verify that a double-peaked profile does indeed satisfy the constraints of the data. For these simulations, we use $q_0 = 0.15$ and the standard parameter set. The first series of simulations uses two δ -function kick

amplitudes. 30% of the pulsars are given a kick of 0 km s^{-1} and the remaining 70% are given a non-zero kick. We range this velocity from $500 - 950 \text{ km s}^{-1}$. Note in Figure 4.14 that over this series of simulations, the kick distributions satisfy our minimum requirements for an allowed kick distribution. A second series of simulations using a kick distribution where 30% of the pulsars are given a kick of 0 km s^{-1} and the remaining 70% have a flat distribution with a mean of 625 km s^{-1} and a range in thickness (Figure 4.15). In both cases, the range of bound neutron stars in globular clusters is stable (28%-30%) corresponding to 2800 and 1000 neutron stars retained in NGC 6397 and $\omega \text{ Cen}$ respectively.

4.6. Conclusions

We have created a Monte-Carlo code which simulates the binary evolution of massive stellar systems and includes HMXB, LMXB, DNS, and radio pulsar phases. This code also follows the motions of these systems in the galactic potential. In addition, we calculate the retention fraction of neutron star systems in globular clusters. For this paper, we restricted our attention to the consequences of intrinsic kicks given to neutron stars, perhaps at birth. First and foremost, a neutron star kick with a mean magnitude above 400 km s^{-1} is required to explain the pulsar velocity data for all the kick distributions we study. By considering the radio pulsar observations alone, we can not constrain the kick distribution, beyond simply requiring a kick. However, if we include the constraints placed upon the kick distribution from the binary populations and the globular cluster retention fraction, we can rule out many of the kick distributions appearing in the literature, including Maxwellian, flat, and δ -function distributions (KW96, Brandt & Podsiadlowski 1995). Distributions which fit all of these constraints do exist, all of which are

double-peaked. To explain the many binary populations, we derive that roughly 30% of the neutron stars receive almost no kick. To explain the radio-pulsar velocity distribution, the remaining $\sim 70\%$ receive a large kick ($600 - 700 \text{ km s}^{-1}$). It is worth noting that Narayan & Ostriker (1990) also required two populations of pulsars.

Of course, there are many caveats to these conclusions. Our results depend sensitively upon the pulsar velocity distribution. If the pulsar distances and hence, the velocities, are systematically lower by 25%, a bimodal distribution is no longer necessary to explain the observations. However, it would require an extensive revision in the velocities to render some sort of neutron star kick unnecessary. Also, we rely heavily on the reasonableness of binary population-synthesis models. Although we have studied the effects of many parameters and have calculated upper limits for all of our production rates, we can not eliminate the possibility that alternate models can explain the data. For instance, Iben & Tutukov (1996) explain the pulsar velocity distribution using the old distance model with no kick whatsoever by allowing only the fastest neutron stars formed in binary evolution to become radio pulsars. Scrutiny of Figure 4.7 reveals that this is not possible unless we remove mass loss from winds. Even so, we require that only the fastest 1% of the neutron stars are observed as pulsars to explain the pulsar velocities from the old distance model. For the new distance model, this percentage becomes prohibitively small. We incorporate the effects of a wide range in binary parameters, so that unless the understanding of binary population synthesis is drastically altered (winds, common envelope evolution, etc.), our basic conclusions still hold. Our results agree with the models of KW96 and DS95.

This bimodal kick distribution has direct implications for a variety of objects

whose evolution may involve a neutron star. To meet the isotropy requirements for gamma-ray bursts using accreting neutron stars in a galactic model, Podsiadlowski, Rees, & Ruderman (1995) require neutron star kicks upwards of $600 - 700 \text{ km s}^{-1}$. Our bimodal kick distribution results in $\sim 70\%$ of the neutron star population with these velocities (Figure 4.16). The bimodal distribution provides a natural break between the low-velocity neutron stars, which burst, and the high-velocity neutron stars which make up the gamma-ray burst population in the galactic model (Leonard & Colgate 1994).

Our kick distribution can also be applied to explain O/B runaway stars. Although O/B runaway stars are not observed to be in close binaries, the observations do not preclude wide binary systems. (Gies & Bolton 1986, Sayer, Nice & Kaspi 1996, Philp et al. 1996). Figure 4.17 plots the distribution of velocities of O/B stars, both bound and unbound, assuming no neutron star kick. The unbound O/B stars are all moving slower than 50 km s^{-1} . The bound systems have significantly higher velocities, but very few O/B stars have velocities greater than 100 km s^{-1} . However, using our bimodal kick distribution, we see that unbound O/B stars can achieve velocities in excess of 200 km s^{-1} .

This bimodal distribution poses an additional problem for kick mechanisms. Not only must a kick mechanism produce neutron stars with velocities greater than 500 km s^{-1} , but the mechanism must be ineffective for a subset of the neutron star population.

Our simulations give us a wealth of data on the characteristics of neutron star systems. The orbital characteristics of the binary systems formed using a variety of kick distributions may also provide insight into this distribution. For instance, wide orbit LMXBs (KW96) and close period DNSs may further constrain the kick

distribution. We have not yet explored variations in the galactic potential and the scale-height distributions of the various neutron star systems. With improved distances and with an increasing sample of radio pulsars, we hope to apply this technique not just to constrain the neutron star kick and binary evolution, but also the galactic potential.

Table 4.1. Parameters: Initial Conditions^a

	LMXB $10^{39} \text{ erg s}^{-1}$	HMXB N with $L_X > 10^{36} \text{ erg s}^{-1}$	DNS Rate (10^{-6} y^{-1})
$V_{kick} = 0 \text{ km s}^{-1}$			
“standard”	2.80	92.7	45.2
$\alpha_{IMF} = 2.1$	2.62	142.4	62.7
$M_{min,max} = 8, 40$	1.36	65.8	26.0
$M_{min,max} = 10, 100$	1.68	47.7	36.1
$\alpha_{MR} = 1.0^b$	0.227	60.9	200.
$\alpha_{MR} = 0.0^b$	2.41	82.6	135.
$\alpha_{MR} = -2.7, q_0 = 0.15^c$	11.1	152.1	26.8
$P(e) = \delta(e)$	2.91	71.2	54.6
$R_{max} = 10^6$	1.26	48.2	73.4
$V_{kick} = 200 \text{ km s}^{-1}$			
“standard”	4.16	40.3	1.15
$\alpha_{IMF} = 2.1$	4.47	53.3	1.42
$M_{min,max} = 8, 40$	2.81	35.5	0.641
$M_{min,max} = 10, 100$	2.56	29.4	0.820
$\alpha_{MR} = 1.0$	0.420	35.1	3.56
$\alpha_{MR} = 0.0$	3.07	42.3	2.49
$\alpha_{MR} = -2.7, q_0 = .15$	19.3	100.5	0.751
$P(e) = \delta(e)$	5.12	32.8	1.11
$R_{max} = 10^6$	1.71	21.8	0.547
$V_{kick} = 400 \text{ km s}^{-1}$			
“standard”	1.68	13.0	0.474
$\alpha_{IMF} = 2.1$	1.98	16.9	0.656
$M_{min,max} = 8, 40$	1.24	10.7	0.289
$M_{min,max} = 10, 100$	0.937	10.5	0.384
$\alpha_{MR} = 1.0$	0.159	10.6	1.85
$\alpha_{MR} = -2.7, q_0 = 0.35$	1.68	13.0	0.474
$\alpha_{MR} = -2.7, q_0 = .15$	6.95	29.8	0.437
$P(e) = \delta(e)$	1.96	10.7	0.491
$R_{max} = 10^6$	0.660	7.51	0.265

^a For these simulations, we use a “standard” set of parameters: $\alpha_{IMF} = 2.7$, mass limits $= 10, 40 M_{\odot}$, $\alpha_{MR} = 2.7$, $q_0 = 0.35$, $P(A_0) \propto 1/A_0$, $P(e_0) = 1.0$, $f_{trans} = 0.5$, $\gamma = 2.1$, $\alpha_{CE} = 1$, and $f_{wind} = 1.0$. We have combined the simulations with a SN rate $= 0.01 \text{ y}^{-1}$ and a binary fraction determined by the choice of mass ratio (unless otherwise stated, we use 0.35). We use the technique in §4.2 to determine each population.

^b For $\alpha_{MR} = 1.0, 0.0$, we assume a binary fraction of 0.43.

^c For $\alpha_{MR} = 1.0, 0.0$, we assume a binary fraction of 0.65.

Table 4.2. Parameters: Orbital^a

	LMXB $10^{39} \text{ erg s}^{-1}$	HMXB N with $L_X > 10^{36} \text{ erg s}^{-1}$	DNS Rate (10^{-6} y^{-1})
$V_{kick} = 0 \text{ km s}^{-1}$			
“standard”	2.80	92.7	45.2
$f_{trans} = 0.1$	2.47	60.3	45.0
$f_{trans} = 0.9$	2.39	61.9	36.0
$\alpha_{CE} = 0.2$	$\lesssim 0.028$	4.82	45.2
$\alpha_{CE} = 2.0$	4.94	181.5	45.3
$f_{wind} = 0$	1.75	89.7	39.2
$\gamma = 1.5$	2.48	238.2	36.3
$V_{kick} = 200 \text{ km s}^{-1}$			
“standard”	4.16	40.3	1.15
$f_{trans} = 0.1$	4.06	23.3	2.00
$f_{trans} = 0.9$	4.43	32.0	0.955
$\alpha_{CE} = 0.2$	$\lesssim 0.028$	2.28	0.0232
$\alpha_{CE} = 2.0$	11.4	71.7	2.13
$f_{wind} = 0$	24.2	65.0	6.01
$\gamma = 1.5$	4.71	85.9	1.38
$V_{kick} = 400 \text{ km s}^{-1}$			
“standard”	1.68	13.0	0.474
$f_{trans} = 0.1$	1.54	6.94	0.854
$f_{trans} = 0.9$	1.71	9.93	0.513
$\alpha_{CE} = 0.2$	$\lesssim 0.028$	0.839	0.00664
$\alpha_{CE} = 2.0$	3.7	20.4	0.927
$f_{wind} = 0$	13.3	21.3	2.43
$\gamma = 1.5$	1.45	29.3	0.577

^aFor these simulations, we use a “standard” set of parameters: $\alpha_{IMF} = 2.7$, mass limits = $10, 40 M_{\odot}$, $\alpha_{MR} = 2.7$, $q_0 = 0.35$, $P(A_0) \propto 1/A_0$, $P(e_0) = 1.0$, $f_{trans} = 0.5$, $\gamma = 2.1$, $\alpha_{CE} = 1$, and $f_{wind} = 1.0$. We have combined the simulations with a SN rate = 0.01 y^{-1} and a binary fraction determined by the choice of mass ratio (unless otherwise stated, we use 0.35). We use the technique in §4.2 to determine each population.

Table 4.3. NS Retention: Maxwellian Kick Distribution^a

$(v_{rms}^2)^{1/2}$ (km s ⁻¹)	Range in RF ^b	RF	NS retained NGC6397	RF	NS retained ω Cen
0.0	91.6 – 99.9%	98%	9.5×10^3	99.1%	3.5×10^3
50.0	4.71 – 49.0%	15.4%	1.5×10^3	29.2%	1.0×10^3
100.0	1.91 – 38.3%	5.30%	5.1×10^2	11.1%	3.9×10^2
150.0	1.19 – 37.5%	2.95%	2.9×10^2	5.83%	2.0×10^2
200.0	0.88 – 18.9%	2.06%	2.0×10^2	3.88%	1.4×10^2
250.0	0.70 – 13.6%	1.60%	1.6×10^2	2.89%	1.0×10^2
300.0	0.57 – 10.2%	1.27%	1.2×10^2	2.26%	79
350.0	0.49 – 8.1%	1.08%	1.0×10^2	1.90%	67
400.0	0.42 – 6.6%	0.93%	90	1.63%	57
450.0	0.38 – 5.5%	0.83%	81	1.42%	49
500.0	0.34 – 4.7%	0.74%	72	1.28%	46
550.0	0.31 – 4.1%	0.66%	64	1.12%	37
600.0	0.29 – 3.6%	0.61%	59	1.02%	35

^aStandard Parameters: $\alpha_{IMF} = 2.7$, mass limits = 10, 40 M_{\odot} , $\alpha_{MR} = 2.7$, $q_0 = 0.35$, $P(A_0) \propto 1/A_0$, $P(e_0) = 1.0$, $f_{trans} = 0.5$, $\gamma = 2.1$, $\alpha_{CE} = 1$, and $f_{wind} = 1.0$.

^bThe range in retention fractions (RF) is determined using the Fokker-Planck models of Drukier (1995).

Table 4.4. NS Retention: Maxwellian Kick Distribution^a

$(v_{rms}^2)^{1/2}$ (km s ⁻¹)	Range in RF	RF	NS retained NGC6397	RF	NS retained ω Cen
0.0	89.0 – 99.7%	95%	9.2×10^3	97%	3.4×10^3
50.0	3.96 – 70.4%	18.4%	1.8×10^3	39.6%	1.4×10^3
100.0	1.25 – 54.7%	4.8%	4.7×10^2	12.7%	4.4×10^2
150.0	0.70 – 37.5%	2.25%	2.2×10^2	5.65%	2.0×10^2
200.0	0.50 – 25.0%	1.41%	1.4×10^2	3.26%	1.2×10^2
250.0	0.41 – 17.0%	1.04%	1.0×10^2	2.21%	77
300.0	0.31 – 12.1%	0.77%	75	1.59%	56
350.0	0.28 – 8.9%	0.67%	65	1.3%	46
400.0	0.23 – 6.9%	0.55%	53	1.1%	37
450.0	0.21 – 5.4%	0.47%	46	0.89%	31
500.0	0.19 – 4.4%	0.44%	43	0.80%	28
550.0	0.18 – 3.7%	0.39%	38	0.69%	24
600.0	0.17 – 2.4%	0.34%	33	0.61%	21

^asame as table 3, $q_0 = 0.15$.

Table 4.5. NS Retention: Flat Kick Distribution^a

<i>MeanVelocity</i> (km s ⁻¹)	Range in RF ^b	RF	NS retained NGC6397	RF	NS retained ω Cen
50.0	9.44 – 69.9%	20.1%	1.9×10^3	33.3%	1.2×10^3
150.0	3.13 – 32.1%	6.66%	646	11.0%	385
200.0	2.35 – 24.1%	5.00%	485	8.28%	290
250.0	1.88 – 19.2%	3.99%	387	6.62%	232
300.0	1.56 – 16.0%	3.33%	323	5.52%	193
350.0	1.34 – 13.7%	2.85%	276	4.73%	166

^aParameters: $\alpha_{IMF} = 2.7$, mass limits = 10, 40 M_{\odot} , $\alpha_{MR} = 2.7$, $q_0 = 0.15$, $P(A_0) \propto 1/A_0$, $P(e_0) = \delta(e_0)$, $f_{trans} = 0.5$, $\gamma = 2.1$, $\alpha_{CE} = 1$, and $f_{wind} = 1.0$.

^bThe range in retention fractions (RF) is determined using the Fokker-Planck models of Drukier (1995).

Table 4.6. NS Retention: δ -Function Kick Distribution^a

<i>Velocity</i> (km s ⁻¹)	Range in RF ^b	RF	NS retained NGC6397	RF	NS retained ω Cen
0.0	89.5 – 99.9%	97.1%	9.4×10^3	98.7%	3.5×10^3
50.0	0.19 – 96.8%	3.62%	3.5×10^2	42.5%	1.5×10^3
100.0	.011 – 67.3%	0.077%	7	0.398%	13.9
150.0	4.2×10^{-3} – 36.6%	0.033%	3	0.127%	4
200.0	2.8×10^{-3} – 11.8%	0.028%	3	0.078%	3
250.0	1.2×10^{-3} – 1.39%	0.016%	2	0.045%	2
300.0	5.1×10^{-4} – 0.43%	$7.6 \times 10^{-3}\%$	1	0.025%	1
350.0	2.2×10^{-5} – 0.30%	$5.5 \times 10^{-3}\%$	1	0.021%	1
400.0	1.7×10^{-6} – 0.21%	$2.1 \times 10^{-3}\%$	0	0.011%	0
450.0	0.0 – 0.16%	$1.0 \times 10^{-3}\%$	0	$7.9 \times 10^{-3}\%$	0
500.0	0.0 – 0.11%	$7.1 \times 10^{-4}\%$	0	$4.7 \times 10^{-3}\%$	0
550.0	0.0 – 0.080%	$1.7 \times 10^{-4}\%$	0	$2.3 \times 10^{-3}\%$	0
600.0	0.0 – 0.062%	$7.9 \times 10^{-5}\%$	0	$1.4 \times 10^{-3}\%$	0
650.0	0.0 – 0.023%	$5.1 \times 10^{-6}\%$	0	$2.5 \times 10^{-4}\%$	0

^aStandard Parameters: $\alpha_{IMF} = 2.7$, mass limits = 10, $40M_{\odot}$, $\alpha_{MR} = 2.7$, $q_0 = 0.35$, $P(A_0) \propto 1/A_0$, $P(e_0) = 1.0$, $f_{trans} = 0.5$, $\gamma = 2.1$, $\alpha_{CE} = 1$, and $f_{wind} = 1.0$.

^bThe range in retention fractions (RF) is determined using the Fokker-Planck models of Drukier (1995).

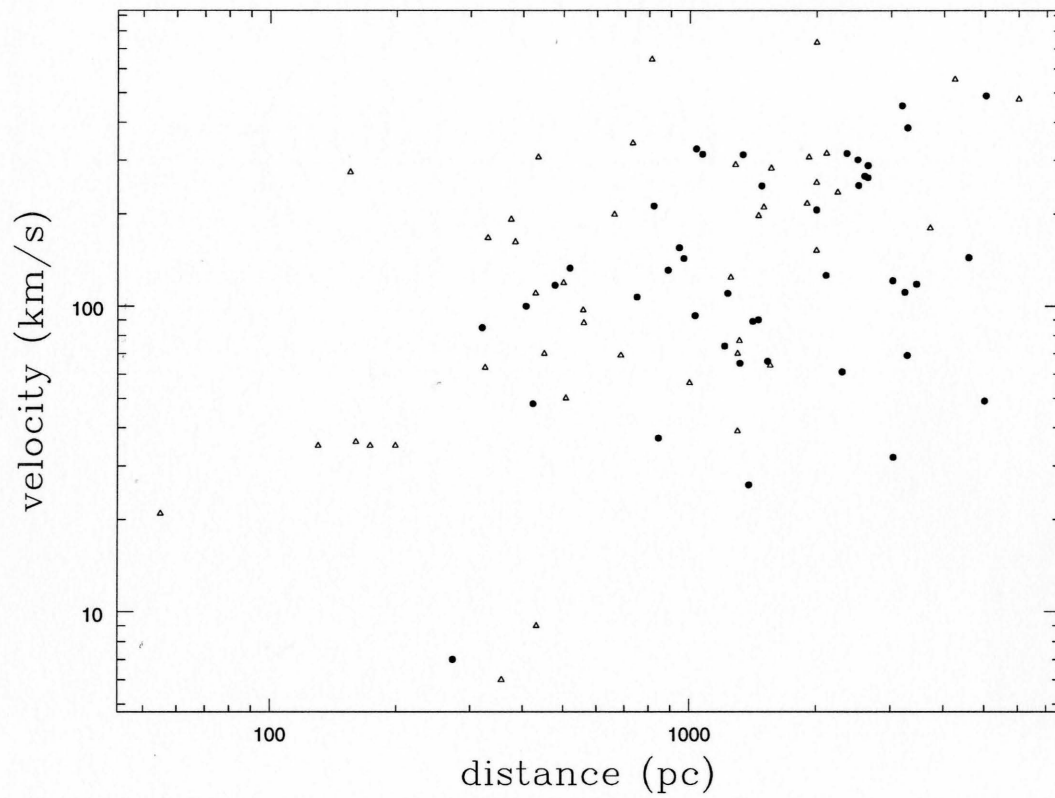


Figure 4.1 The observed transverse velocities of radio pulsars versus their distances D from the Sun (Harrison et al. 1993). The open triangles denote the 44 pulsars with proper motions determined by Harrison et al. and the filled hexagons are the 43 additional pulsars with proper motions calculated by other techniques.

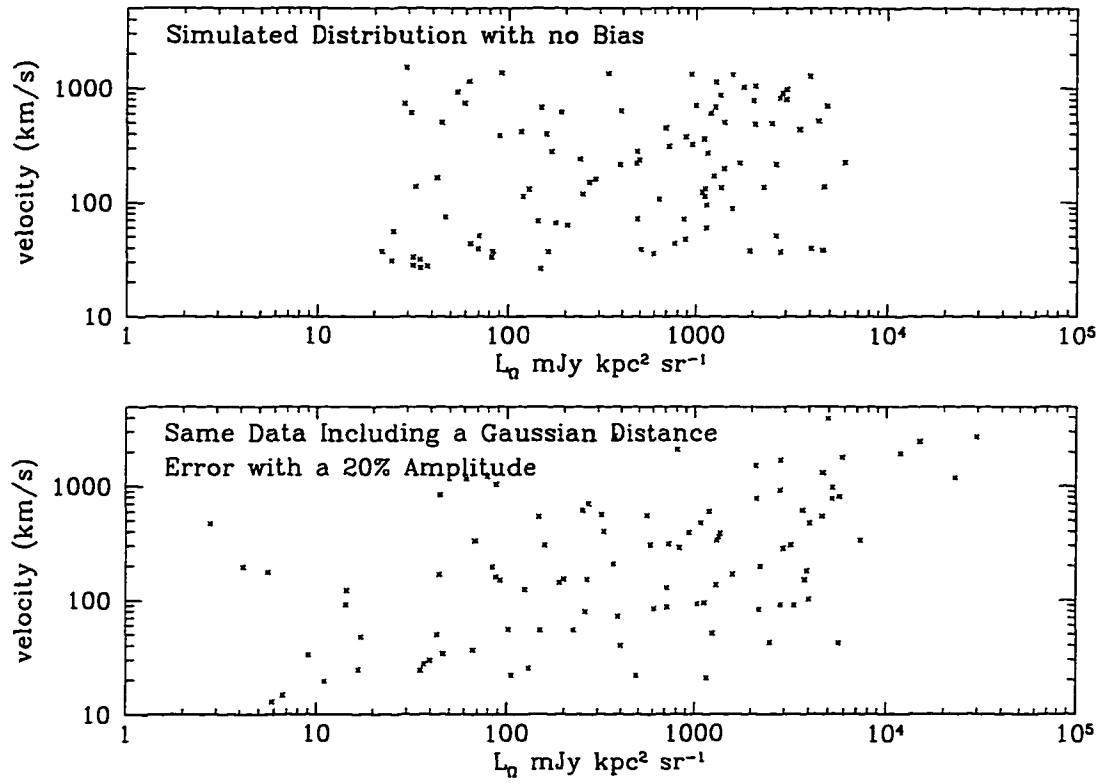


Figure 4.2 Luminosity versus velocity for a simulated sample (no biases) without distance errors on the left and with distance errors on the right. The pulsars in the simulated sample are evenly chosen in velocity/luminosity space with no intrinsic biases. We assume the distance errors are Gaussian with a magnitude of 20% distance. The faster pulsars *appear* to be more luminous.

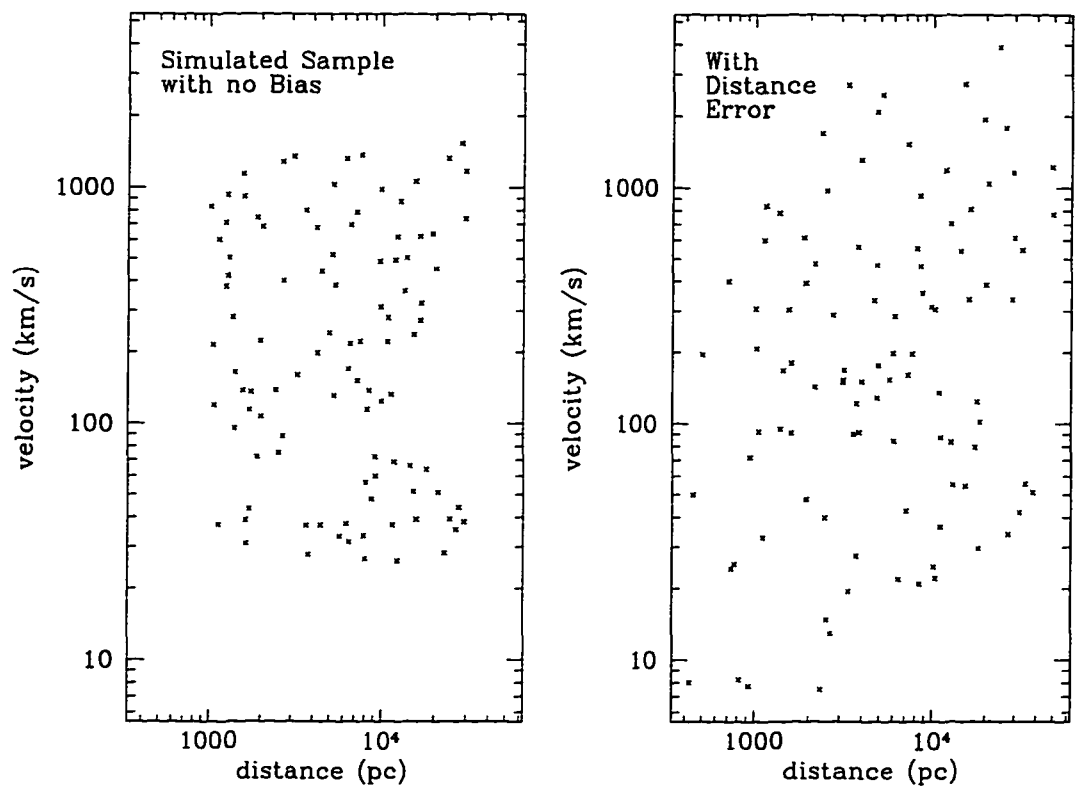


Figure 4.3 The same as Figure 2, except velocity is plotted versus distance. Note that with distance errors, another fictitious bias appears with the nearby pulsars tending to have slower velocities.

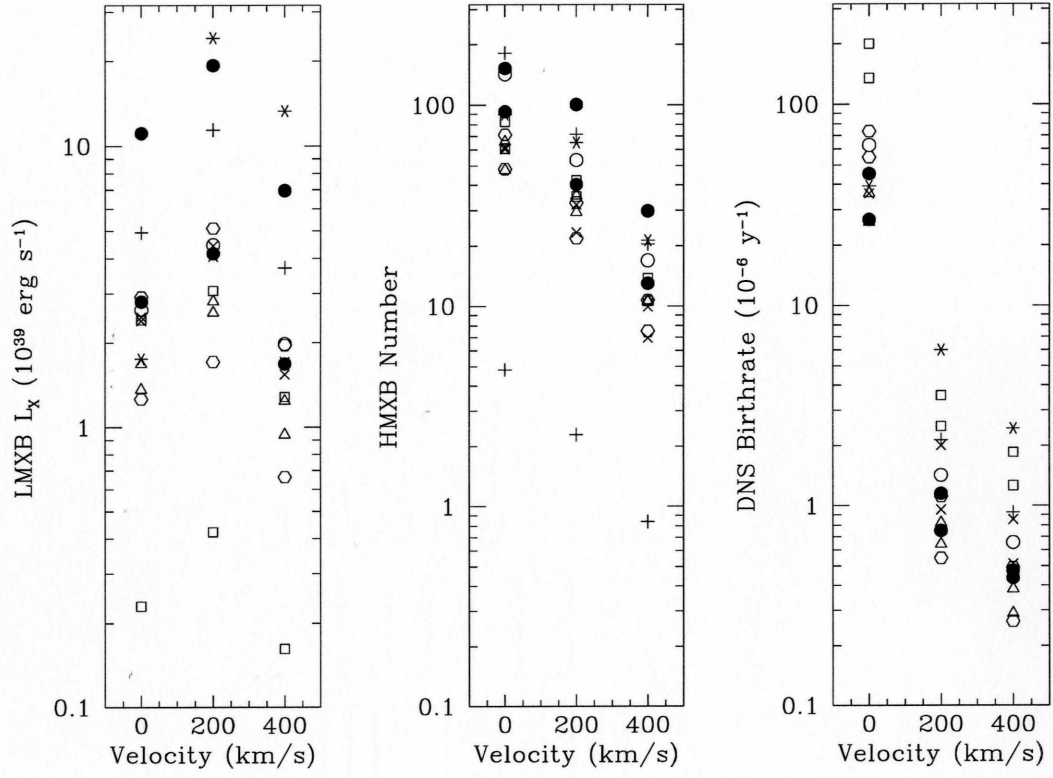


Figure 4.4 The dependence of the various neutron-star binaries with respect to the various initial binary and evolutionary parameters and velocity. The filled circles correspond to the two standard parameter set that we use with $q_0 = 0.35, 0.15$. The open symbols correspond to the initial binary parameters (§4.4.1) and the skeletal symbols correspond to the binary evolution parameters (§4.4.2).

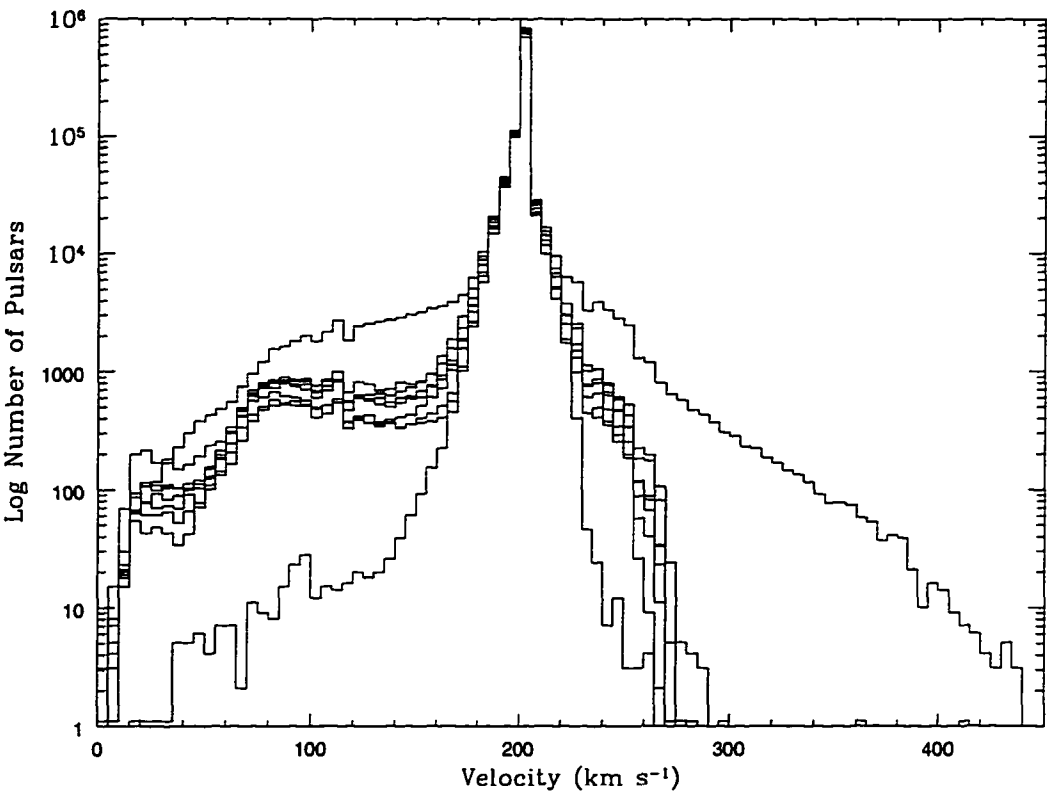


Figure 4.5 The velocity distribution of pulsars for a range of initial and binary-evolution parameters with a δ -function kick of 200 km/s. The binary parameters affect only a small number of the pulsars. The typical pulsar velocity is unchanged by even extreme changes in the binary parameters. The largest differences come from assuming that there is no mass lost from winds.

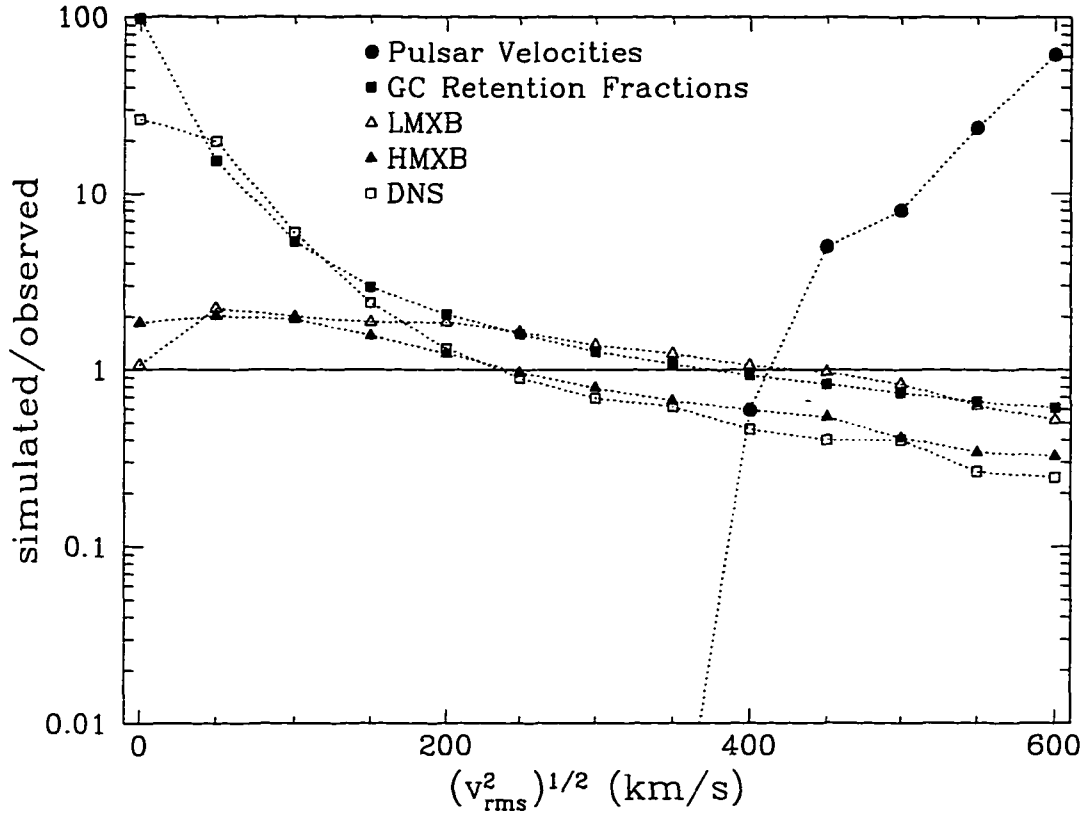


Figure 4.6 The simulated populations normalized by the observations versus the root-mean-square velocity for a Maxwellian Distribution. For the pulsars, we plot $(99.99 - P)$ where P is the percentage probability that the simulated velocity distribution and the observed velocity distribution are not from the same parent population. We use our standard set of binary parameters. A “successful” solution is one for which all the normalized numbers are greater than unity simultaneously.

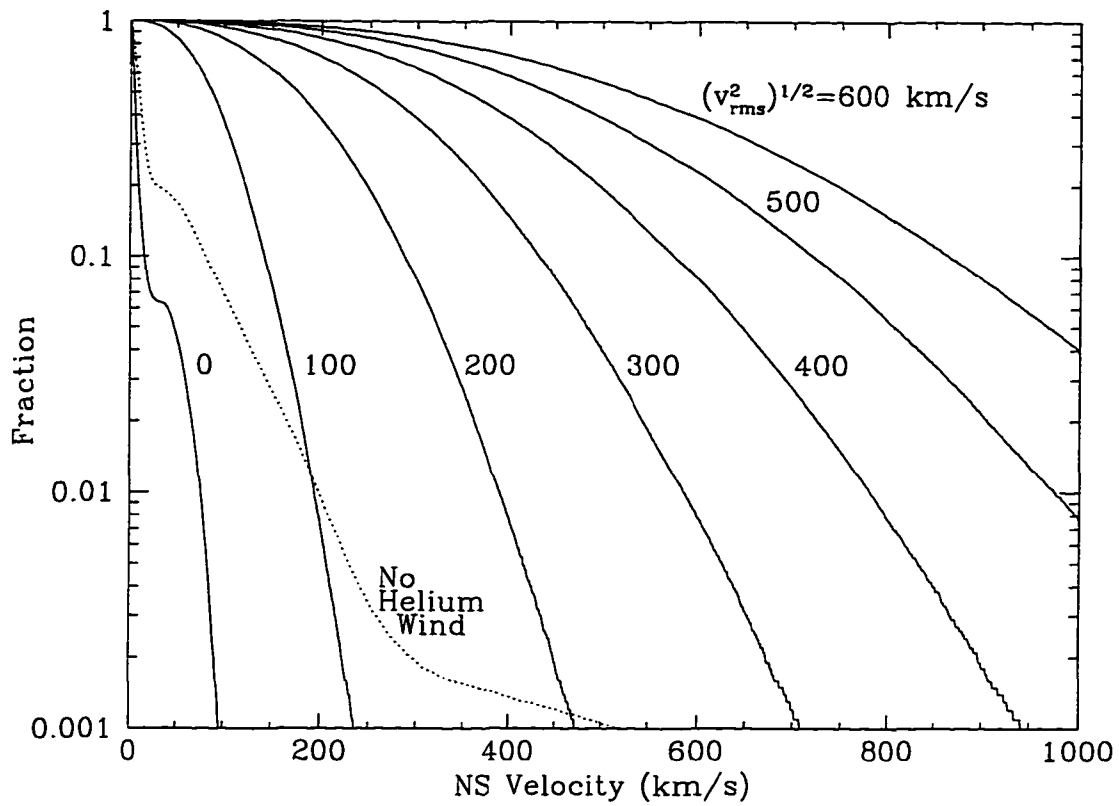


Figure 4.7 Fraction of Neutron Stars with a velocity greater than a given velocity versus that velocity for the series of Maxwellian kick distributions. A zero kick simulation with no mass loss from winds is included to give the maximum effects from the binary parameters.

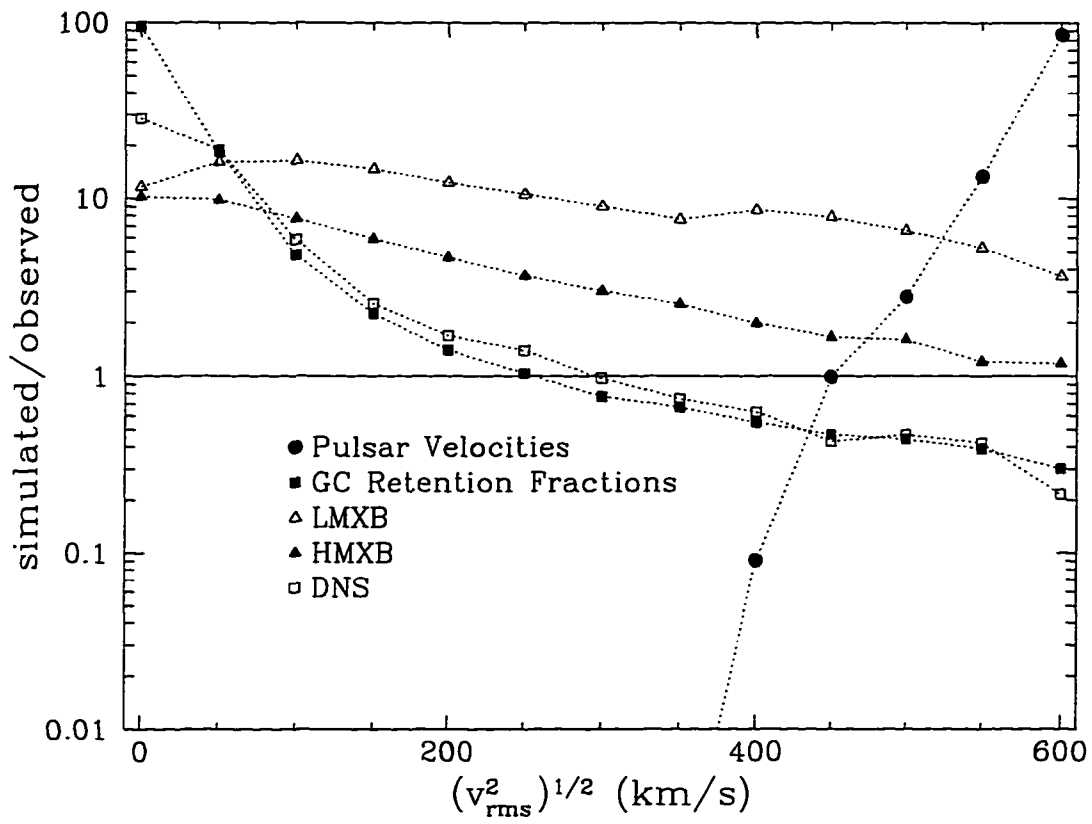


Figure 4.8 The same as Fig. 6, but with $q_0 = 0.15$ and $M_{l,u}=10,100M_{\odot}$.

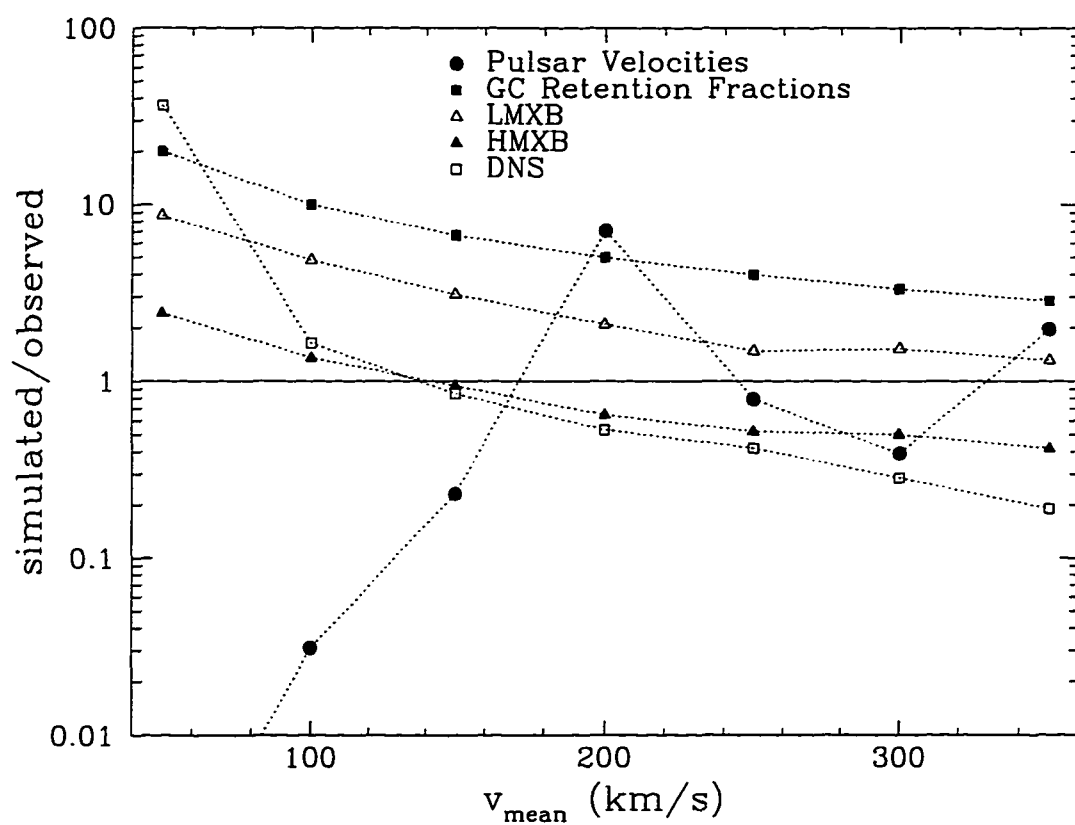


Figure 4.9 The same as Fig. 6, but for flat distributions with $q_0 = 0.15$.

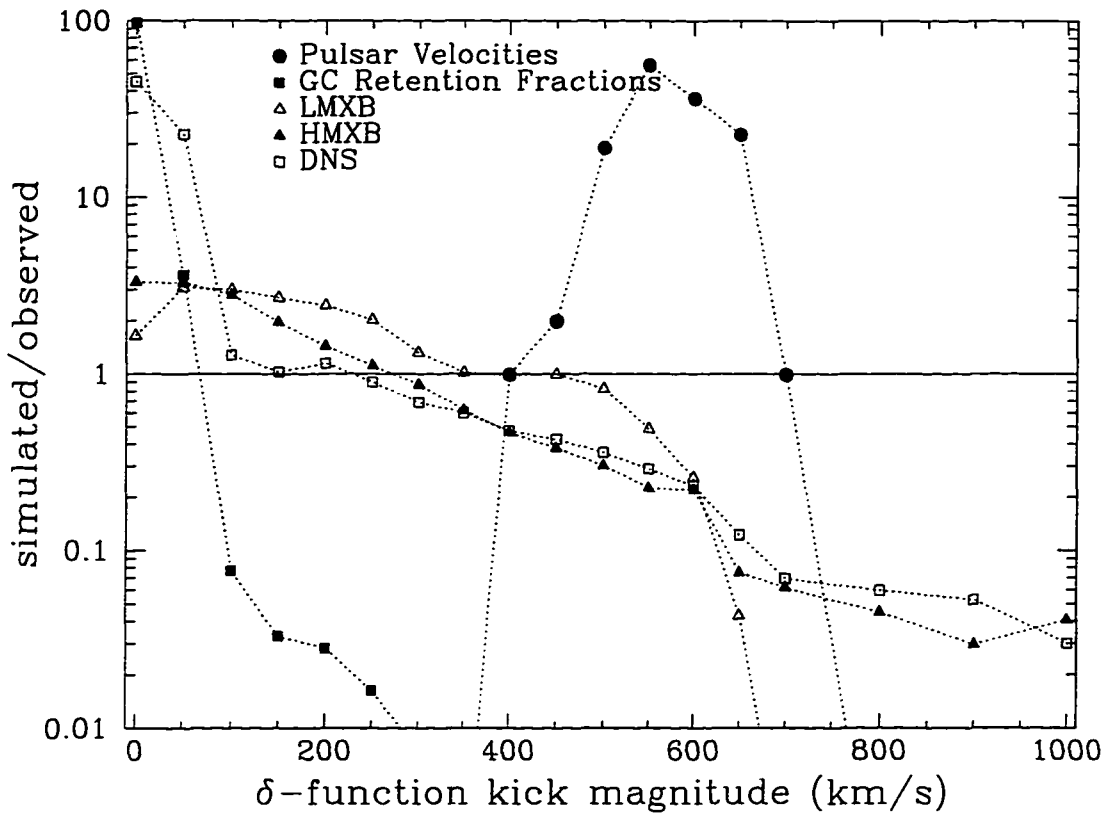


Figure 4.10 The same as Fig. 6, but for δ -function kicks.

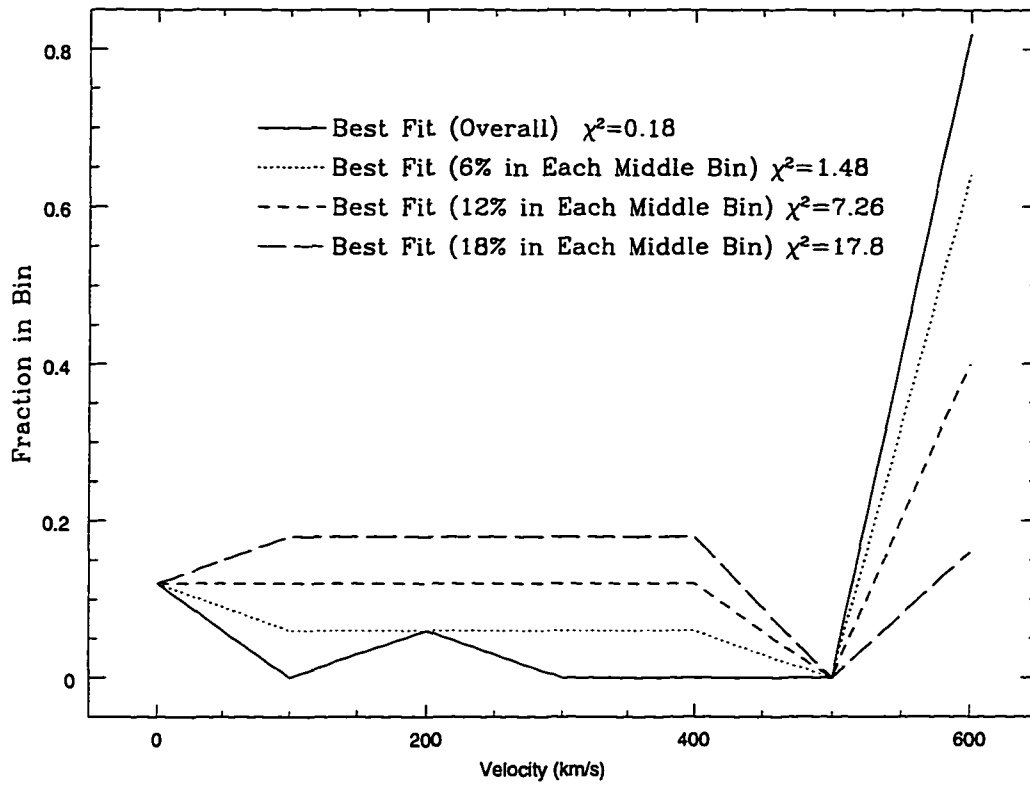


Figure 4.11 Kick distributions with fraction of neutron stars versus velocity bin. The solid line denotes the best-fitting overall kick profile. The remaining curves are constrained by requiring that the middle range of velocities be non-zero to varying degrees.

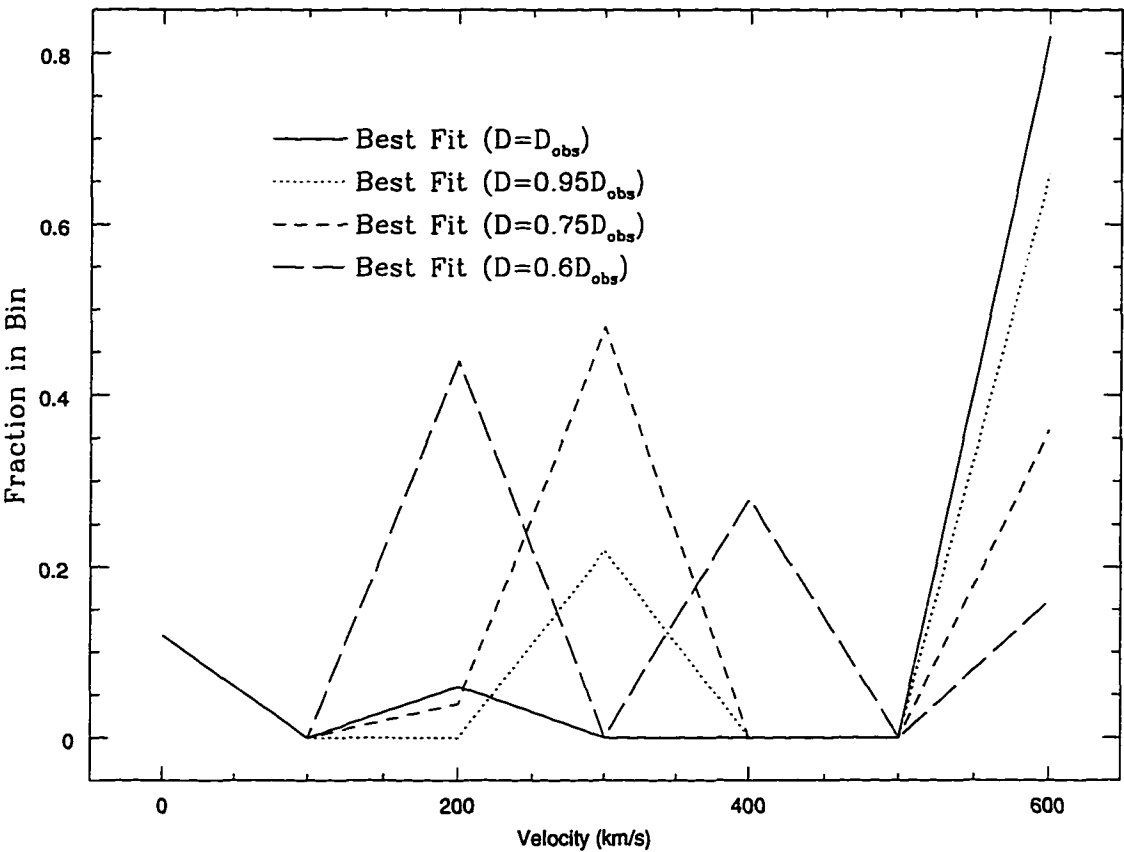


Figure 4.12 Same as Figure 11, but with the best-fitting overall profiles for a range of distance scale factors.

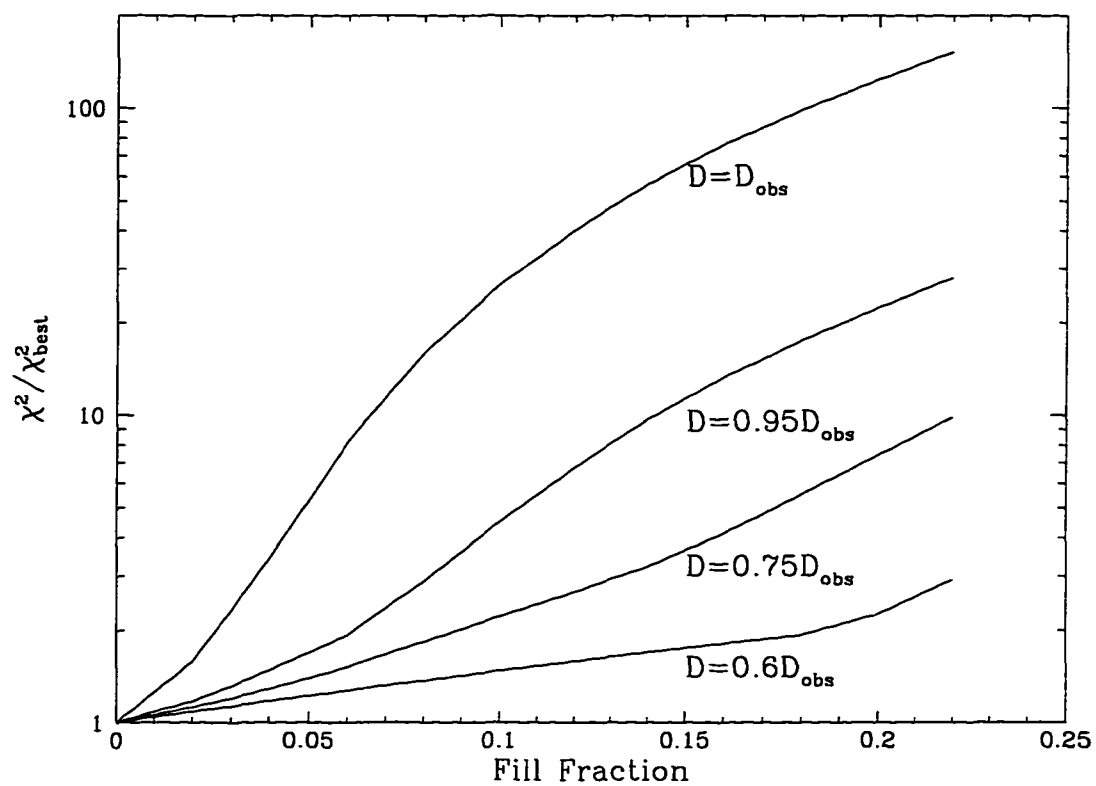


Figure 4.13 χ^2 residuals versus the degree to which the middle velocities are filled, normalized by the residuals from the best-fitting overall distribution. The curves represent a range of scale factors for the distance.

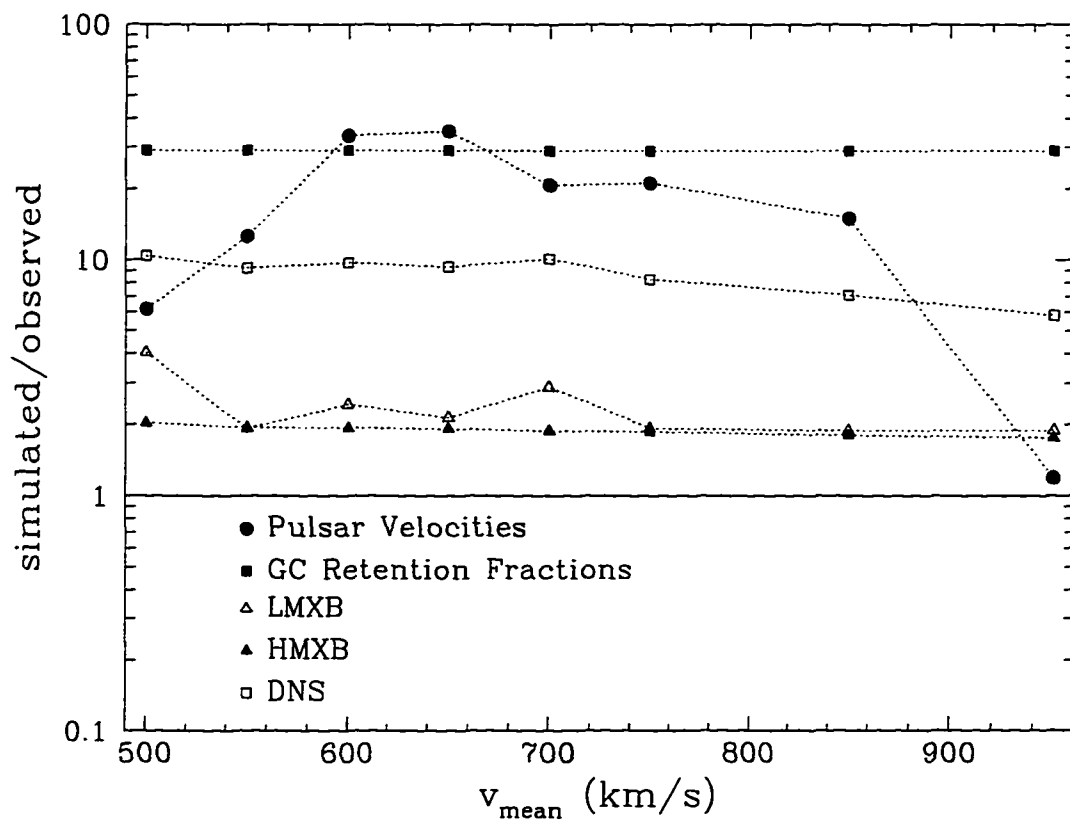


Figure 4.14 Same as Fig 6. with a double-peaked δ -function distribution: 30% at 0 km s^{-1} and 70% at the value on the plot. Again, we use $q_0 = 0.15$.

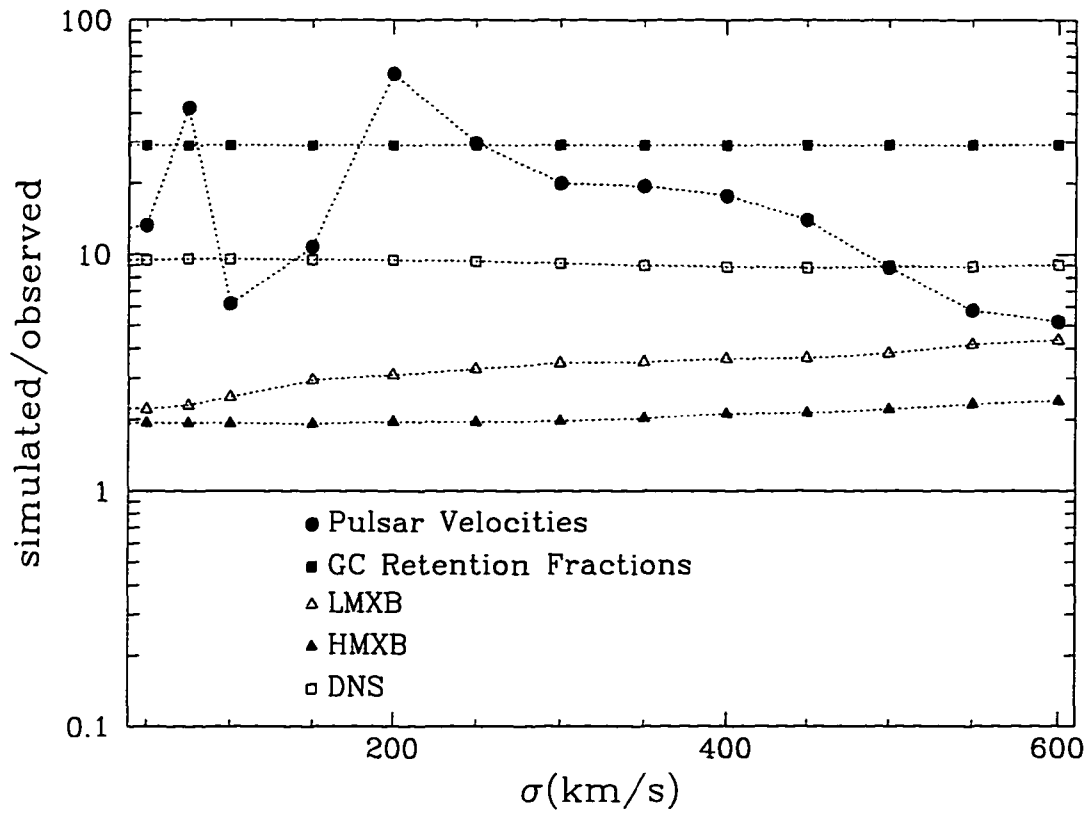


Figure 4.15 Same as Fig 6. with a double-peaked distribution: 30% at 0 km s^{-1} and 70% with a flat distribution with a mean at 625 km s^{-1} with a mean: σ . Again, we use $q_0 = 0.15$.

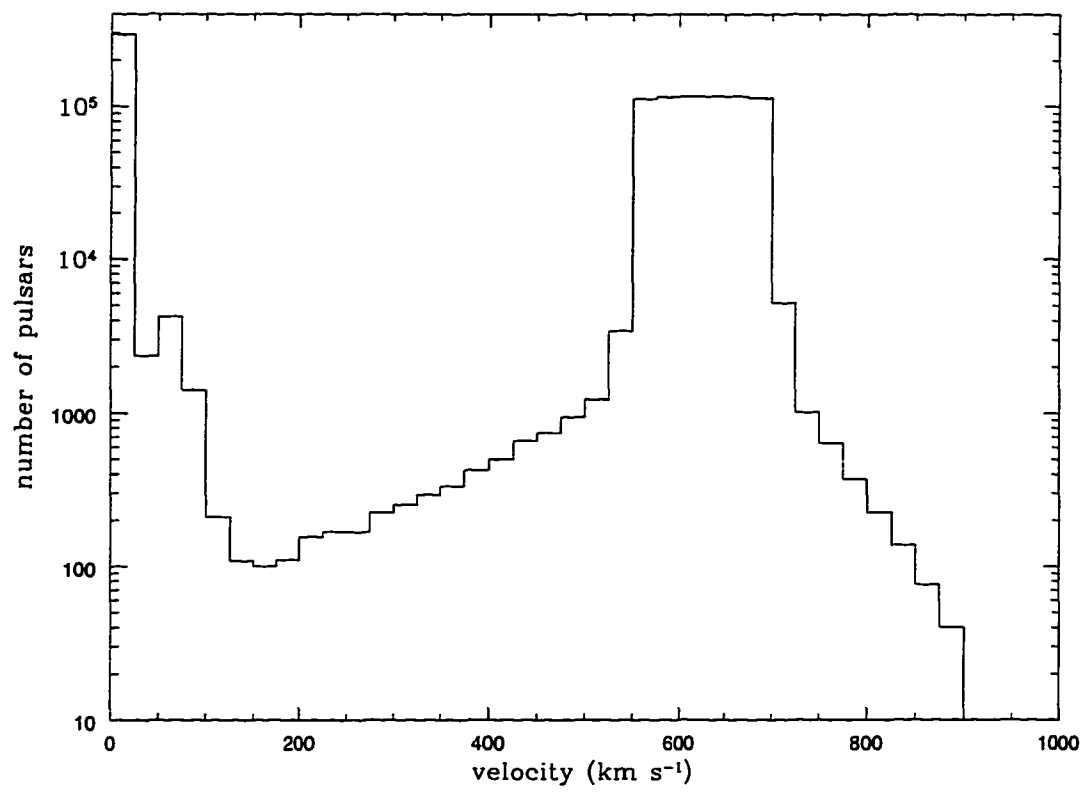


Figure 4.16 The neutron star velocity distribution for our best fitting double peaked distribution.

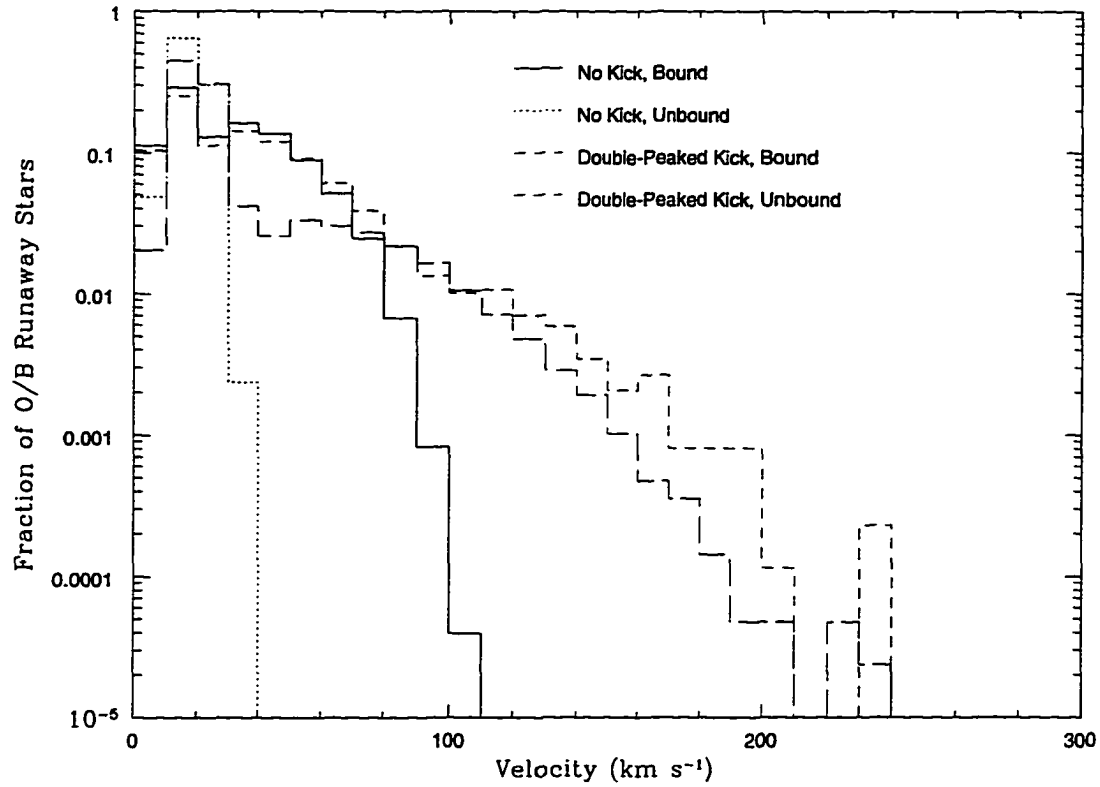


Figure 4.17 The velocity distribution of O/B stars for simulations with no kick (solid line - bound systems, dotted line - unbound O/B stars) and for our best fitting double peaked distribution (long-dashed line - bound systems, short-dashed line - unbound systems.)

CHAPTER 5

EJECTA FROM ACCRETION INDUCED COLLAPSE: A COSMIC POLLUTANT

Brief Summary

The accretion induced collapse (AIC) of a white dwarf has been invoked to account for gamma-ray bursts, Type Ia supernovae, and a number of problematic neutron star populations. So far, AIC studies have focussed on determining the event rates from binary evolution models and little attention has been directed toward understanding the collapse itself. However, the formation of a neutron star through AIC of a white dwarf is followed by the ejection of rare neutron-rich isotopes. The observed abundance of these chemical elements may set a more reliable upper limit to the rate at which these events have taken place over the history of the galaxy.

In this paper, we present a thorough study of the collapse of a massive white dwarf and determine the amount and composition of the ejected material. We discuss the importance of the input physics (equation of state, neutrino transport,

rotation) in determining these quantities.

5.1. Introduction

As an accreting white dwarf approaches the Chandrasekhar mass limit, two physical effects compete to determine its fate. If the central densities and temperatures become sufficiently high to ignite explosive nuclear burning, a thermonuclear explosion ensues. However, electron capture may reduce the central pressure of the white dwarf, causing it to collapse into a neutron star prior to the ignition of a thermonuclear explosion can occur. The path the white dwarf actually follows depends upon its initial state and the rate at which it accretes material (Nomoto & Kondo 1991). Combining results of binary evolution and accretion models, Nomoto & Kondo predict that the rate of the accretion-induced collapse of white dwarfs (AICs) is comparable or greater than the rate of thermonuclear explosions of Chandrasekhar mass white dwarfs.

The thermonuclear explosion of white dwarfs has become the “standard” mechanism behind Type Ia supernovae (see Woosley & Weaver 1986 for a summary) and a large amount of effort has been devoted to understanding the details of this explosion. The accretion induced collapse of a white dwarf has garnered much less attention and the evolution of the collapse is much less thoroughly understood. This lack of attention has allowed rampant speculation about the observable properties of AICs and the characteristics of the neutron stars born in these events.

Assuming some mass ejection occurs during collapse, AICs have been proposed as an alternate mechanism for Type Ia supernova (Colgate, Petschek, & Kriese 1980) and as a source for gamma-ray bursts (Paczynski 1986, Goodman 1986, Goodman, Dar, & Nussinov 1987, Paczynski 1990, Dar et al. 1992). Neutron

stars formed through AICs have also been used to explain a variety of troublesome neutron star systems (see Canal, Isern, & Labay 1990 for a review). In addition, AICs have been proposed as an alternate channel to form millisecond pulsars in globular clusters and the galactic disk, circumventing the LMXB phase (Bailyn & Grindlay 1988, Bailyn & Grindlay 1990, Kulkarni, Narayan, & Romani 1990, Ray & Kluzniak 1990, Ruderman 1991, Chen & Ruderman 1993, Chen & Leonard 1993). AICs have also been invoked in several X-ray binary formation scenarios (Canal et al. 1990, van den Heuvel 1984) and as a formation mechanism for specific cases of close neutron star binaries (Ergma 1993).

For AICs to be a viable solution for any of these objects, they must satisfy at least two basic requirements. First and foremost, AIC events must occur at a rate comparable to that predicted by the observations. This can be verified by either determining the progenitor systems leading to AICs and their formation rate or by comparing observed abundances of rare isotopes with the computed production rate of these elements in single AIC events. While the first approach has been the most widely used, it suffers from the large uncertainties associated with our current knowledge of binary system evolution. The second approach obviously requires a detailed knowledge of the dynamics of the collapse and nucleosynthetic yield of the ejecta (Woosley & Baron 1987, hereafter WB87). Because matter is ejected at a low electron fraction, the nucleosynthetic products from AICs include many anomalous neutron-rich isotopes (e.g. ^{62}Ni , ^{66}Zn , ^{68}Zn , ^{87}Rb , and ^{88}Sr) which pollute the interstellar medium. Comparing the observed abundance of these elements with the amount ejected per event, we can place constraints on the allowable rate of AICs in the galaxy. AICs must also have the appropriate observational signature to match that of the observations. This second requirement pertains most strongly to gamma-ray bursts and Type Ia supernovae. For example, to be a source for

gamma-ray bursts, AICs must be able to produce sufficient energy in gamma-rays to explain the observations. For Type Ia supernovae, AICs must reproduce both the light curves and spectra of the observed Type Ia supernovae.

The previous work on AICs has identified three possible ejection mechanisms. Mass can be ejected by the outward moving shock launched as the collapsing core rebounds when reaching nuclear densities. However, simulations (Baron et al. 1987; Mayle & Wilson 1988, hereafter MW88; Woosley and Baron 1992, hereafter WB92) have shown that, just as in Type II supernovae, the bounce shock stalls because of energy losses due to neutrino emission and dissociation. MW88 carried out simulations of the collapse of massive star ($8 - 10M_{\odot}$) OMgNe cores which have similar structures to most AIC progenitor models. They showed that neutrino-driven explosions akin to the ones obtained as a result of the so-called “delayed mechanism” in Type II supernovae could occur and lead to the ejection of $\sim 0.042M_{\odot}$ on timescales ~ 200 ms. WB92 calculated the evolution of the collapse of a CO white dwarf and showed that $\sim 0.01M_{\odot}$ was ejected at late times (~ 2 s) by a strong neutrino driven wind resulting from the cooling of the neutron star. In their calculation, the explosion itself did not result in any ejected matter, contrary to the results by MW88.

Whether in the delayed explosion or in the wind, the mass ejection mechanism relies upon neutrino absorption, which in turn, leads the ejection of neutron-rich material and, hence, disastrous nucleosynthetic yields from AICs. Thus, even though the amount of ejecta may be quite small, its abundance of neutron-rich nuclear products can severely contaminate the galaxy. To avoid nuclear contamination, one can either limit the amount of matter ejected or the rate at which these events occur. By calculating the amount and composition of the

ejecta in AIC events, we limit the event rate of AICs and place constraints on the evolution of binary stars. Conversely, the knowledge of the event rate can provide important information on the physics of core collapse, neutrino driven explosions and winds.

In this paper, we have run a series of AIC simulations using the CO white dwarf progenitor from the WB92 model (Nomoto 1986) to determine the amount and composition of the ejecta. To measure the reliability of our results, we vary a number of parameters such as the details of the neutrino physics, the equation of state, and the initial rotation of the white dwarf. We discuss the models in §2 and summarize the results and their implications in §3.

5.2. Models and Results

Table 5.1 summarizes the entire set (60 in total) of simulations we have performed. The different simulations were run to test the sensitivity of the results to changes in the neutrino physics (both source and transport columns 3 and 4 of Table 5.1), the inclusion of relativistic effects, (run 6), the choice of the equation of state (EOS) (column 2), multi-dimensional effects (run 2) and initial rotation rate of the white dwarf (run 3).

Most of these parameter variations lead to relatively small changes in the results. However, changes in the equation of state for dense matter which lead to significant differences in the results. We performed calculations using either the equation of state by Lattimer & Swesty (1992) or Baron, Cooperstein, & Kahana (1985). The large differences can be appreciated by comparing density profiles (Fig. 1) and the mass-point trajectories over the course of the simulation (Figs 2,3).

Below, we describe in detail the physical modules and the variations that were used in order to assess the sensitivity of the results.

5.2.1. Numerical Methods

The internal structure of the initial white dwarf is taken from WB92 (Nomoto 1986). The density profile of our initial model is represented by the solid line in Figure 1. This model is then mapped into our one- and/or two-dimensional codes and run for 0.2s. The one-dimensional simulations were performed using an explicit, grid-based Lagrangian code (Benz 1991, Fryer, Benz & Herant 1996) with a second order Runge-Kutta integrator and typically ~ 110 zones. This code does not include any form of convection modeling (mixing length or other). The two-dimensional simulations were performed using the Smooth Particle Hydrodynamics (SPH) code discussed in Herant et al. (1994) with typically ~ 2300 particles.

5.2.2. Neutrino Physics

To illustrate the importance of neutrinos on the composition of the ejecta, we compare the results of a simulation which includes the effects of neutrino physics (Fig. 2 - run 1) and a simulation with no such effects (Fig. 4 - run 24). By comparing the mass-point trajectories between these two simulations, we note that without the cooling effects of neutrino emission, the bounce shock does not stall and an explosion develops. Although the shock stalls for the simulation which includes the effects of neutrino physics, neutrino absorption revives the explosion, ejecting a comparable amount of matter. However, the net effect of neutrino absorption is to lower the electron fraction of the ejecta. Although the amount of material is roughly equal in the two simulations, the actual composition differs immensely.

Including neutrino physics in the simulations involves two difficulties: The determination and numerical representation of the processes that emit or absorb neutrinos and the subsequent transport of these neutrinos through matter. Our neutrino processes are described in Herant et al. (1994) and include many of the possible emission and absorption rates for the standard three neutrino species (electron neutrino, electron antineutrino, and the entire set of μ and τ neutrinos and antineutrinos).

In many Type II supernova simulations, it is often assumed that the neutrinos are emitted from ultra-relativistic electrons ($T \gg \frac{1}{2} \text{MeV}$). This is not always necessarily a good approximation. For example, a numerical representation of the electron/positron neutrino emission rates and luminosity has been derived by Takahashi, El Eid & Hillebrandt (1977):

$$\lambda_{\substack{e^-p \\ e^+n}} = C_2 \beta^{-5} \left[F_4(\pm\eta) \pm (2 - 2\Delta) F_3(\pm\eta) \beta + \left(\frac{1 - 8\Delta + 2\Delta^2}{2} \right) F_2(\pm\eta) \beta^2 \right. \\ \left. \pm (2\Delta^2 - \Delta) F_1(\pm\eta) \beta^3 + \left(\frac{4\Delta^2 - 1}{8} \right) F_0(\pm\eta) \beta^4 \right] \quad (81)$$

and

$$L_{\bar{\nu}} = C_3 \beta^{-6} \left[F_5(\pm\eta) \pm (2 - 3\Delta) F_4(\pm\eta) \beta + \left(\frac{1 - 12\Delta + 6\Delta^2}{2} \right) F_3(\pm\eta) \beta^2 \right. \\ \left. \pm \left(\frac{-3\Delta \pm 12\Delta^2 - 2\Delta^3}{2} \right) F_2(\pm\eta) \beta^3 + \left(\frac{-1 + 12\Delta^2 - 16\Delta^3}{8} \right) F_1(\pm\eta) \beta^4 \right. \\ \left. \pm \left(\frac{2 + 3\Delta - 4\Delta^3}{8} \right) F_0(\pm\eta) \beta^5 \right] \quad (82)$$

where $\lambda_{\substack{e^-p \\ e^+n}}$ are the transition rates for electron and positron capture, $L_{\bar{\nu}}$ are the electron neutrino and anti-electron neutrino luminosities, $C_2 = 6.15 \times 10^{-4} \text{ s}^{-1}$ per nucleon, $C_3 = 5.04 \times 10^{-10} \text{ erg s}^{-1}$ per nucleon, $\Delta = 1.531 \text{ MeV}$ is the neutron-hydrogen mass difference and $\beta = \frac{m_e c^2}{k_B T}$. F_n are Fermi integrals of order n and η is the degeneracy parameter.

Adopting the ultra-relativistic limit, WB92 have simplified these equations, taking only the first term in each equation. To estimate the importance of this assumption, we have used both the limited and the full equations. In Table 5.1, the runs using the full equations are identified by the letters TEH while those using the ultra-relativistic assumption are marked by WB92. As can be seen from a careful comparison of these simulations, adopting the ultra-relativistic limit does not change the results appreciably in most cases.

Despite the low cross-sections for neutrino interactions, the high densities involved in core-collapse scenarios place the neutrinos within the depths of the collapsing star in the diffusion regime. Thus, the neutrino transport must include both the diffusion and free-streaming limits of the transport equations. The “standard” approximation to couple these two extremes calls upon the use of a flux-limiter (see for example, Janka 1991). We have incorporated several different flux-limiters (Bowers & Wilson 1982; Levermore & Pomraning (1981); Herant et al. 1994) and the properties of their ejecta can be compared in column 2 of Table 5.1. The Bowers-Wilson and Levermore-Pomraning flux limiters seem to bound the more accurate Monte-Carlo calculations by Janka (1991) and can be used to gauge the effect of the flux-limiter on the amount and composition of the ejecta. By comparing these two flux limiters in otherwise identical simulations (e.g. run 8 and 12), we see that the two approximations in the neutrino diffusion lead to differences by factors of 4-5 in the explosion energies but only 10% differences in the mass ejected.

5.2.3. Equation of State

Uncertainties surrounding the equation of state for dense matter lead to the largest differences in the ejecta from AICs. We used two such equations of state:

the one described in Herant et al. (1994) which couples the nuclear equation of state by Lattimer & Swesty (1991) to a low density equation of state (Blinnikov, Dunina-Barkovskaya & Nadyozhin 1996) and a nuclear statistical equilibrium (NSE) scheme (Hix et al. 1994) (hereafter called SL EOS), and the equation of state developed by Baron, Cooperstein, & Kahana (1985 hereafter called BCK EOS), which covers both low- and high-density regimes. The BCK EOS is the equation of state used by WB92. For our progenitor, the effects of nuclear burning were minimal. We verified this by running a simulation (run 7) in which we added a nuclear network to our code (Benz, Hills, & Thielemann 1989). It is apparent that an NSE scheme is sufficient to model the effects of nuclear burning during AICs.

Again, the main results of our simulations using one or the other equation of state are listed in Table 5.1 (see column 1 - e.g. compare runs 8 and 20). By using the BCK equation of state, we recover the results by WB92. However, the equation of state dramatically affects the amount and composition of the ejecta in the simulations. Swesty, Lattimer, & Myra (1994), in a previous comparison between the two equations of state, report similar findings (the softer BCK equation of state leads to denser, and hotter, cores after bounce). These differences have been discussed by Swesty, Lattimer, & Myra who argue that, given the standard equation of state parameters for the BCK EOS, the SL EOS is physically more accurate. We have run the SL EOS using two values for the incompressibility of bulk nuclear matter ($K_s = 180, 375$ MeV) and have run a grid of the faster BCK EOS varying the BCK gamma ($1.5 < \gamma < 3.5$), the bulk surface coefficient ($25 < W_s < 38$), the symmetric bulk compressibility parameter ($180 \text{ MeV} < K_0^{sym} < 375 \text{ MeV}$), and an asymmetry parameter ($1.5 < xkz < 3.5$). Table 5.2 gives the results for this grid of simulations in which we used the Levermore-Pomraning flux limiter. Despite this

wide range in the physical parameters, the results from the BCK EOS never agreed with those from the SL EOS.

The ratio of the SL EOS pressure to the BCK EOS pressure along an $S = 2$ k_B /nucleon adiabat is plotted in Figure 5. Note that for densities less than 10^{14} g cm^{-3} , the pressure of the BCK EOS is 10-20% greater than that of the SL EOS. This explains the slower collapse for the simulations using the BCK EOS. In Figure 1, we have plotted the density profiles at 40 ms from simulations using the BCK EOS, the SL EOS, and a simulation where the pressure from the BCK EOS was artificially scaled down by 20%. This small modification made a large difference in the evolution of the collapse and emphasizes the strong dependence of our results on the equation of state.

Coupled with the SL EOS, we have implemented spherically symmetric general relativity as described by van Riper (1979). From table 5.1, we can compare the results of simulations with or without general relativity (runs 1,6). The primary effect of general relativity is to cause the material to fall deeper into the potential well resulting in increased neutrino absorption. Hence, the material ejected has significantly lower electron fractions. However, since the progenitor structure was obtained by Nomoto (1986) without including general relativity effects, we might be overestimating these effects by introducing them a posteriori.

5.2.4. Convection and Rotation

Two-dimensional simulations of AICs can be used to test both the effects of convection and rotation. Since large entropy gradients do not develop in the one-dimensional simulations, we do not expect convection to cause large differences in the ejecta from AICs. We first use our two-dimensional simulations to verify that

convection does not play a major role in the collapse and ejecta of AICs. Given the resolution differences in our one- and two-dimensional models, the results are strikingly similar (compare run 1 and 2 in Table 5.1).

The progenitors to AICs accrete not only mass, but angular momentum, as the white dwarf approaches the Chandrasekhar limit. Typical rotation periods for cataclysmic variables range from 200 – 1200 s (Liebert 1980) although periods of ~ 30 s exist (King & Lasota 1991). A lower limit on the rotation period is set by the break-up spin period (~ 0.5 s for solar-mass white dwarfs). With these rotation periods, we can approximate the white dwarf as a Maclaurin spheroid (Shapiro & Teukolsky 1983). The stability of a Maclaurin spheroid can be determined by calculating the ratio of the kinetic energy to the gravitational potential energy (τ_c). If this ratio rises above 0.1375, secular instabilities set in and our assumption that the collapse is roughly spherical will no longer be valid.

In our models, we assume solid-body rotation and conserve each individual particle's angular momentum for the duration of the simulation. We take an extreme case of a white dwarf rotating with a 2 s period prior to collapse. We conserve angular momentum and collapse the white dwarf to our initial conditions. τ_c for this simulation is initially near 0.008 and increases to 0.05 near the time of bounce so our assumption that the collapse is roughly spherical holds throughout the simulation.

However, for this rotation period, the ratio of surface rotational velocity over the keplerian velocity is 0.39 and rotation severely affects the motion of this outer material. This ratio drops precipitously as we move inward in radius. For example, this ratio is 0.19 at the radius which encloses $1.3M_\odot$ (still 94% of the white dwarf mass). Thus, while the collapse of the outer envelope of a white dwarf is affected

by rotation, the core collapse itself is not. Comparing runs 2 and 3 in Table 5.1, we see that the amount and composition of the ejecta is not altered significantly by the effects of rotation.

5.2.5. Neutrino Wind

The results in Table 5.1 do not include any mass loss from neutrino-driven winds. The amount of this ejecta is small when compared to that of our simulations using the SL equation of state (WB92 predict $\sim 0.005M_{\odot}/s$ for the first two seconds). However, for the BCK EOS simulations, neutrino-driven winds dominate the mass loss. Using a cell-adding routine, we follow the fate of an AIC model beyond the delayed neutrino-induced explosion to obtain the wind-driven mass loss (run 1). Because we are also modeling the core, we are limited to very small timesteps and are able to follow this phase for only 0.4s after bounce. We find that during this period of time, an additional $\sim 0.002M_{\odot}$ peels off the neutron star. Thus, in this limited way, we confirm the results obtained by WB92 that further neutrino driven mass loss is to be expected. Independent of the equation of state or other input physics, it is likely that a neutrino-wind phase exists and $\sim 0.01M_{\odot}$ is ejected during this phase.

5.3. Discussion and Conclusions

We have performed a number of AIC simulations varying the input physics within the range of current uncertainties and obtaining the corresponding mass ejected from AIC. We can use these results to constrain the rate of AIC events in the galaxy. However, these constraints are uncertain primarily due to the lack of understanding of dense matter physics. Because the nucleosynthesis is so dependent

upon the neutrino absorption, one cannot exclude that a more accurate treatment of neutrino physics may also have a decided effect. With these caveat in mind, the nucleosynthetic yields place the most stringent constraints upon the rates of AICs.

Hartmann, Woosley, and El Eid (1985) estimate that there must be less than $10^{-5} M_{\odot}$ of $Y_e < 0.4$ material ejected per supernova to avoid anomalous abundances of particular isotopes (e.g. ^{62}Ni , ^{66}Zn , ^{68}Zn , ^{87}Rb , and ^{88}Sr). Using the value of $0.02 M_{\odot}$ of material with less than $Y_e < 0.4$ ejected per AIC events (see Table 5.1) and assuming a supernova rate of two per century for the galaxy we find that the upper limit for rate of AICs must be $(2/100\text{y}^{-1})(10^{-5} M_{\odot})/(0.02 M_{\odot}) = 10^{-5} \text{ y}^{-1}$. Note that we have assumed AIC to be the only source for material with such a low Y_e . Should there be another source, the allowed AIC rate will be correspondingly smaller. A more conservative estimate is obtained by assuming that this material is ejected with $0.45 < Y_e < 0.40$ rather than with $Y_e < 0.4$ (a real possibility given the crude neutrino physics used). Following the method of WB92, the upper limit for the rate of AICs becomes $(1/170,000)(1/0.07)(1/0.13)(2/100) = 1.3 \times 10^{-5} \text{ y}^{-1}$. Although the electron fraction is very sensitive to the neutrino physics, a large portion of the low Y_e ejecta must change considerably to alter our conclusions. If we include general relativistic effects, this rate decreases by an order of magnitude.

Several attempts have been made to estimate the rate of AICs required to explain various neutron star populations. Assuming OMgNe white dwarfs to be the sole contributor to AICs, Iben, Tutukov, & Yungelson predict an AIC rate of $3 \times 10^{-4} \text{ y}^{-1}$ in the galactic disk. Even with this high rate, AICs do not contribute significantly to any of the neutron star systems in the galactic disk. Bailyn and Grindlay (1990), in an effort to explain the millisecond pulsar population in globular clusters, require a comparable rate ($\sim 10^{-4} \text{ y}^{-1}$) in the galactic globular

cluster population. These rates are an order of magnitude higher than that allowed from our results suggesting that AICs can not be used to solve problems pertaining to neutron star systems. However, specific objects may still be explained by AICs.

The gamma-ray burst models require that less than about $10^{-6-7}M_{\odot}$ of baryonic matter is ejected along with the gamma-ray burst fireball (Paczynski 1986, Goodman 1986, Goodman, Dar, & Nussinov 1987, Paczynski 1990, Dar et al. 1992). With our high ejected masses, we do not get the high velocities required to create gamma-rays. In addition, assuming the Nomoto & Kondo (1991) prediction that AICs are more common than Chandrasekhar mass thermonuclear explosions, the limit on the rate of AICs is also an upper limit to the number of Type Ias that can be explained by Chandrasekhar mass thermonuclear explosions. Then from our results, less than 1% of the observed Type Ias come from this “standard” mechanism. However, the amount of nickel ejected and explosion energy are becoming tantalizingly close to the properties of peculiar Type Ia supernovae such as SN 1991bg (Filippenko et al. 1992).

The applications of AICs, both in producing neutron stars and supernova or gamma-ray outbursts, mandates continued research on their evolution. To fully understand the fate of AICs, the physical processes that cause the largest variations in the results (in particular, the equation of state and the effects of general relativity) must be understood. The characteristics of the progenitors may also have an effect on the subsequent evolution. If we can reduce the uncertainties due to numerical techniques and initial conditions, we are then in the position to do one of two things: either by understanding the basic physics of dense matter, we can calculate accurate upper limits of the event rate of AICs, or by knowing something of the event rate of AICs, we can gain some understanding of the basic

physics of dense matter.

Table 5.1. AIC Simulations

Model Num.	EOS ^a	Flux ^b Limiter	ν^c Source Term	KE_{exp} 10^{51} ergs	$Y_e > 0.45$	$M_{ej}(M_\odot)$ $0.40 < Y_e < 0.45$	$Y_e < 0.40$
1	SL	MH	TEH	1.3	0.09	0.04	0.07
2	SL-2D ^d	MH	TEH	0.6	0.07	0.01	0.09
3	SL-2D (rot)	MH	TEH	0.5	0.07	0.01	0.11
4	SL	MH	WB	1.2	0.10	0.02	0.08
5	SL-375 ^e	MH	TEH	1.1	0.08	0.03	0.09
6	SL-GR ^f	MH	TEH	1.4	0.02	0.04	0.22
7	SL-Adv. Burn ^g	MH	TEH	1.0	0.07	0.05	0.05
8	SL ^h	BW	TEH	0.2	0.05	0.06	0.02
9	SL	BW	WB	0.2	0.07	0.03	0.03
10	SL-Adv. Burn	BW	TEH	0.7	0.04	0.06	0.0
11	SL-GR	BW	TEH	1.4	0.01	0.01	0.26
12	SL	LP	TEH	0.5	0.05	0.06	0.01
13	SL	LP	WB	0.5	0.07	0.05	0.02
14	SL-Adv. Burn	LP	TEH	0.7	0.06	0.03	0.02
15	SL-No Burn	LP	TEH	0.2	0.1	0.07	0.03
16	SL-No Burn	LP	WB	0.02	0.08	0.05	0.03
17	SL-GR	LP	TEH	1.2	0.01	0.01	0.25
18	BCK	MH	TEH	0.8	0.04	0.04	0.0
19	BCK	MH	WB	0.5	0.03	0.03	0.0
20	BCK	BW	TEH	0.0	0.0	0.0	0.0
21	BCK	BW	WB	0.0	0.0	0.0	0.0
22	BCK	BW	TEH	0.0	0.0	0.0	0.0
23	BCK	BW	WB	0.0	0.0	0.0	0.0
24	SL	none	none	1.0	0.20	0.0	0.0

^aWe use both the Swesty-Lattimer (SL) and Baron-Cooperstein-Kahana (BCK) equations of state

^bThe following flux limiters are employed: Herant (MH), Bowers-Wilson (BW), Levermore-Pomraning (LP).

^cWe use the detailed electron/positron emission rates of Takahashi, El Eid & Hillebrandt (TEH-1977) and the simplified rates used by WB.

^dThe 2-D models are SPH simulations with ~ 2300 particles. The rotational simulation assumes a white dwarf spinning with a period of 2s.

^e $K_1 = 375$. In all other SL EOS simulations, $K_1 = 180$.

^fThis run includes General Relativistic effects.

^gSome runs include an additional burning network to be used prior to the onset of nuclear statistical equilibrium. In other runs, there we have turned off even the NSE network to test the range of effects from nuclear burning.

^hThe most probable outcomes are bold-faced.

Table 5.2. BCK EOS models^a

$BCK\gamma$	W_s	K_0^{sym}	xkz	Result
1.5	31.5	180	2.0	- ^b
1.5	31.5	375	2.0	-
2.5	31.5	180	2.0	-
2.5	31.5	375	2.0	-
3.5	31.5	180	2.0	-
3.5	31.5	375	2.0	-
1.5	25.0	180	2.0	-
1.5	25.0	375	2.0	-
3.5	25.0	180	2.0	-
3.5	25.0	375	2.0	-
1.5	38.0	180	2.0	-
1.5	38.0	375	2.0	-
3.5	38.0	180	2.0	-
3.5	38.0	375	2.0	-
1.5	25.0	180	1.5	-
1.5	25.0	375	1.5	-
3.5	25.0	180	1.5	-
3.5	25.0	375	1.5	-
1.5	38.0	180	1.5	-
1.5	38.0	375	1.5	-
3.5	38.0	180	1.5	-
3.5	38.0	375	1.5	-
1.5	25.0	180	2.5	0.05 M_\odot ejected
1.5	25.0	375	2.5	-
3.5	25.0	180	2.5	0.05 M_\odot ejected
3.5	25.0	375	2.5	-
1.5	38.0	180	2.5	-
1.5	38.0	375	2.5	-
3.5	38.0	180	2.5	-
3.5	38.0	375	2.5	-
2.5	25.0	180	2.0	-
2.5	25.0	375	2.0	-
3.5	25.0	180	2.0	-
3.5	25.0	375	2.0	-
2.5	25.0	180	2.5	0.05 M_\odot ejected
2.5	25.0	375	2.5	-
2.5	31.5	180	2.5	-
2.5	31.5	375	2.5	-

^aIn all these models we use the Levermore-Pomraning flux limiter and the full neutrino source terms.

^bExcept where specifically noted, the end result for these simulations was no explosion. Of course, this does not exclude mass ejection from neutrino winds.

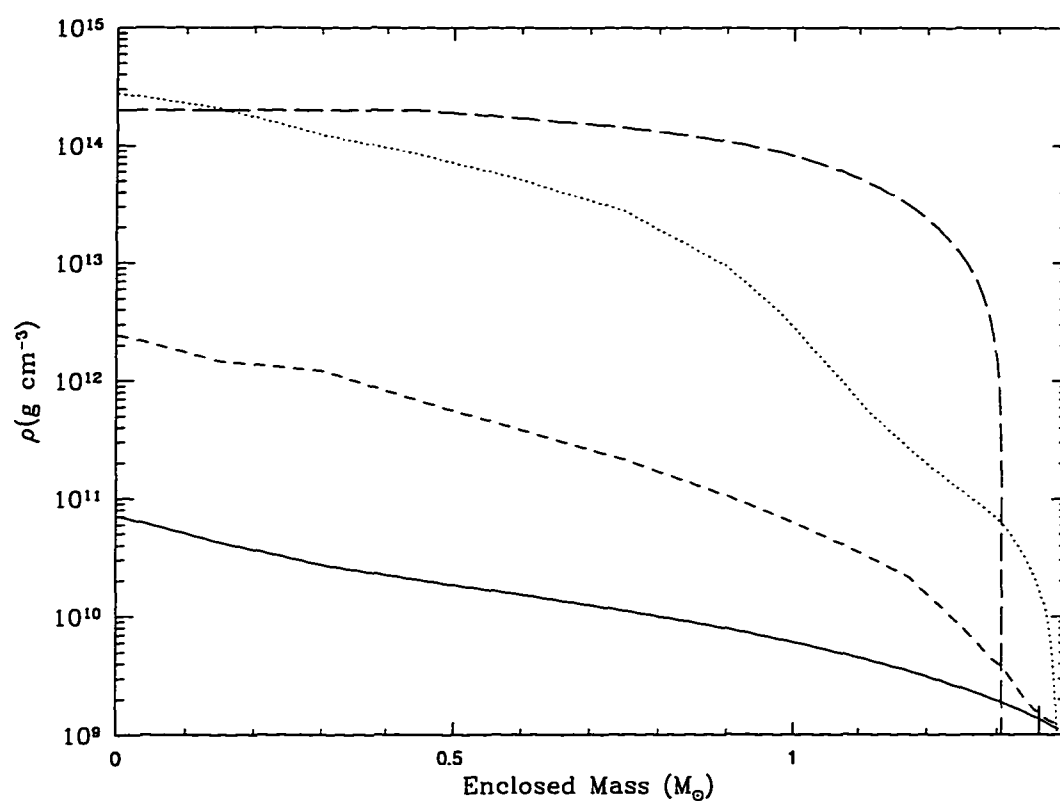


Figure 5.1 shows density profiles for the initial model (solid line), the BCK EOS after 40 ms (short-dashed line), the SL EOS after 40 ms (dotted line), and a simulation using 80 % of the pressure from the BCK EOS after 40 ms (long-dashed line). Changing the pressure by 20 % drastically alters the evolution of the collapse.

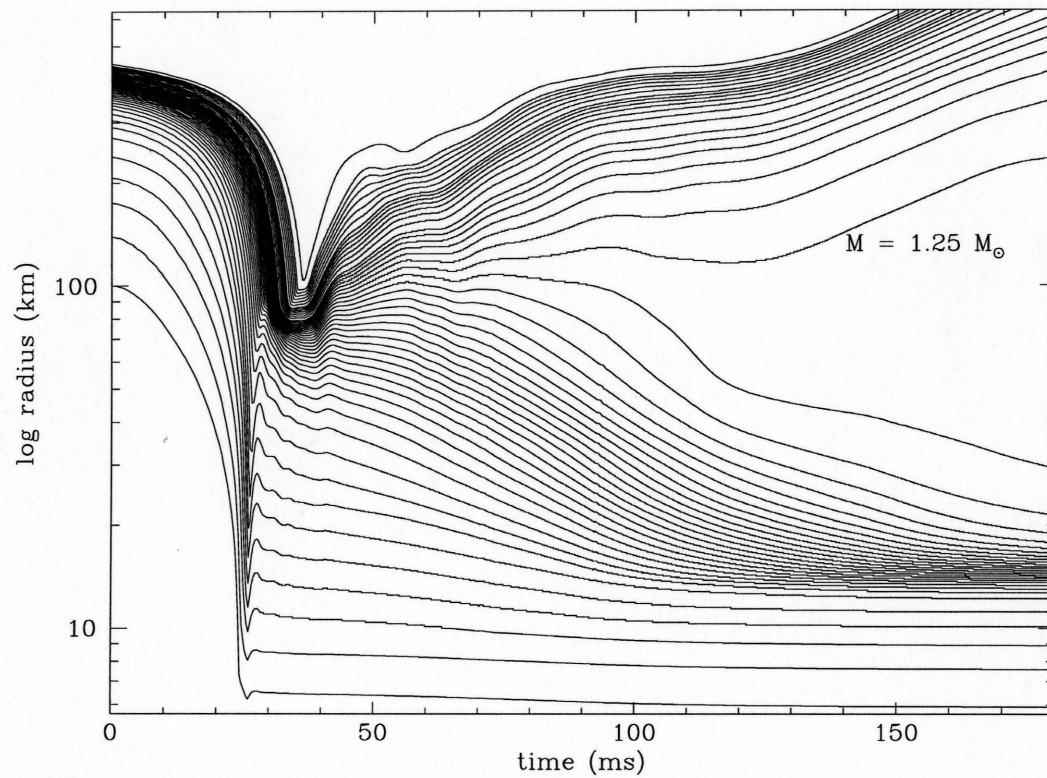


Figure 5.2 displays mass-point trajectories for a simulation using the SL EOS. The resolution is increased near the transition between ejected material and proto-neutron star material. The inner 9 lines represent the $1M_{\odot}$ core.

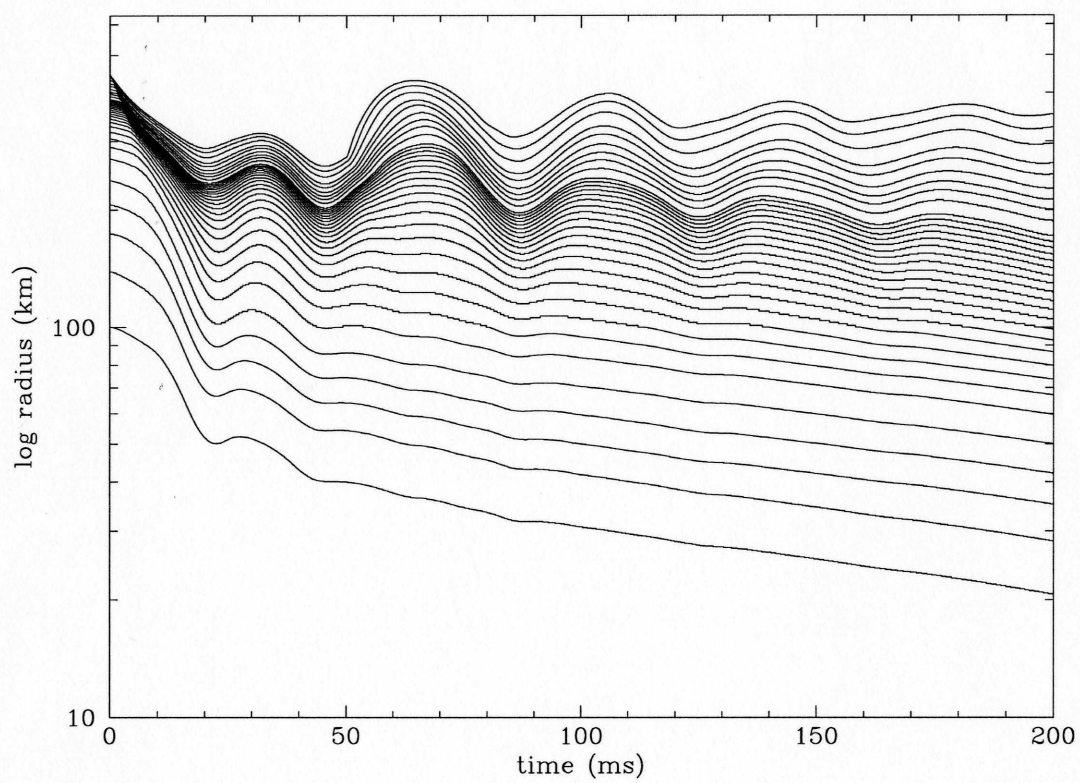


Figure 5.3 is identical to Figure 2 using the BCK equation of state.

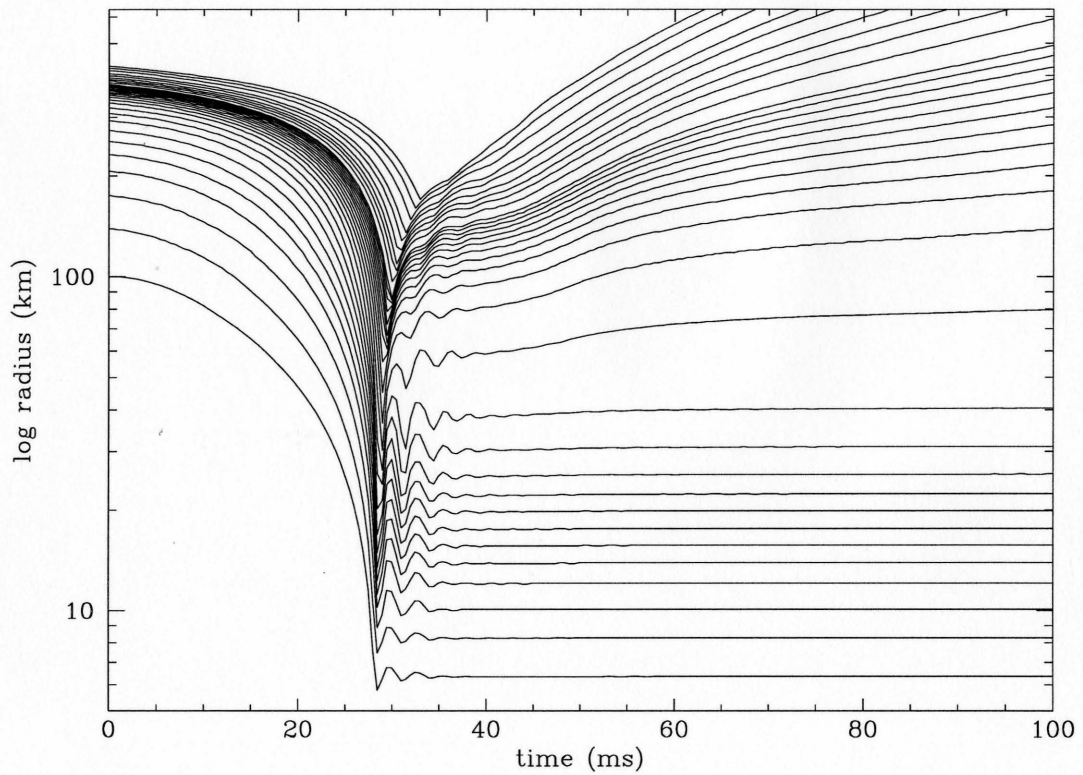


Figure 5.4 is identical to Figure 2 with the same SL EOS but without neutrino transport. Comparison with Figure 2 differentiates a prompt explosion from a delayed neutrino explosion.

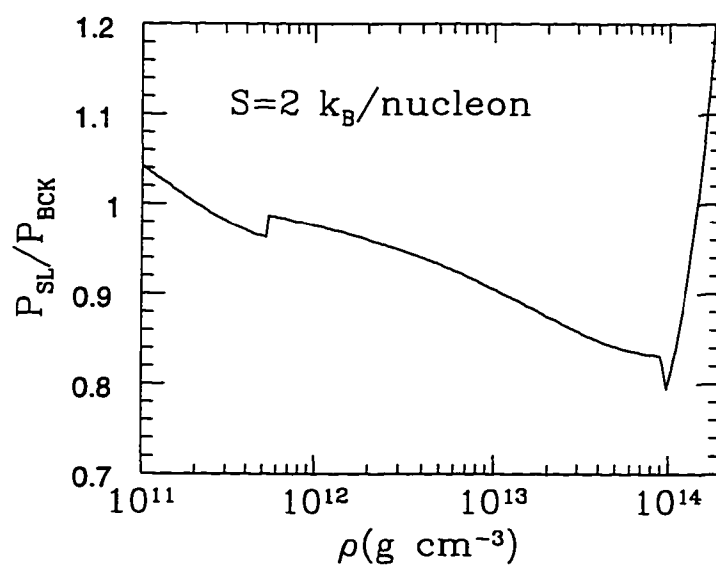


Figure 5.5 plots the ratio of pressure from the SL EOS and the BCK EOS. For densities less than 10^{14} g cm $^{-3}$, the BCK pressure is consistently higher by 10-20 %.

REFERENCES

- Abramovici, A., Althouse, W.E., Drever, R.W.P., Gursel, Y., Kawamura, S., Raab, F.J., Shoemaker, D., Sievers, L., Spero, R.E., Thorne, K.S., 1992, *Science*, 256, 325
- Allen, C.W., 1973, *Astrophysical Quantities* (London: Athlone)
- Anderson, S.B., Gorham, P.W., Kulkarni, S.R., Prince, T.A., & Wolszczan, A., 1990, *Nature*, 346, 42
- Bahcall, J.N., Glashow, S.L., 1987, *Nature*, 326, 476
- Bailyn, C.D. & Grindlay, J.E., 1990, *ApJ*, 353, 159
- Baron, E., Cooperstein, J., & Kahana, S., 1985, *Pys. Rev. Lett.*, 55, 126
- Baron, E., Cooperstein, J., Kahana, S., & Nomoto 1987, *ApJ*, 320, 304
- Benz, W. 1991, *An introduction to Computational Methods in Hydrodynamics, in Late Stages of Stellar Evolution and Computational Methods in Astrophysical Hydrodynamics*, ed. C.B. de Loore, (Berlin:Springer), p 259
- Benz, W., Fryer, C.L., Herant, M., Colgate, S.A., in preparation
- Benz, W., & Hills, J.G. 1992, *ApJ*, 389, 546
- Benz, W., Hills, J.G, & Thielemann, F.-K., 1989, *ApJ*, 342, 986
- Bergeron, P., Wesemael, F., & Beauchamp, A., 1995, *PASP*, 107, 1047
- Bethe, H.A. 1990, *Rev. of Mod. Phys.*, 62, 801
- Bhattacharya, D. & van den Heuvel, E.P.J., 1991, *Phys. Rev. Let.*, 203, 1
- Biehle, G.T. 1991, *ApJ*, 380, 167
- Biehle, G.T. 1994, *ApJ*, 420, 364
- Bisnovatyi-Kogan, G.S., & Lamzin, S.A. 1984, *Soviet Astron.*, 28, 187
- Blaauw, A., 1961, *Bull. Astron. Inst. Netherlands*, 15, 265
- Blinnikov, S.I., Dunina-Barkovskaya, N.V., & Nadyozhin, D.K., 1996, *ApJS*, 106, 171
- Bondi, H. 1952, *MNRAS*, 112, 195
- Bowers, R.L. & Wilson, J.R., 1982, *ApJS*, 50, 115

- Brandt, N. & Podsiadlowski, P., 1995, MNRAS, 274, 461
- Bradt, H.V.D., Ohashi, T., Pounds, K.A., 1992, ARA&A, 30, 391
- Brown, G.E., 1995, ApJ, 440, 270
- Burrows, A., Hayes, J., 1996, Phys. Rev. Let., 76, 352
- Burrows, A., & Woosley, S. 1986, ApJ, 308, 680
- Burstein, D., & Heiles, C., 1982, AJ, 87, 1165
- Canal, R., Isern, J., & Labay, J. 1990, ARA&A, 28, 183
- Cannon, R.C. 1993, MNRAS, 263, 817
- Cannon, R.C., Eggleton, P.P., Żytkow, A.N., & Podsiadlowski, P. 1992, ApJ, 386, 206
- Caraveo, P., 1993, ApJ, 415, L111
- Chen, K., & Leonard, P.J.T. 1993, ApJ, 411, L75
- Chen, K., & Ruderman, M. 1993, ApJ, 408, 179
- Chevalier, R.A. 1989, ApJ, 346, 847 (C89)
- Chevalier, R.A. 1993, ApJ, 411, L33
- Chanmugam, G., 1992, ARA&A, 30, 143
- Cisneros-Parra, J.N., 1970, A&A, 8, 141
- Colgate, S.A. 1971, ApJ, 163, 221
- Colgate, S.A., Herant, M., & Benz, W. 1993, Phys. Rep., 227, 157 (CHB)
- Colgate, S.A., & Leonard, P.J.T., 1993, BATSE Gamma Ray Burst Workshop
- Colgate, S.A., Petschek, A.G., & Kriese, J.T., 1980, ApJ, 237, L81
- Cordes, J.M., Romani, R.W., Lundgren, S.C., 1993, Nature, 362, 133
- Cox, A.N., Vauclair, S., & Zahn, J.P. 1983, Astrophysical Processes in Upper Main Sequence Stars, (CH-1290 Sauverny : Geneva Observatory)
- Crane, P., Nelson, J.E., Tyson, J.A., Nature, 280, 367
- Dalton, W.W. & Sarazin, C.L., 1995, ApJ, 448, 369

- Dar, A., Kozlovsky, B., Nussinov, S., & Ramaty, R. 1992, *ApJ*, 388, 164
- Davidson, A., Margon, B., Liebert, J., Spinrad, H., Middleditch, J., & Chanan, G., 1975, *ApJ*, 200, L19
- Davies, M.B. & Benz, W., 1995, *MNRAS*, 276, 876
- Davies, R.E., & Pringle, J. 1980, *MNRAS*, 191, 599
- Dewey, R.J. & Cordes, J., 1987, *ApJ*, 321, 780
- Drukier, G.A., 1996, *MNRAS*, 280, 498
- Eggleton, P.P., 1983, *ApJ*, 268, 368
- Eich, C., Zimmerman, M.E., Thorne, K.S., & Żytkow, A.N. 1989, *ApJ*, 346, 277
- Ergma, E. 1993, *A&A*, 273, L38
- Filippenko, A.V., Richmond, M.W., Branch, D., Gaskell, C.M., Herbst, W., Ford, C.H., Treffers, R.R., Matheson, T., Ho, L.C., & Dey, A., 1992 *AJ* 104 1543
- Flannery, B.P., & van den Heuvel, E.P.J., 1975, *A&A*, 39, 61
- Frail, D.A., Gross, W.M., & Whiteoak J.B.Z. 1994, *ApJ*,
- Fryer, C.L., Benz, W., Herant, M., 1996, *ApJ*, 460, 801
- Fryer, C.L., Benz, w., Herant, M., Colgate, S.A., in preparation
- Fryer, C.L., Burrows, A., & Benz, W., in preparation
- Fryxell, B.A., & Taam, R.E. 1988, *ApJ*, 335, 862
- Gamow, G. 1937, *Structure of Atomic Nuclei and Nuclear Transformations*, Oxford University Press
- Gies, D.R. & Bolton, C.T., 1986, *ApJS*, 61, 419
- Goodman, J. 1986, *ApJ*, 308, L47
- Goodman, J., Dar, A., & Nussinov, S. 1987, *ApJ*, 314, L51
- Gunn, J.E., & Ostriker, J.E., 1970, *ApJ*, 160, 979
- Habets, G.M.H.J., Ph.D. Thesis, University of Amsterdam
- Hansen, C.J., Kawaler, S.D., *Stellar Interiors-Physical Principles, Structure, and Evolution*, 1994, (New York: Springer-Verlag)

- Hartmann, D., Woosley, S.E., & El Eid, M.F. 1986, *ApJ*, 307, 414
- Herant, M., Benz, W., Hix, W. R., Fryer, C. L., & Colgate, S. A. 1994, *ApJ*, 435, 339 (HBHFC)
- Herant, M. & Benz, W. 1992, *ApJ*, 387, 294
- Herant, M., Benz, W., & Colgate, S.A. 1992, *ApJ*, 395, 642
- Hills, J.G., 1983, *ApJ*, 267, 322
- Hix, R., Thielemann, F.K., Fushiki, I., & Truran, J.W. 1994, in preparation for *ApJ*
- Houck, J.C., & Chevalier, R.A. 1991, *ApJ*, 376, 234 (HC)
- Hulse, R.A., Taylor, J.H., 1975, *ApJ*, 195, L51
- Iben, I., Jr. 1967 *ARA&A*, 5, 571
- Iben, I. Jr. & Tutukov, A.V., 1996, *ApJ*, 456, 738
- Iben, I. Jr., Tutukov, A.V., & Yungelson, L.R., 1995, *ApJS*, 100, 217
- Iben, I. Jr., Tutukov, A.V., & Yungelson, L.R., 1995, *ApJS*, 100, 233
- Johnston, S., Koribalski, B., Weisberg, J.M., Wilson, W., 1996, *MNRAS*, 279, 661
- Janka, H.T., 1991 PhD thesis
- Junker, W., & Schaefer, G., 1992, *MNRAS*, 254, 146
- Kalogera, V. 1996, *ApJ*, 471, 352
- Kalogera, V., & Webbink, R.F., 1996, submitted to *ApJ*
- Kalogera, V. & Webbink, R.F., 1996c submitted to *ApJ*
- Kaspi, V.M., Bailes, M., Manchester, R.N., Stappers, B.W., Bell, J.F., 1996, *Nature*, 381, 584
- King, A.R., & Lasota, J.-P., 1991, *ApJ*, 378, 674
- Kippenhahn, R., & Weigert, A., 1990, *Stellar Structure and Evolution*, (Berlin: Springer-Verlag)
- Kirshner, R.P., Morse, J.A., Winkler, P.F., & Blair, J.P., 1989, *ApJ*, 342, 260
- Kulkarni, S.R., Narayan, R., & Romani, R.W., 1990, *ApJ*, 356, 174

- Landau, L.D. 1937, Doklady Akad. Nauk USSR, 17, 301
- Lamb, D.Q., 1995, PASP, 107, 1152
- Lattimer, J. M., Swesty, F. D. 1991, Nuc. Phys. A, 535, 331
- Leonard, P.J.T., 1990, JRASC, 84, 216
- Leonard, P.J.T., 1995, MNRAS, 277, 1080
- Leonard, P.J.T. & Dewey, R.J., 1992, Conf. on Luminous High-Latitude Stars
- Leonard, P.J., Hills, J.G., & Dewey, R.J. 1994, ApJ, 423, L19
- Levermore, C.D., & Pomraning, G.C., 1981, ApJ, 248, 321
- Liebert, J., 1980, ARA&A, 18, 363
- Lyne, A.G., & Lorimer, D. R. 1994, Nature, 369, 127
- Masters, A.R., & Roberts, D.H., 1975, ApJ, 195, L107
- Mayle, R. & Wilson, J.R. 1988, ApJ, 334, 909
- Meurs, E.J.A. & van den Heuvel, E.P.J., 1989, A&A, 226, 88
- Mihalas, D., & Binney, J., 1968, Galactic Astronomy, Chapter 4, W.H. Freeman & Co.
- Miyamoto, M. & Nagai, R., 1975, PASJ, 27, 533
- Morse, J.A., Winkler, P.F., & Kirshner, R.P., 1995, AJ, 109, 2104
- Motch, C., Belloni, D., Buckley, D., Gottwald, M., Hasinger, G., Pakull, M.W., Pietsch, W., Reinsch, K., Remillard, R.A., Schmitt, J.H.M.M., Trumper, J., Zimmerman, H.U., 1991, A&A, 246
- Nadezhin, D.K. 1974, Nauchnye Informatsii Astron. Sov. Akad. Nauk SSR, 32, 33
- Narayan, R., & Ostriker, J.P., 1990, ApJ, 352, 222
- Nice, D.J., Sayer, R.W., & Taylor, J.H., ApJ, 466, L87
- Nice, D.J., 1996, private communication
- Nomoto, K., 1986, Ann. NY Acad. Sci. 470, 294
- Nomoto, K., Kondo, Y., 1991, ApJ, 367, L19

- Paczynski, B., 1970, *Acta. Astr.*, 21, 1
- Paczynski, B., 1986, 1986, *ApJ*, 308, L43
- Paczynski, B. 1990, *ApJ*, 363, 218
- Philp, C.J., Evans, C.R., Leonard, P.J.T., Frail, D.A., 1996, *AJ*, 111, 1220
- Podsiadlowski, P., Rees, M.J., Ruderman, M., 1995, *MNRAS*, 273, 755
- Prince, T.A., Anderson, S.B., Kulkarni, S.R., & Wolszczan, A., 1991, *ApJ*, 374, L41
- Rasio, F. A. 1996, in *Evolutionary Processes in Binary Stars*, ed. R. A. M. J. Wijers, M. B. Davies, & C. A. Tout (Dordrecht: Kluwer Academic Publishers), 121
- Rasio, F.A., & Livio, M., 1996, *ApJ*, 471, 366
- Ray, A., & Kluzniak, W. 1990, *Nature*, 344, 415
- Ruderman, M. 1991, *ApJ*, 366, 261
- Roberts, D.H., Masters, A.R., & Arnett, D., 1975, *ApJ*, 195, L107
- Ruffert, M. 1994a, *ApJ*, 427, 342
- Ruffert, M. 1994b, *A&AS*, 106, 505
- Ruffert, M. 1995, submitted to *ApJ*
- Ruffert, M., & Anzer, U. 1995, *A&A*, 295, 108
- Ruffert, M., & Arnett, W.D. 1994, *ApJ*, 427, 351
- Ruffert, M., Janka, H.-Th., Shafer, G., 1996, *ApJ*, 311, 532
- Sawada, K., Matsuda, T., Anzer, U., Börner, & Livio, M. 1989, *ApJ*, 221, 263
- Sayer, R.W., Nice, D.J., & Kaspi, V.M., 1996, *ApJ*, 461, 357
- Scalo, J. M. 1986, *Fund. of Cosmic Phys.*, 11, 1
- Schaller, G., Schaerer, D., Meynet, G., Maeder, A., 1992, *A&AS*, 98, 523
- Schinder, P.J. 1990, *ApJ*, 374, 249
- Schwarzschild, M., 1958, *Structure and Evolution of the Stars*, (Princeton: Princeton Univ. Press)

- Smarr, L. L., & Blandford, R. 1976, *ApJ*, 207, 574
- Shames, I. H., 1992, *Mechanics of Fluids*, (New York: McGraw-Hill)
- Shapiro, S.L., & Teukolsky, S.A., 1983, *Black Holes, White Dwarfs, and Neutron Stars*, Wiley & Sons, Inc., p. 169
- Srinivasan, G., & van den Heuvel, E.P.J., 1982, *A&A*, 108, 143
- Stokes, G.H., Taylor, J.H., & Dewey, R.J., 1985, *ApJ*, 294, L21
- Shapiro, S.L., & Teukolsky, S.A., 1983, *Black Holes, White Dwarfs, and Neutron Stars*, (New York: Wiley), 405
- Swesty, F.D., Lattimer, J.M., & Myra, E.S., 1994, *ApJ*, 425, 195
- Taam, R.E., Bodenheimer, P., & Ostriker, J.P. 1978, *ApJ*, 222, 269
- Taam, R.E., & Fryxell, B.A., 1989, *ApJ*, 339, 297
- Takahashi, K., El Eid, M.F., & Hillebrandt, W. 1977, *A&A*, 67, 185
- Tammann, G.A., Loeffler, W., Schroeder, A., 1994, *ApJS*, 92, 487
- Taylor, J.H. & Cordes, J.M., 1993, *ApJ*, 411 674
- Taylor, J.H., Manchester, R.N., & Lyne, A.G., 1993, *ApJS*, 88, 529
- Taylor, J.H., & Weisberg, J.M., 1982, *ApJ*, 253, 908
- Taylor, J.H., & Weisberg, J.M., 1989, *ApJ*, 345, 434
- Terman, J.L., Taam, R.E., 1995, *MNRAS*, 276, 1320
- Terman, J.L., Taam, R.E., & Hernquist, L., 1994, *ApJ*, 422, 729
- Theuns, T., & Jorissen, A. 1993, *MNRAS*, 265, 946
- Timmes, F.X., Woosley, S.E., Weaver, T.A., 1996, *ApJ*, 457, 834
- Thorne, K. S. 1996, in *Compact Stars in Binaries*, ed. J. van Paradijs, E. P. J. van den Heuvel, & E. Kuulkers (Dordrecht: Kluwer Academic Publishers), 153
- Thorne, K.S., & Żytkow, A.N. 1975, *ApJ*, 199, L19
- Thorne, K.S., & Żytkow, A.N. 1977, *ApJ*, 212, 832
- Trincheri, G., Fabbiano, G., 1991, *ApJ*, 382, 82

- Tutukov, A.V., Chugai, N.N., & Yungelson, L.R., 1984, *Pisma v Ast. Zh.*, 10, 586
- van Kerkwijk, M.H., van Paradijs, J., Zuiderwijk, E.J., 1995, *A&A*, 303, 497
- van den Heuvel, E.P.J. 1984, *A&A*, 5, 209
- van den Heuvel, E.P.J., 1994, *A&A*, 291, L39
- van den Heuvel, E.P.J., 1995, *JApA*, 16, 255
- van den Heuvel, E.P.J., & Rappaport, S., 1986, *Physics of Be stars*, Proc. of the 92nd IAU Coll., 291, Cambridge University Press
- van Kerkwijk, M.H., 1996, private communication
- Van Riper, K.A. 1979, *ApJ*, 232, 558
- Wasserman, I., Cordes, J., & Chernoff, D., in preparation
- Webbink, R.F., 1975, *A&A*, 41, 1
- Wijers, R.A.M.J., van Paradijs, J., & van den Heuvel, E.P.J., 1992, *A&A*, 261, 145
- Wolszczan, A., 1991, *Nature*, 350, 688
- Woosley, S. E. 1996, private communication
- Woosley, S.E. & Baron, E., 1992, *ApJ*, 391, 228
- Woosley, S.E., Langer, N., Weaver, T.A., 1993, *ApJ*, 411, 823
- Woosley, S.E., Langer, N., & Weaver, T.A., 1995, *ApJ*, 448, 315
- Woosley, S.E., & Weaver, T.A. 1983, *AIP Conf. Proc.*, 115, 273
- Woosley, S.E., & Weaver, T.A. 1995, *ApJ Sup.*, in press
- Yamaoka, H., Shigeyama, T., Nomoto, K., 1993, *ApJ*, 267, 433
- Zel'dovich, Ya.B., Ivanova, L.N., & Nadezhin, D.K. 1972, *Soviet Astr.-AJ*, 16, 209